UNIVERSITÉ DU QUÉBEC

MÉMOIRE PRÉSENTÉ À
L'UNIVERSITÉ DU QUÉBEC À CHICOUTIMI
COMME EXIGENCE PARTIELLE
DE LA MAÎTRISE EN INGÉNIERIE

par

Pankaj Jain

ÉTUDE DU TRANSFERT DE CHALEUR CONVECTIF DANS UN FOUR CIRCULAIRE

Avril 1996

Bibliothèque
Paul-Émile-Boulet

UQAC
Université du Québec
à Chicoutimi

Mise en garde/Advice

Afin de rendre accessible au plus grand nombre le résultat des travaux de recherche menés par ses étudiants gradués et dans l'esprit des règles qui régissent le dépôt et la diffusion des mémoires et thèses produits dans cette Institution, **l'Université du Québec à Chicoutimi (UQAC)** est fière de rendre accessible une version complète et gratuite de cette œuvre.

Motivated by a desire to make the results of its graduate students' research accessible to all, and in accordance with the rules governing the acceptation and diffusion of dissertations and theses in this Institution, the **Université du Québec à Chicoutimi (UQAC)** is proud to make a complete version of this work available at no cost to the reader.

L'auteur conserve néanmoins la propriété du droit d'auteur qui protège ce mémoire ou cette thèse. Ni le mémoire ou la thèse ni des extraits substantiels de ceux-ci ne peuvent être imprimés ou autrement reproduits sans son autorisation.

The author retains ownership of the copyright of this dissertation or thesis. Neither the dissertation or thesis, nor substantial extracts from it, may be printed or otherwise reproduced without the author's permission.

To
My dear parents

My brother, Mukesh
and his family

ABSTRACT

This thesis deals with the development and testing of a heated skin technique to determine the magnitude and distribution of the heat transfer coefficients along the flat molten metal bath in circular remelting furnaces. Various flow visualization techniques were equally applied to explore the flow structure inside the entire furnace chamber.

The heated skin technique employs an electrically heated composite layer to simulate the flat molten metal bath condition in the scaled model. The direction of heat flow is reverse to that in the reality, i.e. in the model the gas is colder than the surface. The heat transfer coefficients are measured by thin foil thermocouples and heat flux sensors, while the distribution of the surface temperature and formation of hot spots are monitored by infrared thermography.

Five sets of experimental runs were performed for various rotational and axial burner orientations with the Reynolds numbers ranging from 6×10^3 to 3×10^4. The results were verified qualitatively with the velocity distribution and infrared imaging. The repeatability of the experimental results was $\pm$ 3%.

SOMMAIRE

Dans cette étude, nous avons développé et testé la technique appelée "méthode de la peau chauffante" afin de mesurer les coefficients convectifs locaux sur la surface horizontale d'un four circulaire. L'écoulement des gaz dans la chambre de combustion a été exploré par différentes techniques de visualisation.

Pour la technique de la peau chauffante, on a utilisé une surface multicouche pour simuler les conditions du bain de métal fondu en modèle réduit. Le sens de la propagation de la chaleur est opposé à ce qu'il est en réalité parce que dans le modèle, le gaz est plus froid que la surface. Les coefficients de transfert de chaleur sont mesurés par des senseurs thermiques qui ont été placés sur la surface du modèle. Une caméra infrarouge est également utilisée pour visualiser la distribution de température et la formation des points chauds.

Cinq séries d'essais expérimentaux ont été effectués pour différentes orientations axiales et rotationnelles des brûleurs, et pour des nombres de Reynolds variant entre 6 $\times$ 10^3 et 3 $\times$ 10^4. Les résultats ont été comparés qualitativement avec ceux obtenus par la vélocimétrie et l'imagerie infrarouge. L'erreur expérimentale calculée à partir de la répétitivité des résultats est de l'ordre de $\pm$ 3%.

ACKNOWLEDGEMENTS

I am grateful and wish to thank my director, Professor L. I. Kiss, co-director, Professor A. Charette and Professor R. T. Bui, for their guidance and assistance throughout the course of this research.

I would like to express my appreciation to my colleagues, Foudil Dahmane, Babacar Fall, and all the other members of the GRIPS, for their advice and help in various phases of this investigation. I especially thank André Arsenault for his help in computer related problems while writing the thesis. I also thank P. Paquette for his great help in building the experimental equipment required by this work.

I am grateful to Alcan for providing financial support for this project. I would specially like to thank Mr. Thierry Bourgeois and Wesley Stevens of Alcan ARDC and Mr. Ed Rauch of Alcan Rolled Products for their enthusiastic interest and their diligence in providing all the industrial informations needed for the completion of this project.

Finally, I would like to thank my brother, Mukesh, and his family for the support they have given me during this masters.

TABLE OF CONTENTS

LIST OF FIGURES

LIST OF TABLES

NOMENCLATURE

SYMBOL	DESCRIPTION
A	surface area, m^2
c_1	first radiation constant, 3.742×10^{-12} W.cm^2
c_2	second radiation constant, 1.4388 cm.K
D	internal diameter of the furnace, m
E	emissive power, W/cm.μm
g	gravitational acceleration, m/s^2
h	heat transfer coefficient, $W/m^2.K$
H	height, m
He	helium gas
HFS	heat flux sensor
i	electric current, A
$\dot{I}$	momentum flow rate, $kg.m/s^2$
k	thermal conductivity, W/m.K
L	charateristic length, m
l	length parameter, m
$\dot{m}$	mass flow rate, kg/s
n	number of burners
P	perimeter, m
q	heat flow rate, W
$\dot{q}$	heat flux, W/m^2
R	thermal resistance, $K/W/m^2$
R	radius, m
T	temperature, K

SYMBOL	DESCRIPTION
TC	thermocouple
V	charateristic velocity, m/s
$\dot{V}$	volumetric flow rate, m^3/s
W	power, W
x	volume fraction

DIMENSIONLESS NUMBERS

Ar	Archimedes number
Gr	Grashof number
Nu	Nusselt number
Re	Reynolds number
Ri	Richardson number
St	Strouhal number

GREEK SYMBOLS

α	temperature coefficient of resistance, K^{-1}
β	thermal volumetric expension coefficient, K^{-1}
ϵ	emissivity
λ	wavelength, μm
μ	dynamic viscosity, kg/m.s
ν	kinematic viscosity, m^2/s
σ	Stefan-Boltzmann constant, 5.67×10^{-8} $W/m^2.K^4$
ρ	density, kg/m^3
τ	time, s

SUBSCRIPTS	DESCRIPTION
avg	average
conv	convection
f	film
m	model
mix	mixture
rad	radiation
s	sensor
surf	surface

Chapter 1

INTRODUCTION

1.1 AIMS AND MOTIVATION

Forced convection is an important mechanism of heat transfer in melting and solidification of metals. Over the last few years it has received concentrated research attention due to the large number of applications in material processing, metallurgy, purification of metals, solidification of castings and ingots, and various other thermal engineering problems. One problem of interest to the metallurgical industry is the melting of scrap metal. Scrap metal refers either to metal chopped from the ends of ingots or to compressed blocks of used beverage containers or other recycled materials. This thesis is concerned with experimental measurements of convective heat transfer coefficients in a circular remelting furnace having a highly three dimensional complex flow. This investigation was carried out on a 1:8.83 model of a remelting circular furnace. The model was based on the rules of geometrical similarity between the model and the original furnace. The implementation of the "heated skin technique" developed as a heat transfer measuring tool is discussed in detail.

Research involves a combination of experimental and analytical work. The theoretician strives to explain or predict the results of experiments on the basis of analytical models which are in accordance with fundamental physical principles that have been well estab-

lished over the years. When experimental data are encountered which do not fit into the scheme of existing physical theories, a skeptical eye is cast first at the experimental data and then at appropriate theories. In some cases the theories are modified or revised to take into account the results of new experimental data, after being sure that the validity of the data has been ascertained. In any event, all physical theories must eventually rely upon experiment for verification. It is worthwhile to mention here that analytical or numerical solutions are not always possible to obtain, and indeed, in many instances they are very cumbersome and difficult to use. Whether the research is of a basic or developmental character, the dominant role of experimentation is still present. Physical experimentation is the ultimate test of most theories.

Despite the increasing interest in recycling scrap metals, it appears that there is no experimental study reported in the open literature to our knowledge for the case of the furnace geometry studied in this research work. The measurement of local heat transfer distribution for complex geometries like ours with their correspondingly complex flows is needed to design the furnace chamber, the chimney and to determine number of burners and their relative position and orientation. Good design not only helps optimizing the process, but also reduces the chances of oxidation of metal due to local overheating (formation of hot spots) [7,10,49]. Measurement of the local heat transfer coefficients provide both needed design data and a check on computational models for the prediction of heat transfer for such complex flows. The flow visualization experiments were equally made to explore the flow structure as well as to improve the understanding of mechanisms inside the entire furnace chamber [23,25,24].

The technique employs commercially available (custom design) foil heaters. The

foil heaters, divided into 17 independent electrically heated sections ("heated skin"), are attached to the test section to be studied. When a constant current passes through the heater, a nearly constant heat flux is generated. By measuring heat fluxes and temperatures at different locations on the foil heaters (test section) with the help of attached micro-foil heat flux sensors and foil thermocouples, local heat transfer coefficients can be calculated. The overall goal of this thesis is to develop this heated skin technique for local measurements in natural, forced and mixed convection problems, and to establish its capabilities and limitations by applying it to test problems. In our experiments, the direction of heat flow is inverted, i.e., instead of gas to surface heat transfer, the test surface is kept at higher temperature than that of the cooling air stream and the surface to gas heat exchange is measured [19,26,27].

The foil heater possesses a number of properties which make it particularly suitable for heat transfer studies. Firstly, the heaters are manufactured by foil-etching, which furnishes a reasonably uniform thickness of electrical resistance and this resistance is only slightly temperature dependent. Secondly, heat conduction along the foil heater itself may be neglected because the resistance coating is only a few Angströms thick. Thirdly, the flexible nature of foil heaters allows them to be attached to almost any two-dimensional surface. In addition, surfaces which are moderately three-dimensional in nature can also be handled by using a number of heaters.

The two thermal boundary conditions encountered in convection heat transfer are the uniform wall heat flux and the uniform wall temperature conditions. These two thermal boundary conditions are illustrated in Figure 1.1.

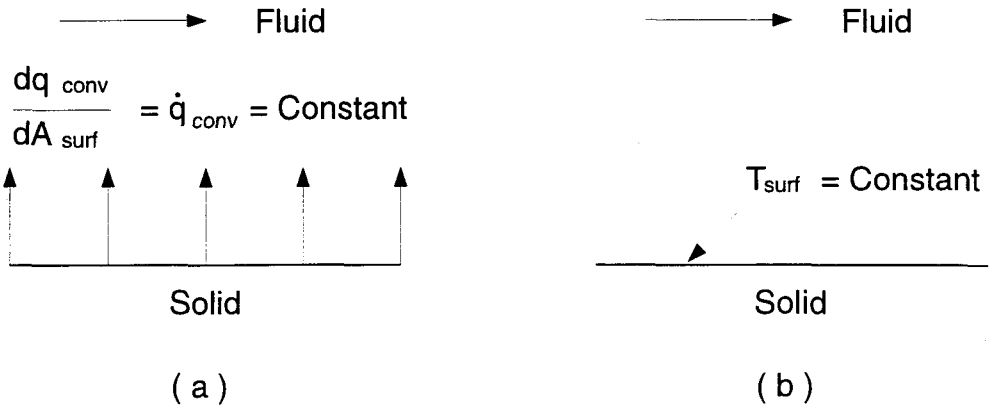

Figure 1.1 Two basic types of convection boundary conditions. (a) Uniform wall heat flux. (b) Uniform wall temperature.

A uniform wall heat flux condition can be experimentally achieved by the generation of energy in the wall itself by the flow of electric current as mentioned earlier. A uniform wall temperature boundary condition can as well be achieved by dividing the heated skin into many individually controlled electrical current flow sections [46].

In the present study, the convective parameter is varied by changing the externally induced overall flow velocity, heat flux, and/or orientation of burners. It was found that about three to four hours are needed for the surface temperature/flux distribution to reach the appropriate new steady state if one or more of the input parameters, such as the heat flux, flow velocity, or burner orientation, is changed. This slow transient response is largely due to the conjugate nature of the transport process i.e., balancing of the downward conductive heat losses and the upward convection/radiation heat transfer is a time consuming process, and severely limits the speed with which different input conditions may be investigated.

The main objectives of this thesis can be summarized as follows:

1. Develop a method called "heated skin technique" to enable the acquisition of local heat transfer data in natural, forced, or mixed convection problems.

2. Evaluate the performance of the proposed technique by using it to determine local heat transfer coefficients on a model surface of a circular scrap melter in a turbulent flow field.
3. Verify the results against those of visualization experiments and measured velocity distribution in the furnace chamber.

The primary advantages of employing the heated skin technique for taking heat transfer measurements are:

1. The technique can be implemented relatively easily.
2. The accuracy of the method is comparable or better than many other available techniques, and
3. The equipment and instrumentation required to use the technique are available commercially, and are relatively inexpensive to purchase.

The ability to measure the temperature and heat flux at a surface is very important in many applications. In particular, it is often necessary to obtain such information in situations that are very sensitive to the evasive (perturbing) tendencies of probes. Generally there is a belief that traditional methods of directly measuring the rate of convective heat transfer from a surface, by placing instruments in the boundary layer, significantly alter the quantity under investigation by affecting both local temperature and velocities. However the use of very thin micro-foil heat flux sensors (0.46 mm thick) and foil thermocouples (0.005 mm thick) in this study, allow the measurement of the local convective heat transfer coefficients with negligible disturbance to the boundary layer.

1.2 BACKGROUND AND PREVIOUS WORK

Numerous experimental techniques for determining local heat transfer coefficients have been presented in the published literature. A comprehensive survey of all of these investigations will not be attempted here. Much of the theory relevant to measurement techniques in heat transfer has been reviewed in a book edited by J. P. Holman [18] and also in the one edited by Eckert and Goldstein [11]. In particular, the chapters on "Guarded Hot Plate Methods", by K. D. Maglić [33]; "Analogies to Heat Transfer Processes", by E. R. G. Eckert [11]; "Heat Transfer in Turbulent Flow and Experimental Results", by W. M. Rohsenow [43], are directly applicable to this study. The literature reviewed in this section is limited to those methods which can be used for taking local convection heat transfer measurements and to works which are relevant to the technique developed in this thesis.

Most of the techniques used to measure local heat transfer coefficients are based on three general methodologies in which:

1. The test surface is maintained at a constant temperature, and local heat fluxes are measured.
2. The analogy between heat and mass transfer is used to infer local heat transfer results by examining an equivalent mass transfer problem.
3. The test surface is maintained at a non uniform temperature, often by attaching an ohmic heater to the surface, and local heat fluxes are calculated.

In techniques which maintain the test surface at a constant temperature, it is necessary to determine local surface heat fluxes [29]. This objective has been accomplished by using heat flux gauges [12]; by employing a series of individually power controlled heating strips, which are adjusted to obtain a nearly constant surface temperature; and by measuring the

temperature gradient in the fluid next to the wall using optical methods [16,40,42]. This technique furnishes good results only if the heating surface area is divided into several small heating strips.

Heat flux gauges may be classified into two types: (i) the thermal resistance type; and (ii) the calorimetric type. Thompson [12] has presented an excellent review of the theory of operation of various types of heat flux gauges.

The basic principle of the thermal resistance type of heat flux gauges is to create one-dimensional heat conduction situation inside the gauge which is driven by the local heat flux at the test surface.

In the calorimetric type of heat flux gauge, the local heat flux is obtained from an energy balance applied to the gauge. Heat is either supplied or removed from the surface of the heat flux gauge in order to maintain isothermality of the test surface.

For the condition of constant temperature along surfaces, a method for measuring the local heat transfer coefficients along a flat plate has been proposed by T. Kumada [30]. The method uses the change of a wet surface temperature by radiation heating, and is based on the heat balance equation, which expresses a simple relationship between humidity and wet bulb temperatures. This method can be applied to isothermal conditions with large variations of the local heat transfer coefficients along the surface of a body.

Optical techniques have been used to obtain the temperature distribution and local heat transfer coefficients at a surface [2]. The most developed of the optical techniques are those that use the known dependence of the index of refraction of the working fluid on temperature. Hauf and Grigull [16] have presented a comprehensive review of three of these techniques, namely the shadowgraph, schlieren, and interference methods. The

interference method is generally used in natural convection experiments, but it is equally applicable in forced convection problems and can be extended to other applications such as certain fluid flow analyses. The major advantage of using interferometry is that there is no device or probe inside the fluid to disturb the flow and temperature fields.

The similarities between the physical mechanisms and the governing equations for heat and mass transfer in a constant property fluid suggests that the heat transfer results may be inferred from a study of an analogous mass transfer experiment. This is the basis of using the napthalene sublimation and electrochemical techniques to obtain natural or forced convection mass transfer data for studying the corresponding heat transfer problem. The two techniques will now be briefly discussed.

The napthalene sublimation technique involves the application of a uniform coating of napthalene to the surface being investigated. The boundary condition of constant mass concentration of napthalene vapor at the test surface in the mass transfer problem corresponds to a constant temperature boundary condition for the analogous heat transfer experiments. When the experiment is performed, napthalene sublimates at different rates from point to point on the test surface. By measuring the napthalene profile on the test surface before and after the experiment has been performed, local mass transfer coefficients may be determined. This technique has been used to study forced convection in a one-row plate fin and tube heat exchanger [44].

Another technique used to take local mass transfer measurements from a surface in a liquid environment is based on electrochemical reactions. In this method, the test surface is made a cathode for an electrochemical reaction. When a voltage difference is applied between the test surface and the tank containing the electrolytic solution, ions will plate out

on the cathode. These ion concentration gradients induce the density differences which drive the natural convection motion. An excellent review article discussing the theory relevant to the electrochemical method as well as its applications to both free and forced convection mass transfer measurements has been presented by T. Mizushina [36].

The third methodology that has been employed to measure local heat transfer coefficients involves maintaining the test surface at a non uniform temperature, and then estimating the local heat fluxes at the solid-fluid interface.

Ohmic heating is frequently used to provide a nearly constant heat flux boundary condition at a test surface. Early heat transfer measurements using ohmic heating were obtained by passing current through a thick metal wall. Giedt [15] was one of the first to attach a thin metal foil to a test surface made of low thermal conductivity material. In his experiments a 0.05 mm thick nichrome ribbon was helically bound around a lucite cylinder. Measurements of local heat transfer were made around the cylinder, which was oriented in a normal direction to the air stream. Heat conduction along the nichrome ribbon and radiation from the surface of the heater were calculated. Later Ota and Kon [38] and many others [45] used this method to generate constant heat flux boundary condition along surfaces.

A gold coated plastic sheet has been used as a heater in a number of recent investigations [5,17,37] to provide a nearly constant heat flux boundary condition at a test surface. S. A. Hippensteele et al. [17] were among the first to publish local convection heat transfer results using commercially available elements of a composite consisting of a plastic sheet coated with liquid crystal and another sheet with a thin layer of conducting material (gold or carbon). Qualitative photographs of impingement cooling of a single jet on a flat plate,

heat transfer at the end wall of a cascade, and film injection from a cylinder in cross flow were taken. Liquid crystals were used in this technique to obtain thermal patterns. These crystals can be categorized into three types: smectic, nematic, and cholesteric based on their molecular structure [1,4,8].

In this thesis, an attempt has been made to use the heated skin technique, which was applied primarily to determine the values and distribution of the local heat transfer coefficients along the horizontal surface of the molten metal bath in circular remelting furnaces. This technique will be described in detail in the chapters to follow.

1.3 SURVEY OF THE THESIS

There are a total of six chapters in this thesis. In chapter 1, the aims of this work and a synopsis of relevant investigations have already been presented. The organization of the remaining five chapters will now be summarized.

In chapter 2, the flow visualization experiments using various techniques are presented. The design and development of the heated skin technique for measuring local heat transfer coefficients is discussed in chapter 3. In the following chapter, a method of calibrating heat flux sensors and some pre-measurement preparations and experiments will be presented. In chapter 5, experiments, followed by results and discussions are presented. Finally, in chapter 6, the impact of this work is summarized, improvements are suggested and a number of extensions are recommended.

Chapter 2

FLOW VISUALIZATION

2.1 OBJECTIVE

The interest behind doing the flow visualization experiments was to make the process of transport phenomena visible in the entire furnace chamber and later use the results to design and develop the "heated skin" technique to determine the local heat transfer distribution along the horizontal surface of the flat molten metal bath in the circular remelting furnace. The flow visualization experiments were performed in two furnace configurations: one with 4 burners and one with 6 burners.

Flow visualization is superior to flow measurement in that the global physical phenomena in the entire flow field are retrieved. The information obtained from the flow visualization experiments is qualitative: exploring the structure, main flow regions and improving our understanding of these mechanisms. Besides a better comprehension of the flow structure, certain semi-quantitative conclusions (order of magnitude estimation, comparison, ranking) can be made on the basis of the results.

Like any model, a cold flow model cannot imitate the real situation perfectly, it cannot represent the complexity of physical phenomena such as chemical reactions, variations in material properties, buoyancy etc. In the preparatory phase of the project, a similarity study

was performed in order to determine the limitations and the scaling laws for the model.

2.2 MODELLING OF FLOW IN FURNACES

Numerical and physical modelling complement each other in aerothermodynamics. The study of a real, multicomponent, chemically reacting, turbulent, spontaneously fluctuating high temperature flow in its totality would require a highly complex numerical or physical model, the application of which would also be very expensive. On the other hand, a complex model can be inconvenient to use, as the separation and isolation of the various physical effects are not always feasible.

These considerations led us to the division of the whole project into smaller, easily tractable sub-projects: pure fluid dynamic study, ***determination of the convective heat transfer coefficients***, analysis of the radiation in and around the scrap and molten metal and modelling the melting process itself.

Analyzing the dominant influencing factors, most researchers agree that in the case of high momentum forced flows, the flow pattern in a real combustion chamber can be studied very well on a scaled cold flow model. In many cases, cold flow experiments of combustion chambers use water as the modelling fluid. Obviously neither water nor gas cold flow models are able to reproduce thermal buoyancy effects. In physical modelling, the effect of compressibility and thermal expansion can be analyzed separately, but introducing these effects requires additional complications. For example, the injection of a lighter component into the working fluid can approximately simulate thermal buoyancy. In our experiments air is used as the modelling fluid [23].

The flow inside the furnace is primarily driven by the high-momentum gas jets from the burners located along the perimeter. A secondary momentum source is represented by

the buoyancy forces, but while the first effect is mostly responsible for the movements in the horizontal plane, the buoyancy contributes basically to the flow pattern by generating vertical momentum components.

The most important basic output of the fluid dynamic modelling is a picture of the flow pattern. The qualitative informations like the shape of streamlines, path of particles, location and size of vortices, low velocity zones ("dead zones"), turbulent regions, boundary layer structure, zones of separation etc. have a primary importance for understanding the flow phenomena in a combustion chamber or a furnace. Flow visualization is an old, but continuously developing field of experimental fluid dynamics [50] and the new achievements in laser and image processing technology together with the new high-speed recording methods expand the capabilities significantly.

Quantitative analysis of the flow field in the physical models basically consists of the determination of the velocity field, velocity profiles and the measurement of turbulence intensities and analysis of the turbulence spectrum.

2.3 SIMILARITY STUDY, SCALING LAWS

Besides geometric similarity there are criteria for all physical effects, usually in the form of dimensionless groups. As it has been mentioned earlier, we cannot reproduce all the physical processes taking place in the real furnace. Therefore we will concentrate only on the dominant and most relevant ones. It often happens that a match between all the relevant dimensionless numbers cannot be realized simultaneously, but the conditions can be "tuned" in such a way that the influence of the various physical factors can be studied separately in subsequent experiments [23].

2.3.1 Geometric Similarity

As the geometric similarity between the model and the real furnace is a basic requirement, a strict scaling-down procedure should be followed. The only factor left free for modelling is the geometric ratio. This value is subject to the type and availability of construction materials, manufacturing capabilities and finally but not less importantly, the requirements of the experimental methods. Obviously the number of burners, their circumferential locations, the height and shape of the door and the stack should also be conformed.

In our case, the maximal size of the available plexiglass panes, the reasonable space requirements, and the accessibility for photo and video cameras represented the main constraints. The scaling factor was finally selected as 1 : 8.8333. This is not a round value, but results in clear and round numbers (in inches) for the construction of the model, and gives a very close match to the kinematic viscosity ratio, which plays a decisive role in the modelling of the dynamic effects.

2.3.2 Dynamic Similarity

The most important factors affecting the formation of the flow pattern inside the furnace are the momentum transport coefficients (molecular and turbulent viscosities and the corresponding viscous forces), the intensity of the convective momentum transport (generally referred to as the effect of the "inertia forces") and the source of momentum due to the temperature differences in the gas (buoyancy forces). Many dimensionless numbers have been created from the parameters and properties describing these effects, but only a few of them are independent.

In forced flow, the most important dimensionless group to be considered is the Reynolds number (*Re*), which relates the intensity of the momentum transfer by convection to that by molecular mechanisms (viscosity). The value of the Reynolds number strongly depends on how one selects the value of the characteristic velocity V and the characteristic length L. The complexity involved in determining these characteristic parameters will be discussed in detail in the later chapter 5.

2.3.3 Ratio of the Velocities in the Model and in the Real Furnace

From the identity requirement of the Reynolds numbers in the model and in reality

$$Re_m = Re \tag{1}$$

it follows that

$$V_m = \left(\frac{\nu_m}{\nu}\right)\left(\frac{D}{D_m}\right)V \tag{2}$$

If material properties of the gas in the model and in the real system are identical, the velocities in the small scale model must be increased by the inverse of the geometrical scale factor i.e. in our case by a factor of 8.8333. In the model, the air is at room temperature level, while in the real furnace combustion gases are at elevated temperatures. The material properties are affected both by composition and temperature differences. However in case of "dilute" flames, the temperature effect is much stronger than the effect of concentration variation. To estimate the influence of the material properties, the properties of air at room temperature, 20 °C, are compared to air properties at 800 °C using data from Ref. [48].

$$\rho_{20^\circ C} = 1.1881 \text{ kg/m}^3$$

$$\rho_{800^\circ C} = 0.3243 \text{ kg/m}^3$$

$$\nu_{20^\circ C} = 15.13.10^{-6} \text{ m}^2/\text{s}$$

$$\nu_{800°C} = 133.6.10^{-6}\ m^2/s$$

$$\mu_{20°C} = 17.98.10^{-6}\ kg/m.s$$

$$\mu_{800°C} = 43.32.10^{-6}\ kg/m.s$$

The ratios of the material properties and the dimensions are consequently:

$$\nu/\nu_m = 8.830$$

$$\mu/\mu_m = 2.409$$

$$\rho/\rho_m = 1/3.664$$

$$D/D_m = 8.833$$

Substituting these values into Equation (2), one can find that the characteristic velocities in the model must be approximately equal to those in the real furnace.

Other important flow parameters have different scaling laws which can also be derived from Equation (1) and from the definitions of those parameters.

2.3.3.1 Ratio of volumetric flow rates

$$\frac{\dot{V}_m}{\dot{V}} = \left(\frac{\nu_m}{\nu}\right)\left(\frac{D_m}{D}\right) \approx \frac{1}{80} \tag{3}$$

2.3.3.2 Ratio of mass flow rates

$$\frac{\dot{m}_m}{\dot{m}} = \left(\frac{\mu_m}{\mu}\right)\left(\frac{D_m}{D}\right) \approx \frac{1}{21} \tag{4}$$

2.3.3.3 Ratio of momentum flow rates

$$\frac{\dot{I}_m}{\dot{I}} = \left(\frac{\mu_m}{\mu}\right)\left(\frac{\nu_m}{\nu}\right) = \left(\frac{\rho_m}{\rho}\right)\left(\frac{\nu_m}{\nu}\right)^2 \approx \frac{1}{21} \tag{5}$$

2.3.3.4 *Remarks*

• The numerical match between the scaling factors of the mass and momentum flow rates is simply the result of the special choice of the geometric scale to be practically identical to the kinematic viscosity ratio (at the given temperature levels).

• In case of dynamic similarity, the scaling factor of the momentum flow rate depends solely on the material properties, not on the geometry.

• The above assumptions do not take care of the buoyancy effects, which will be treated in the next section.

2.3.4 Modelling of the Buoyancy Effects

In a cold flow model the effect of thermal buoyancy cannot be reproduced. An approximate imitation of the effect is possible by reducing the density by the mixing of some lighter gas (for example hydrogen or helium) into the air at the inlet.

The buoyancy driven natural convection is characterized also by a number of dimensionless groups. The buoyancy due to any type of density differences in the gravitational field is described by the Archimedes number :

$$Ar = \frac{g\,L^3}{\nu^2}\,\frac{\Delta\rho}{\rho} \tag{6}$$

where g is the acceleration of the gravitational field and $\Delta\rho$ is the density difference due to any cause. From the definition of density and that of the thermal expansion coefficient β, it follows that $\Delta\rho = -\rho\,\beta\,\Delta T$, the momentum source term due to the thermal expansion can be introduced, leading to the well-known Grashof number :

$$Gr = \frac{g\;L^3\,\beta\,\Delta T}{\nu^2} \tag{7}$$

Both the above dimensionless numbers characterize the ratio of buoyancy forces to viscous forces; only the density variations in their expression have different origins.

Let us examine how much helium should be added to the inlet air to model a given ΔT temperature difference in the real furnace (Although it would be the best additive, the application of hydrogen has been discarded due to the safety hazard).

The criterion of similarity is

$$Ar_m = Gr \tag{8}$$

From basic thermodynamic relations, using the properties of air and helium, one can easily derive a formula for the relative density difference of the mixture to pure air,

$$\left(\frac{\Delta\rho}{\rho}\right)_{model} = \frac{\rho_{mix} - \rho_{air}}{\rho_{air}} = -0.862\, x_{He} \tag{9}$$

where x_{He} is the volume fraction of helium in the mixture. In other words, this means that for reaching a given relative density difference $\Delta\rho/\rho$, one should add approximately 16% higher volume fraction of He to the air. By substituting the above relation into the similarity criterion and using the value of the thermal expansion coefficient at 800°C, β=9.32×10^{-4} K^{-1},

$$x_{He} = 1.08 \cdot 10^{-3}\, \Delta T \tag{10}$$

With pure helium jet entering an air space (x_{He}=1.0), we can imitate the effect of approximately 900°C temperature difference. However, the practical realization of this effect is not without difficulties: if all the burners are delivering helium into the internal flow chamber of the model, after a short period of time all density differences disappear as helium replaces the air inside. To maintain the density difference, only one or a few burners but not all of them should be fed by the light gas mixture. This method can provide a physically adequate picture about the influence of the buoyancy forces on the behavior of the individual jets.

The above outlined methodology is of utmost importance when the influence of the natural convection on the general flow pattern is dominant or at least comparable to the influence of the forced convection.

There is no *a priori* theoretical or experimental information about the range and ratio of the Reynolds and Grashof numbers to decide whether the forced or natural convection dominates in a flow field. A comparison of the numerical values in itself is senseless without the exploration of the flow structure, as those values can cover several orders depending on the more or less arbitrary choice of characteristic lengths, velocities, temperatures etc.

However, the range of uncertainty can be significantly reduced, if instead of the separate analysis of Re and Gr values, a physically sound combination (for example the ratio) of them is introduced.

The appropriate dimensionless group for describing the relation of buoyancy to the kinetic energy dominated flow in flames and combustion phenomena is the so-called Richardson number :

$$Ri = \frac{Ar}{Re^2} = \frac{g\,L}{V^2}\,\frac{\Delta\rho}{\rho} \tag{11}$$

This dimensionless group reflects the experience that natural convection flows are reacting sensitively to external forced ventilation effects and the effect of the disturbance is increasing with the square of the external velocity. Energetically this number relates the changes in the potential energy to the kinetic energy.

In flames and non-isothermal free jets the local value of the Richardson number increases with the distance from the mouth of the burner (nozzle), as the velocity decreases. The relative value of the buoyancy forces to the inertia forces increases toward the tip of the

flame, which is demonstrated by the rising of the tip and usually ***only*** the tip of the flame. This indicates the fact that the influence of the lifting forces due to thermal expansion is not uniform in the whole flow field.

Experience in many furnaces and combustion chambers shows that in the case of high-momentum burners even the local effect of the buoyancy on the tip of the flame is often suppressed.

The importance of the use of the Richardson number is that it shows the way how the density difference can be "compensated" by velocity variations. Obviously without any density difference the natural convection cannot be modelled, but when perfect modelling is not possible due to certain reasons, the decrease of flow velocity can effectively help to maintain the *Ri* number at a required level. When doing this, it is very important to explore the limits of the domain of the Reynolds number within which the flow pattern does not undergo a qualitative change. For this reason we tested the effect of velocities below the nominal value during modelling.

We found earlier that for modelling natural convection alone, injection of pure helium into air can approximately model buoyancy forces for about 900°C. In modelling forced and natural convection together, the requirement of matching *Re* and *Ri* simultaneously imposes a further restriction.

From

$$Ri_m = Ri \tag{12}$$

it follows that

$$\frac{\left(\frac{\Delta\rho}{\rho}\right)_m}{\left(\frac{\Delta\rho}{\rho}\right)} = \left(\frac{D}{D_m}\right)\left(\frac{V_m}{V}\right)^2 = \frac{0.862\, x_{He}}{\beta\,\Delta T} \tag{13}$$

If Re_m = Re is also satisfied, then the relation between the volumetric fraction of helium required to model a ΔT temperature difference becomes

$$x_{He} = 9.55 \cdot 10^{-3} \Delta T \tag{14}$$

instead of the correlation for matching Grashof and Archimedes numbers only (Equation 10). This correlation reduces the maximal temperature difference modelled by pure helium jets to approximately ΔT=105 °C.

2.3.5 Ratio of Residence Times in the Model and Real Furnace

The residence time of a gas particle is

$$\tau = \int_0^L \frac{dl}{V} \tag{15}$$

where l is the length parameter along the individual path of the particle, the integration from 0 to L is related to the total length of the path from the mouth of the burner to the stack and V is the velocity of the particle along the path. Applying the condition of the dynamic similarity and performing the integration in both the model and the real furnace we obtain (also using the material properties of air at 20°C and 800°C)

$$\frac{\tau_m}{\tau} = \left(\frac{D_m}{D}\right)^2 \left(\frac{\nu}{\nu_m}\right) \approx \frac{1}{8.83} \tag{16}$$

This correlation can also be directly obtained from the isochronity criterion (*Strouhal number*), as one possible form of that dimensionless group is

$$St = \frac{D}{\tau V} \tag{17}$$

The simultaneous match of the Strouhal and Reynolds numbers leads to the same relation as Equation (16).

2.4 THE EXPERIMENTAL METHODS

There are numerous methods to visualize flow phenomena. Some of them show streamlines, others only individual paths, some show the flow structure in the whole volume while others only along solid surfaces or in selected sections. These techniques are classified into four groups in table 2.1 : wall tracing, tuft, tracer and optical methods.

Method	Type
WALL TRACING	Liquid film
	Sublimation
	Thermosensible paint
	Electrolytic etching
	Soluble chemical film
TUFT	Surface tuft
	Tuft grid
	Depth tuft
TRACER :	
Direct injection	Solid particles
	Liquids
	Gases
Chemical reaction	Chemical
	Electrolytic
	Photochemical
Electrical	Hydrogen bubble
	Spark
	Smoke wire
OPTICAL	Shadowgraphy
	Interferometry
	Holography
	Liquid crystal

Table 2.1 Conventional flow visualization methods

2.4.1 Fluorescent Mini-Tuft Technique

Originally developed for aerospace research, this is a surface flow visualization technique. The small tufts fixed to the surface at one end serve as the point indicator of flow direction. The application of ultraviolet illumination and fluorescent dyes on the marker elements improves the visibility of the tufts.

In our implementation, small polystyrene foam balls were attached to the free end of the tufts. The application of these end pieces helped to increase the aerodynamic drag on the tuft and to separate the self generated whipping motion from real flow fluctuations.

The tufts were attached in a regular, relatively dense array over the solid surfaces in the model and were illuminated by ultraviolet lamps. It took some efforts to introduce the UV light uniformly into the interior of the model, as the plexiglass walls transmit UV very weakly. Finally a set of UV lamps and an array of metallic reflectors were installed (see Figure B.1, Appendix B).

The visible light from the tufts was recorded on photo and video. However, the relatively low light level does not permit short exposure times during recording.

The fluorescent tuft method provides the following informations :

• The direction of the near surface flow velocity vectors along the solid surfaces with a good resolution.

• The visualization of vortex zones, flow separation, flow reversals.

• By applying an appropriate, relatively long (20-100 ms) exposure time, the blurred image of certain tufts or certain tuft regions indicates higher level of turbulent fluctuations, like in case of separation zones. This can also be an indication of enhanced surface heat transfer.

2.4.2 "Pop Corn" Method

In this technique relatively large (roughly 1 cm diameter) polystyrene balls are dumped into the fluid dynamic model. These particles **are not** tracers, as they are not able to follow the path of gas particles. They fly along a polygon-like criss-cross pattern in the furnace. This movement results in a rearrangement of their distribution within the model, along the furnace floor. The resulting pattern of the rearrangement is independent of the initial distribution of the foam particles, and is preserved even after the gas flow is stopped. The particles are sedimenting fast in low velocity regions, and are deposited on the floor in those areas, where the horizontal component of the velocity is minimum (flow stagnation).

The pattern of these stagnation or dead zones is characteristic to each burner arrangement and orientation. The presence of these stagnation zones is most characteristic to the non-rotating flows (see Figure B.2, Appendix B).

The useful output of the "pop corn" technique :

• The shape and location of stagnation zones (dead zones) along the horizontal surfaces.

2.4.3 Smoke Visualization with Laser Sheet Illumination

The technique was well introduced in an earlier report by Kiss et al. [22]. We applied the fog in short bursts, as after a short time the flow chamber gets saturated and further observation is blocked by the tracer itself. This method can also give an indication about the residence time. During the experiments the fog was introduced only through one or two of the burners, while all of them were operating to facilitate the observation of the behavior of the individual jets (see Figures B.3 - B.14, Appendix B).

Most of the smoke visualization experiments were done by planar (horizontal or vertical) laser sheet illumination, but the observation of the complicate three-dimensional,

curved jet shapes made the application of diffuse illumination a necessity.

The type of results obtained from smoke visualization :

• Visualization of the overall flow structure, main regions, individual jet behavior, either in planar sections (laser sheet) or in three dimensions (diffuse illumination).

• Qualitative estimation of residence time, by exploiting the observation of a transient, short-burst fog injection.

2.4.4 Photographic and Video Recording

The main difficulty encountered during the two years of the project was represented by the struggle with the low light levels, to bring the sensitivity of various recording techniques into harmony with our potential to provide sufficient intensity and contrast of illumination.

Traditional photo recording techniques were not adequate for recording smoke visualization images. In the case of the fluorescent mini-tuft technique, relatively long exposure times allowed us to use color photography (400 ASA), but the fixed frame rate (30 f/s) of ordinary video does not provide too much latitude in this application.

We performed many experiments using extremely fast black & white film (Kodak TMAX 3200) with push-processing up to 12500 ASA, but the quality of the results was not appropriate. Therefore, we decided to use electronic image recording as a basic tool. Although the resolution of video recording cannot compete with traditional photography, it is not much inferior to that of the push-processed ASA 12500 film, and at the same time it provides the recording of evolution of the flow in time.

The interaction between the jets generates fluctuations in the flow into the furnace chamber. These fluctuations are affecting mass exchange and momentum transfer mechanisms. The analysis of the fluctuations, the formation of the so-called coherent structures,

which are generated in the flow periodically but which preserve their individual identity only for a short time (sometimes only for 50-100 ms), require the application of high speed recording. At high recording rate the light energy is further reduced by the short exposure times below the threshold sensitivity of any conventional photographic recording technique.

For recording and analyzing the transient behavior of the flow, finally we used the KODAK Ektapro intensified imager and high speed video recording system, which provided an extreme flexibility in accommodating our experimental conditions. The maximum sensitivity of the intensified imager is equivalent to 500000 ASA, which made possible the use of low intensity diffuse illumination (to avoid reflections and to prevent the melting down of the plexiglass walls of the model) in conjunction with high speed recording, up to a rate of 1000 frames/second, and down to 1 microsecond exposure time (see Figures B.15 - B.17, Appendix B).

2.5 FLOW STRUCTURE

To illustrate the description of the findings about the flow structure, we provide a few photos and line drawings. However we call to attention that the two video films [21,28], described in Appendix A, form integral part of this flow visualization study, and provide the most comprehensive illustration to the text [23].

All the visualization experiments with the fluid dynamic model of the furnace have been performed for flat bath conditions and for maximum metal level. Basically the smoke visualization technique with laser sheet illumination was applied, but certain experiments were done in diffuse light, and the application of the "pop corn" technique also complemented the studies.

Traditional photographic recording did not give satisfactory quality even with the 12500 ASA TMAX film, but the refinements in smoke generation and in the optical system finally gave good conditions for ordinary (30 frame/sec) video recording.

During the experiments we arrived to the conclusion that dynamic effects, self-generated fluctuations play an important role in the mass exchange processes, as they can even affect the residence time. The high speed video photographic technique described earlier provided the necessary time resolution to study the dynamics of directional oscillations of the jets and made possible the "freezing" of the image of the instantaneously changing shape of the jets, core etc.

Smoke was applied in short, consecutive bursts during the experiments, through only one selected burner, but air was supplied through all the six burners.

The most important, easy-to-recognize characteristic of the flow is the formation of a large swirl inside the circular chamber of the furnace. It is possible to distinguish three main regions or elements of the flow:

• The "**doughnut**" shaped toroid-like flow, which has approximately 1/3 diameter core in its centre (see Figures B.9 - B.11, Appendix B). This steadily rotating flow is driven by the jets from the six burners like a "turbine wheel". Within this toroidal flow a strong mixing is present, so the velocity is not changing radically across the cross section. The radial velocity distribution has a maximum, and is decreasing rapidly in the boundary layer near the external cylindrical wall, and more slowly toward the centerline of the furnace. Due to this cross-mixing (turbulence), the trace of the individual jets cannot be recognized.

• In the center of the "doughnut" is the **core** of the swirl. The core behaves similarly to the motion of a rotating solid body (like a "plug"), i.e. the tangential velocity within the core

is roughly proportional to the radius. The radial velocity components are generally small in the core. Also, the radial mass and energy transfer is enhanced only by the fluctuating interaction of the individual burners, which occasionally can penetrate slightly into the core (see Figures B.9 - B.11, and B.14 in Appendix B and the video about the star-shaped coherent structures in the core).

The part of the flow which reaches the core either after a long, smooth, spiralling-in motion or as a result of the temporary "break-ins" from the jet fluctuations, stays there for a long time. The "escape" from the core is the result of several effects:

a. during the fluctuating interactions with the individual jets, small "gas-packages" are exchanged between the toroidal part and core,

b. there is some weak vertical circulation pattern in the core, which conveys gas to the top of the furnace, where a part of the gas can slowly find its way toward the stack in the boundary layer just under the roof, and

c. there is also the molecular transport, but it is even weaker than the above mentioned mechanisms.

• The third important element of the rotating flow structure is the **merging region** of the individual jets (see Figures B.3 - B.8, Appendix B). We introduced this concept to describe that portion of the flow where the different jets preserve their individual character before being completely united and mixed with the high-momentum rotating toroid.

The individual jets have three important momentum components at the exit of the burners: tangential, radial-inward and vertical-downward. After a relatively short travel, the radial and vertical components disappear, the jet merges completely into the toroidal flow. The kinetic energy associated with the radial and vertical degrees of freedom is

converted either into the rotational energy of the "doughnut" (acceleration), or into the random turbulent fluctuations which promote the cross-mixing.

From the top view, the gasses in the merging jet follow a question mark shape, but in three-dimension the flow pattern is more complicated (see Figures B.15 - B.17, Appendix B). The inward and downward pointing jet turns upward when reaching the bath surface by impingement, and then makes a half turn upward and slightly outward, roughly like a half-wind of a helix on the surface of a torus. After this half-turn, the gases reach the extremity of the torus, coming close to the external cylindrical wall of the furnace. At this point the cross section of the jet is nearly the same as that of the doughnut. The jets gradually increase their cross section in the merging region due to the mass and momentum exchange processes which slow them down and transversely distribute their material.

Chapter 3

DEVELOPMENT OF THE TECHNIQUE

3.1 DESCRIPTION OF THE TECHNIQUE

In this section, an overview of the heated skin technique developed to obtain heat transfer measurements in a circular remelting furnace is presented.

The technique is based on the ability of the foil heaters to generate a nearly constant heat flux surface as well as the division of the surface into many individually controlled heated sections (seventeen sections) making possible the generation of the constant temperature surfaces. This technique involves inverse heat flow conditions, since in the model the gas is at lower temperature than that of the surfaces. The foil heaters are attached to a horizontal circular plate (made of low thermal conductivity material, "styrofoam"), which simulates the molten metal flat bath over which the convection and radiation heat transfer measurements are to be made (see Figure 3.1). When a voltage is applied across the etched foil heater of uniform electrical resistivity, a uniform current flows through it, and generates a uniform heat flux surface.

Convective heat transfer coefficient at the interface between the heating element surface and the fluid (air) may be determined by measuring the surface temperature and heat flux at points of interest.

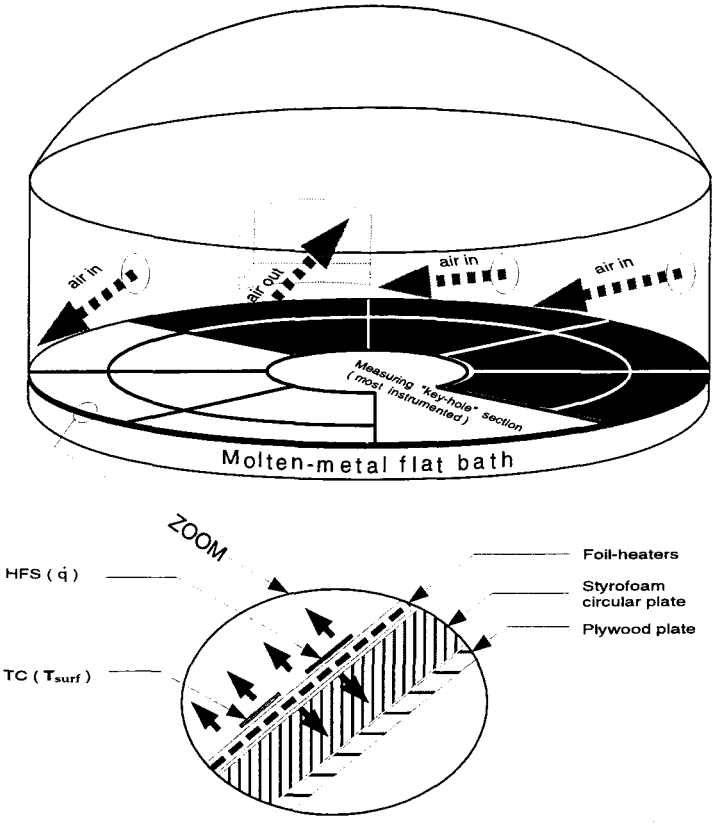

Figure 3.1 Heated skin technique

In order to determine the convective and radiative heat transfer coefficients distinguishably, two sets in a group of three heating elements, forming a shape like a key hole, with extremely different surface emissivities, are prepared (see Figure 3.2),i.e. one set (key hole section) is painted black to increase the emissivity of the surface (≈ 0.95) to measure the radiative and convective heat transfer coefficients, and the other set was left with an aluminum shiny surface of emissivity ≈ 0.04. Foil thermocouples (chromel-alumel) were glued on all the seventeen heating element surfaces to measure the local surface temperature. The measuring "key hole" section was better instrumented, i.e. more thermocouples as well as micro-foil heat flux sensors were installed in order to get more heat transfer data points along the radius.

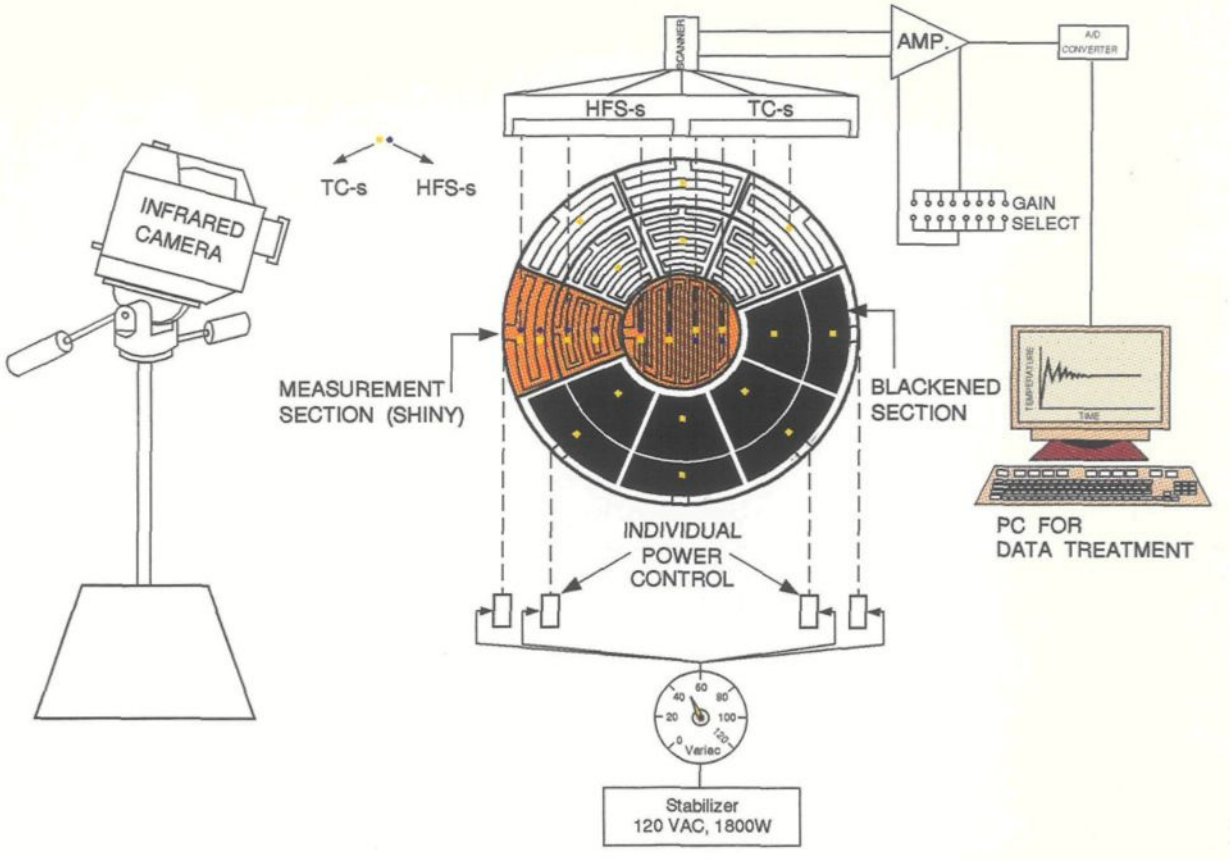

Figure 3.2 Schematic overview of the experimental set-up

All the seventeen heaters are installed on a 25 mm thick styrofoam circular disk of 1.12 m diameter, the free inner diameter of the scaled model. Styrofoam was selected for this purpose because of its low thermal conductivity which reduced downward heat losses. In addition to the styrofoam disk, a 13 mm thick plywood disk of the same surface area as that of the styrofoam disk was also used to provide hard backing to the styrofoam disk and consequently to the heaters (see Figure 3.2).

The power to the heating elements was fed through an AC power stabilizer, which provides a non-fluctuating power supply, and a variac to regulate the input voltage. Seventeen rheostats, each capable of dissipating 15 to 25 Watts, are introduced in the

circuit to control the heating elements individually, to generate constant heat flux as well as constant temperature surfaces (see Figure 3.3).

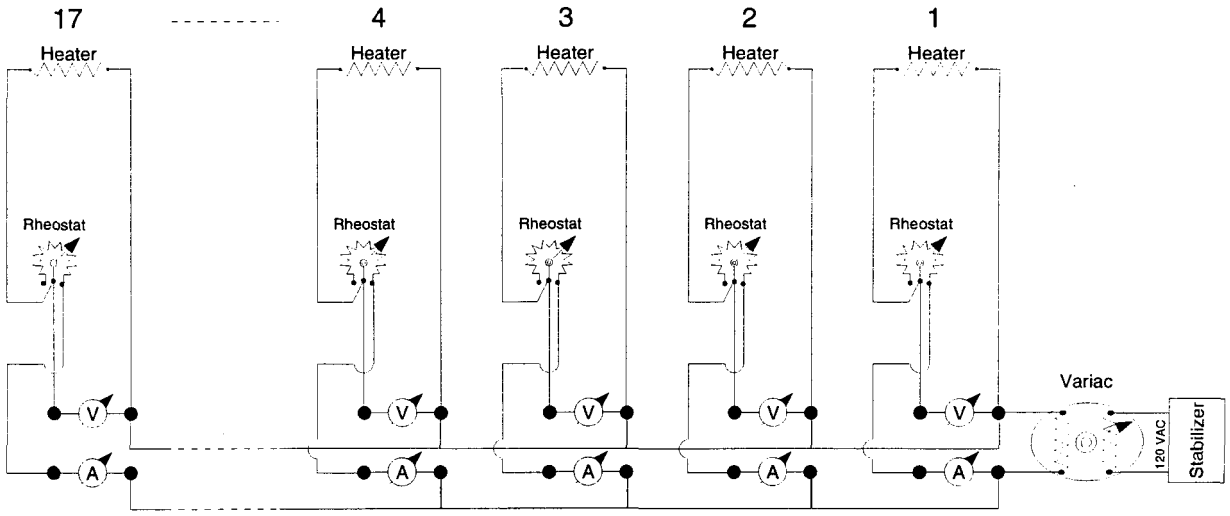

Figure 3.3 Electrical connections of rheostats and heaters

The local convective heat transfer coefficient is defined as:

$$h_{conv} = \frac{\dot{q}}{T_{surf} - T_{air}} \tag{18}$$

and the Nusselt number, or non-dimensional heat transfer coefficient, is defined by the following equation:

$$Nu = \frac{h_{conv} L}{k_{air}} = \left[\frac{\dot{q}}{T_{surf} - T_{air}}\right]\left[\frac{L}{k_{air}}\right] \tag{19}$$

where:

k_{air} is the thermal conductivity of the air (W/m.K),

L is the appropriate reference length (m),

$\dot{q}$ is the heat flux (W/m^2),

T_{surf} is the local surface temperature (K), and

T_{air} is the inlet air temperature (K).

The radiative heat transfer coefficient is defined as:

$$h_{rad} = \frac{\epsilon\sigma\left(T_{surf}^4 - T_{air}^4\right)}{T_{surf} - T_{air}} \tag{20}$$

or

$$h_{rad} = \epsilon\sigma\left(T_{surf} + T_{air}\right)\left(T_{surf}^2 + T_{air}^2\right) \tag{21}$$

where:

ϵ is the emissivity of the surface, and

σ is the Stefan-Boltzmann constant.

3.2 SUPPORTING EQUIPMENT AND INSTRUMENTATION

Various equipment and instrumentation used in this heat transfer study are described in the following sub-sections.

3.2.1 Foil Heaters

The foil heaters employed in this work are manufactured by Minco Products Inc. These heaters are thin, flexible heating elements, consisting of an etched-foil resistive element laminated between layers of flexible insulation and aluminum foil. According to the manufacturer, the heating elements are stable to about 200°C.

Here are the main specifications of the foil heaters used in this study:

1. The total thickness of the insulating layer, aluminum foil, and etched foil is 0.76 mm.
2. The electrical resistance of the central heating element is 86.7 Ω and 173.5 ±0.5% Ω for the other elements.
3. The insulating material used for lamination is silicone rubber.

The foil heaters were always handled with great care during the installation as well as through the entire serie of experiments to avoid making smudge marks and fingerprints on the surface of the heating elements.

The foil heaters were glued to the surface of the styrofoam disk by using a factory applied adhesive (peeled-off protective backing).

3.2.2 Temperature Measurement

All quantitative temperature measurements in this work were obtained using chromel-alumel foil thermocouples, manufactured by Rdf Corporation. They are thin foil thermocouples, with butt-bonded junctions which provide accurate and fast response sensors for the surface temperature measurements.

They are available in a free filament style with removable carrier and in a matrix type with sensor embedded in paper thin laminate. The main characteristics of these thermocouples are:

1. The foil thickness is 0.005 mm.
2. The dimensions are 19 mm by 9 mm.
3. Matrix type with sensor embedded in paper laminate (see Figure 3.4)

These foil thermocouples were glued on the surface of the heated skin, and were connected to the data acquisition system to monitor the surface temperatures (see Figure 3.4).

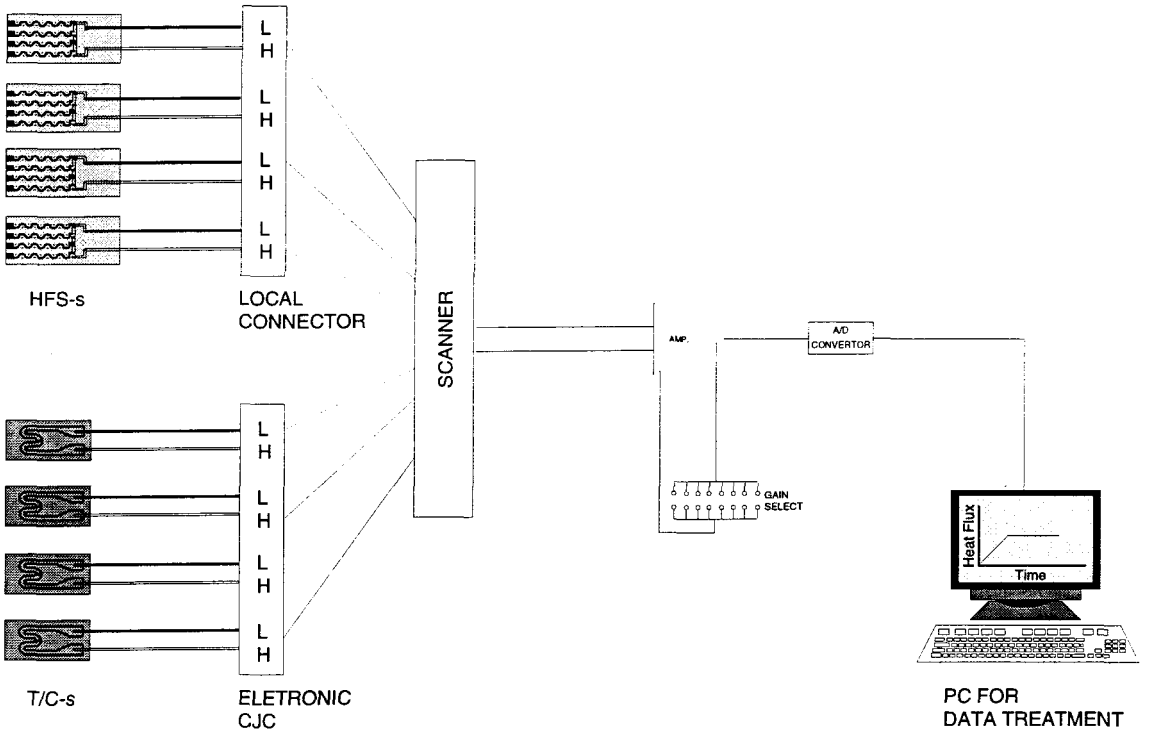

Figure 3.4 Connections of TC-s and HFS-s to the data acquisition system

A chromel-alumel thermocouple made of 30-gauge wires (Omega Engineering Inc., GG-K-30) was also prepared in the laboratory to check the above mentioned foil thermocouples. The procedure used to fabricate the thermocouple was as follows:

1. About 8 mm of insulation was removed from one end of the wires.
2. The last 4 mm of the chromel and alumel wires were twisted tightly together with the help of pliers.
3. The ends of the twisted wires were cut, leaving just enough wire at the end to make a bead with a thermocouple welder.
4. The wires were welded together.
5. The wires were glued apart above the bead, to ensure that they could not make contact.

In order to check the reliability of the thermocouples obtained from different sources, a cylindrical copper block of 170 mm in diameter and 140 mm thick was constructed to hold all the thermocouples (foil thermocouple from Rdf, thermocouple embedded with HFS from Rdf, Omega thermocouple prepared in the lab and a laboratory thermometer with precision of ± 0.1°C) at the same temperature. All the three thermocouples and the thermometer were placed on the top surface of the copper block at equal distance from the centre and were connected to data acquisition system to monitor the temperatures. The block was completely covered with 75 mm thick styrofoam sheet to avoid non-uniform cooling of the apparatus by forced convection due to surrounding air movement. The block was then heated uniformly and the measurements were taken at various temperatures. The difference among the thermocouples and the thermometer were found to be lower than ± 0.4°C.

3.2.3 Heat Flow Measurement

Micro-foil heat flow sensors (manufactured by Rdf Inc.) were used to measure heat flux. The sensors are very thin and flexible and can be attached to flat or curved surfaces without damaging them. The micro-foil heat flow sensor is designed for the precise measurement of heat loss or gain on any surface. It employs butt-bonded junctions with a very low thermal profile for efficient reading.

The sensor is available with or without an integral thermocouple for discrete measurement, and in two different sensitivity ranges. Here are the main characteristics of this sensor:

1. The upper temperature limit is 204°C.
2. There are 40 junctions.

3. The chromel-alumel thermocouple is integrated with the sensor.
4. The carrier material is a polyamide film (Dupont Kapton).
5. The nominal thickness is 0.457 mm.
6. The nominal sensitivity is provided for individual sensor and is in the range of 2 $\frac{\mu V}{W/m^2}$
7. The response time is 0.7 second.
8. The thermal resistance is 0.004 $\frac{^{\circ}C}{W/m^2}$

The micro-foil heat flux sensors were attached on the key hole section. Each foil heater in the key hole section was equipped with two equidistant sensors. These sensors were then connected to the data acquisition system to monitor the heat flux values at the points of interest (see Figure 3.2).

3.2.4 Rheostats

The rheostats used in this study are manufactured by Ohmite Manufacturing Company. These rheostats are designed to operate smoothly and reliably over long periods of use. Different models are available, specifications of the rheostats used in this work are as follows:

1. The electrical resistance tolerance is ± 10%.
2. The resistance and amperage of the rheostat used for central heating element are 15 Ω, 1.29 A and that for all others are 25 Ω, 1.0 A.
3. The overall dimensions are 10 mm in diameter and 38 mm in thickness.
4. The contact material is metal graphite composite.
5. The body is made from ceramic.

The rheostats were connected in series with the heating elements (one to one connection) to control the heaters individually, thus allowing the generation of constant heat flux as well as constant temperature surfaces (see Figure 3.3).

3.2.5 Multimeters

Six multimeters were used to measure the voltage and current to the three foil heaters forming the key hole section, and one multimeter was kept handy to measure the voltage and current of the remainder of the heating elements.

The multimeters used in this work were manufactured by ECG Inc. (digital multimeter, model: DM-38). In the 20 A range, these units have a resolution of 10 mA and accuracy ± 2% of four digits reading; and the voltage measurement in the 400 V range, has a resolution of 100 mV and accuracy ± 1.0% of four digits reading.

3.2.6 Variac (Variable Autotransformer)

A variac was used in this study to control voltage across the foil heaters. It was manufactured by POWERSTAT, The Superior Electric Company. This unit is capable of supplying 0 to 120 volts, but the voltage range across the heaters was restricted from 0 to 70 volts.

3.2.7 Power Stabilizer

A power stabilizer was used to avoid power fluctuations. This was manufactured by TRIPP LITE, The Power People (model: LC-1800). The unit is capable of supplying 1500 W of power. This unit supplies stable output in the input range of 87 to 140 volts and 60 Hz. It was connected to the heating elements through a variac (see Figures 3.2 and 3.3).

3.2.8 Data Acquisition System

A data acquisition unit (MetraByte Corporation, DASH-8) was used to take thermocouple and heat flow sensor voltage readings [34].

A data acquisition or computer interface system is a device that permits to feed data from the real world to a computer. It takes the signals produced by temperature sensors, pressure transducers, flow meters etc, and converts them into a form that the computer can understand.

Thermocouple and heat flow sensor voltage measurements were taken using three relay multiplexer assemblies (MetraByte Corporation, EXP-16). Each assembly contains 16 measurement channels on a isothermal connector block (see Figure 3.5).

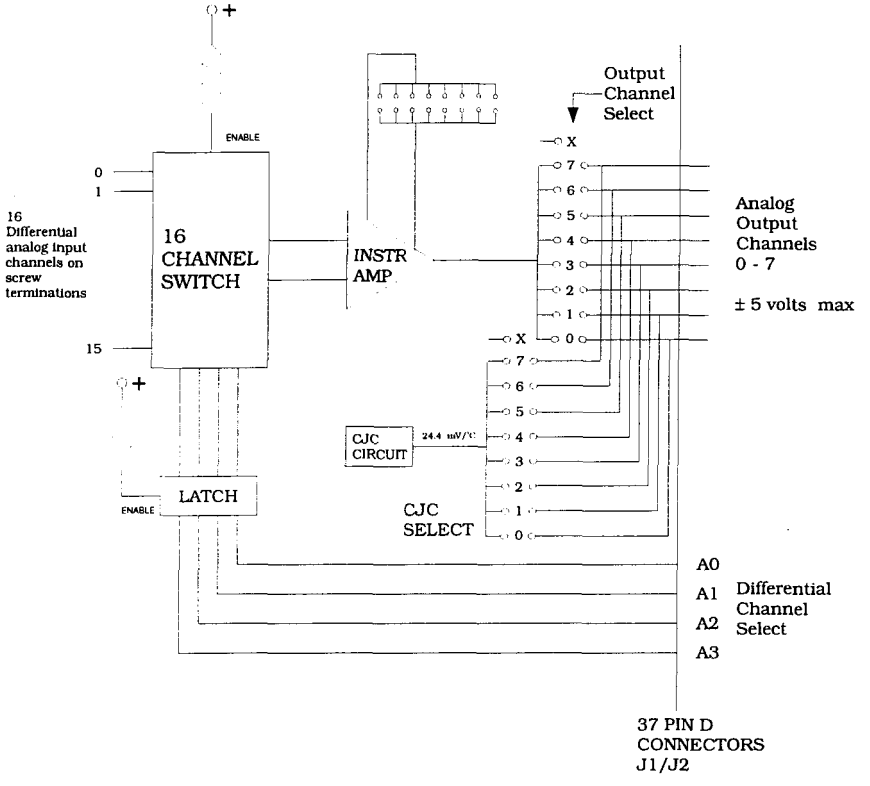

Figure 3.5 Block diagram of the multiplexer EXP-16

Low level transducers, such as thermocouples or heat flux sensors, require significant amplification. The EXP-16 expansion multiplexer incorporates an instrumentation amplifier that provides stable amplification and also includes circuitry that allows cold-junction compensation of thermocouples. Circuitry is provided on-board to produce a + 24.4 mV/°C (0.1 °C/bit) compensation signal with a 0.0 volt output at 0 °C. The gain switch on each EXP-16 configures the entire board for the gain selected. Gains of 0.5, 1, 2, 10, 50, 100, 200 and 1000 are available. The gain of 1000 was selected for the thermocouples and that of 100 was set for the heat flow sensors.

A software package called "LABTECH NOTEBOOK" was used to perform several functions,i.e. data acquisition and process control, storage and screen display of experimental data, data manipulation and curve fitting.

3.2.9 Hot-Film Anemometer

The technique used to measure the air velocity in the furnace chamber is the hot-film thermal anemometer, manufactured by TSI Incorporated (Velocicheck, model 8330). A fine film is heated electrically and placed in the flow stream. When the air stream passes through the sensor, the electric current increases to maintain the same temperature.

The early work of King [20] as cited in Ref. [18] has shown that the heat transfer rate from the film can be expressed in the form :

$$q = \left(a + bu^{0.5}\right)\left(T_f - T_\infty\right) \tag{22}$$

where

T_f = film temperature, K

T_∞ = free stream temperature of fluid, K

u = fluid velocity, m/s

a,b = constants obtained from a calibration of the device

The heat transfer rate must also be given by

$$q = i^2 R_w = i^2 R_0 \left[1 + \alpha(T_f - T_\infty)\right] \tag{23}$$

where

i = electric current, A

R_0 = resistance of the film at the reference temperature T_0, ohm

α = temperature coefficient of resistance, K^{-1}

For measurement purposes the hot film is connected to a bridge circuit, as shown in Figure 3.6.

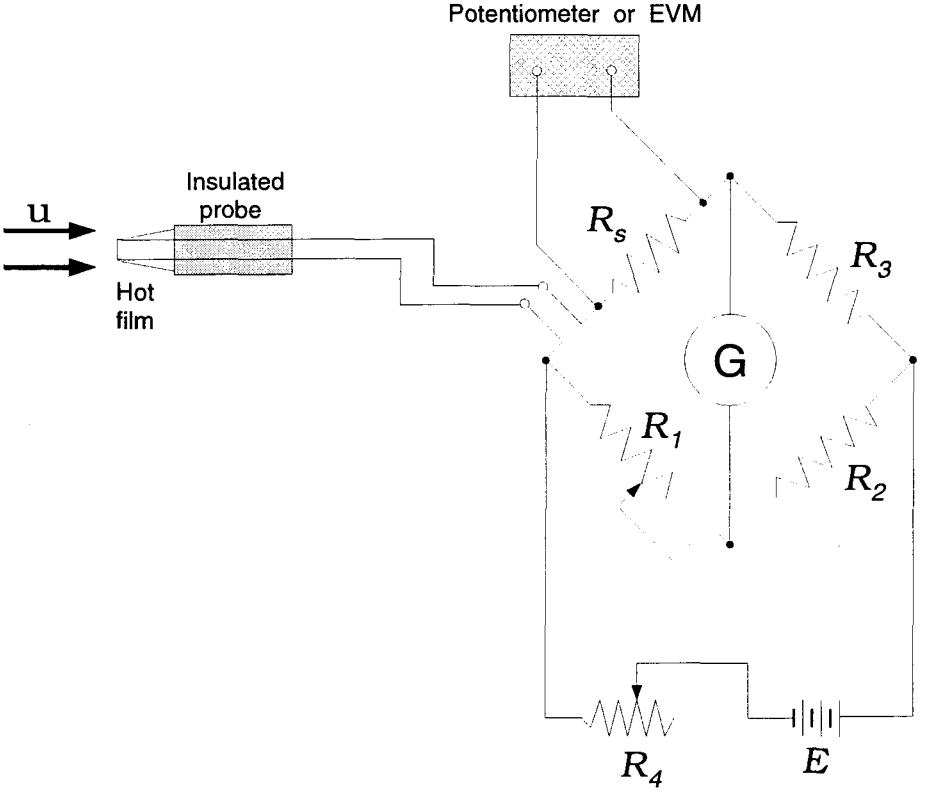

Figure 3.6 Circuitry of the hot-film anemometer

The current is determined by measuring the voltage drop across the standard resistance R_s, and the film resistance is determined from the bridge circuit. For steady state measurements the null condition is used, while an oscilloscope output may be used for transient measurements. With i and R_f determined, the flow velocity may be calculated with equations (22) and (23).

The instrument used in this work displays numerically both the air flow velocity and the air stream temperature.

3.3 DESCRIPTION OF THE MODEL

The model used in this study is a reduced scale (1:8.83) model of a 10 m diameter circular top-charged remelting furnace. It was manufactured by using a transparent material (plexiglass) to facilitate visual observation inside the entire furnace chamber. The model was built with a strong attention to the correct geometric similarity even in close details around the door and stack region (see Figures C.1 and C.3 in Appendix C).

There are six burners located along the periphery of the circular vertical wall at the designed circular angles. The burners are of the ball-joint design to facilitate their orientation. The upper perimeter of the model is equipped with a precise angular division from 0-360 degrees. Burner orientation in the original position can be seen in the Figure 3.7.

The internal floor plate in the model (see Figure 3.1) represents the molten metal level in the real furnace. Its vertical height is adjustable in order to model different operating conditions.

The adjustment of the flow velocity is based not on the velocity measurement inside the furnace model, but using the scaling law for the flow rates. A flow rate measuring

section was specifically built for this purpose, and the non-standard orifice was calibrated using Laser Doppler Anemometer by Hugues Boily, as a part of his undergraduate studies.

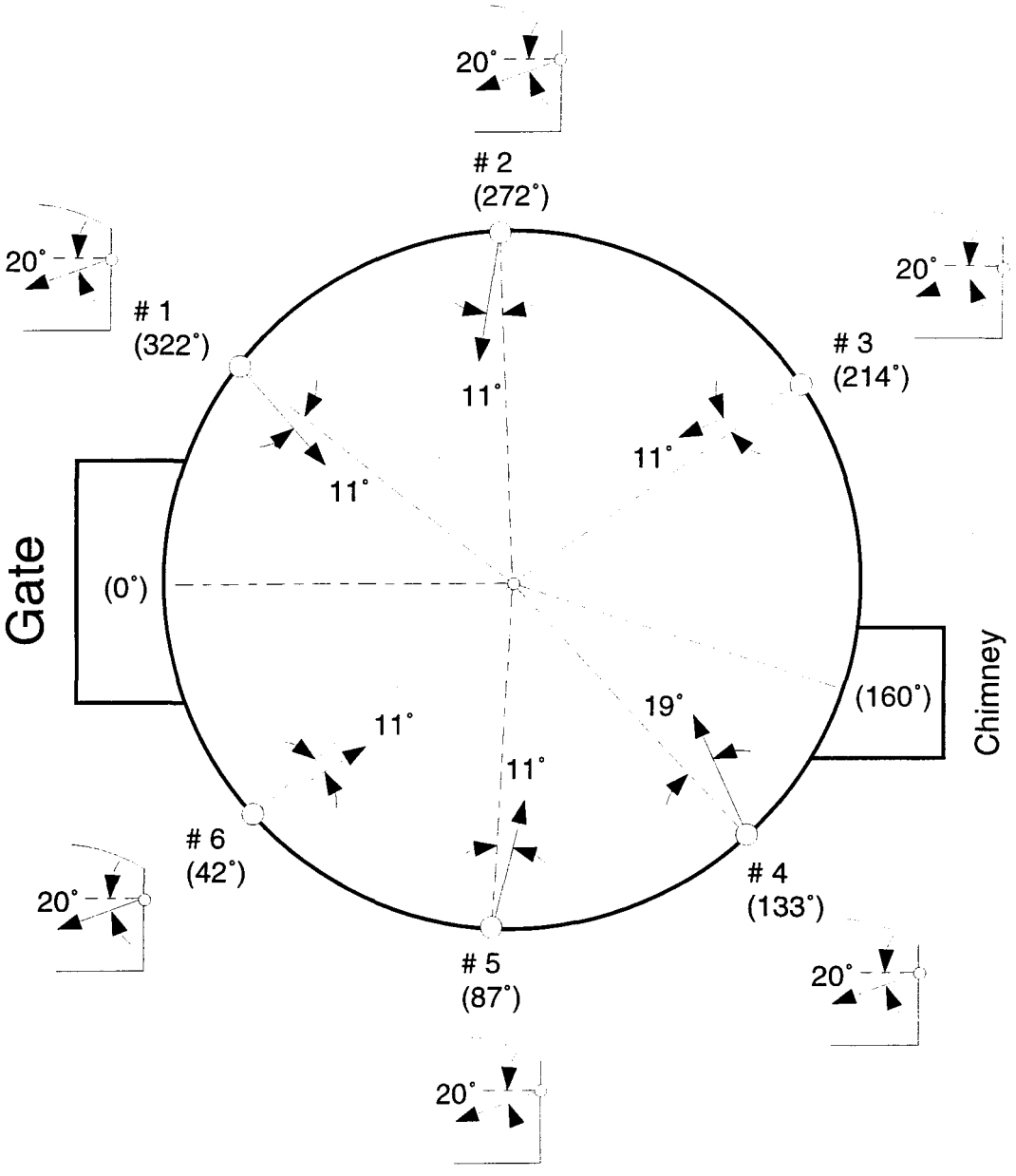

Figure 3.7 Burner orientation and their relative angular positions

Chapter 4

PRE-MEASUREMENT PREPARATION

4.1 CALIBRATION OF HEAT FLUX SENSORS

Heat flux sensors provide a simple, sensitive, and reliable method of measuring heat fluxes, but in the past they have given such poor results that many researchers have stopped using them. These problems were caused by a lack of understanding of the way a sensor interacts with its surroundings [6], by poor meter design, and by inaccurate sensor calibration techniques.

There are currently two calibration techniques in use, the guarded hot plate method and the radiation enclosure method. They are described in detail in Ref. [39]. The guarded hot plate method has the advantage of being capable of calibrating sensors at the flux level and the temperature they will experience in the field.

Many different types of heat flux sensors are available commercially. The type used in this study consists of a thin wafer with serially connected thermocouples (thermopile) attached across its surface. This assembly is enveloped within a protective covering. It is flat, moisture proof, moderately rugged with varying degrees of rigidity, and reasonably uniform in construction. More detailed information on heat flux sensors is available in Ref. [41].

The Rdf corporation has given us a graph that calibrates the output of the heat flux sensor over the temperature range of −300°C to 400°C at a base temperature of 21°C. Because the temperature variation over the surface of the heated skin was expected to be in the range of 30°C to 60°C, it was decided to develop our own calibration curve for this particular range to achieve a higher degree of accuracy.

A procedure was developed by the GRIPS to calibrate each heat flux sensor (HFS) individually over a temperature range of 30°C to 60°C, using the "guarded hot plate" method. A three-dimensional sketch of the device is shown in Figure 4.1.

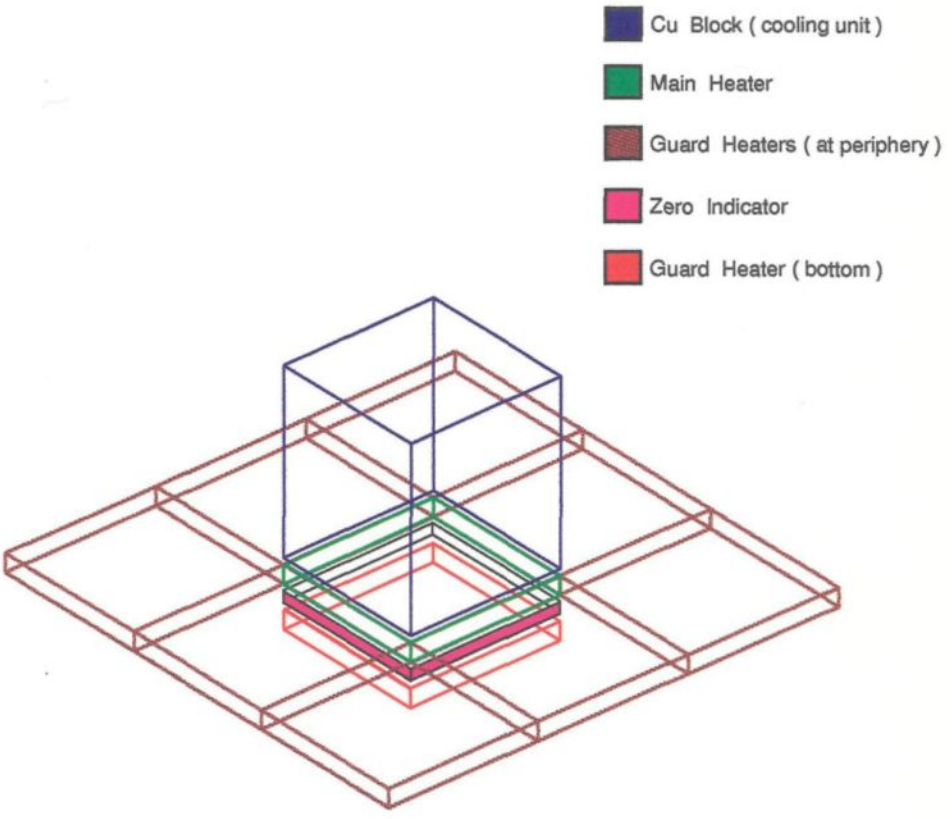

Figure 4.1 3-D line diagram of the HFS calibrator

As shown in the diagram, the main heater is accompanied by 8 lateral guard heaters and one bottom guard heater. All 8 guard heaters and the main heater were individually

equipped with a copper-constantan thermocouple.

Electrical current is dissipated in the lateral guards independently of the main central element; these lateral guards are maintained at a temperature as close as possible to the temperature of the central plate. The guards are essential for the correct functioning of the method: its role consists in maintaining the heat flow lines perpendicular in the central measuring zone. Therefore the density of heat flow is maintained constant and perpendicular to the hot surface and the isothermal planes are parallel in the whole thickness of the sensor (HFS). In other words, the purpose of the lateral guards is to reduce the lateral losses in the central plate as well as in the corresponding central zone inside the specimen, and that of the bottom guard is controlled using the signal from the zero indicator to compensate the downward heat losses from the central plate.

4.1.1 Apparatus Description

4.1.1.1 Heating unit

The heating unit consists of a central metering section and a guard section. The metering section consists of a heater (thin foil heaters from MINCO Inc.) and a plate. The guard section consists of 1 bottom and 8 lateral guard heaters attached to the flat plates. The surface plates are made of metal (copper) of high thermal conductivity, and the surfaces are smoothly finished to conform to a true plane.

4.1.1.2 Cooling unit

The cooling unit, a solid copper block, has the same bottom dimensions as the central plate and its height corresponds the side of the plate (see Figures 4.1 and 4.2).

4.1.1.3 Edge heat losses

As explained earlier, the deviation from one-dimensional heat flow in the main plate as well as in the corresponding central zone in the specimen, through the edges, was reduced by 8 additional lateral guard heaters installed at the periphery and corners of the central plate.

4.1.1.4 Zero indicator

To detect the heat flow from the main heater to the bottom guard heater or vice versa, a zero indicator (heat flow meter) was installed between the lower surface plate of the main heater and the upper surface plate of the bottom guard heater.

4.1.1.5 Contact resistance

The imperfect contact between the central surface of the main heater plate and of the specimen (HFS) was improved by inserting a thin homogenizing layer of material having thermal resistance much lower than the air resistance.

4.1.1.6 Enclosure

The main apparatus was placed in an enclosure to avoid non-uniform cooling of the apparatus by forced convection due to surrounding air movement.

For better understanding a two-dimensional sketch is given in Figure 4.2.

The "guarded hot plate" imposes adiabatic boundary conditions on the "hot side" in order to ensure constant heat flux density and uniform temperature.

The electrical circuit diagram of the thermocouples, the guard heaters and the main heater can be seen in the Figure 4.3.

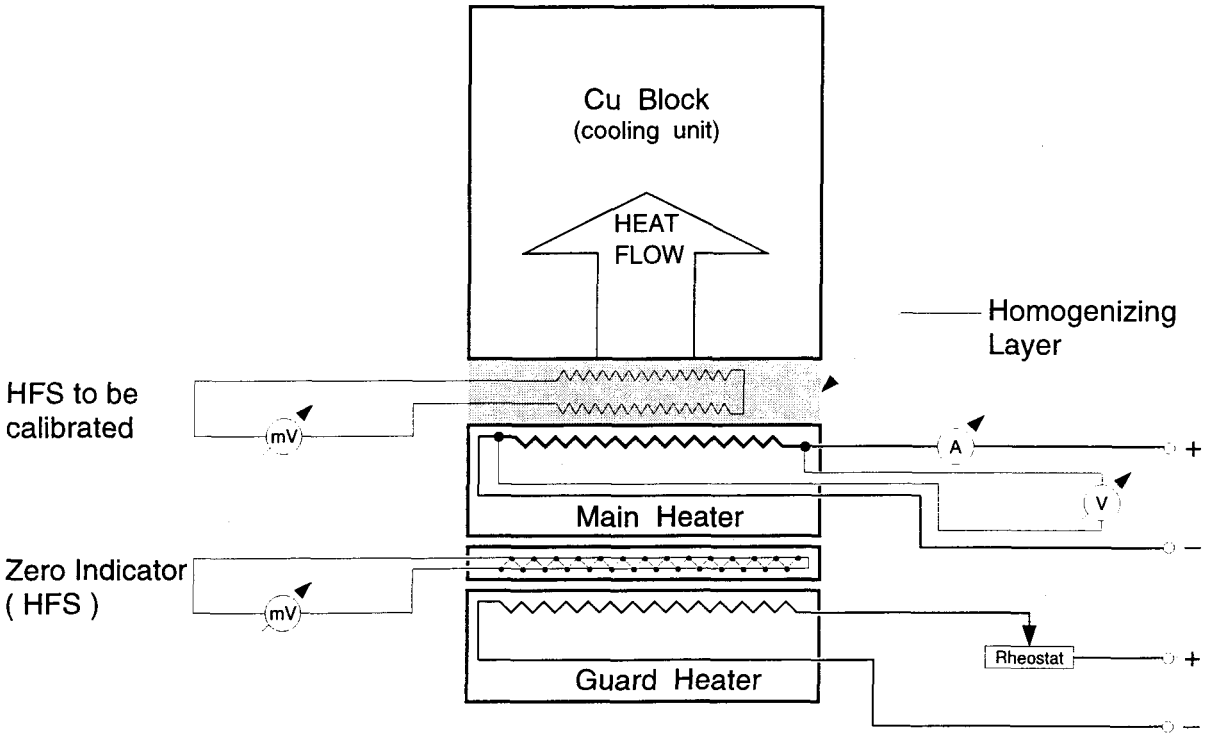

Figure 4.2 Schematic view of the HFS calibrator

The non calibrated HFS was placed between the main heater plate and the cooling unit (Cu block). The main heater temperature was set to the lowest temperature in the calibration range ($\approx$ 30°C). All 8 lateral guard heaters were set to the same temperature as the main heater. The downward heat dissipation from the main heater was compensated by the bottom guard heater. A heat flow meter was installed between the main heater and the bottom guard heater to confirm zero heat flow. The steps were repeated at 10°C increments in the main heater temperature from 30°C to 60°C.

The computation of the heat flux density was made from the electrical power dissipated and measured in the central part of the hot plate (main heater).

$$q = \frac{W}{A} \tag{24}$$

Where A is the area (m^2) of the central zone and W is the electrical power (W) dissipated in the main heater. This electrical power supplied to the main heater was calculated from measurements of voltage and current. Voltage and current measurements were taken using a digital multimeter (FLUKE 79, series II multimeter). In the 10 Amp. range, the unit has a resolution of 1 mA and accuracy 2% of reading three digits. The voltage measurement (four wire arrangement) in the 4 V range, has a resolution of 0.5 mV and accuracy $\pm 0.5\%$ of one digit.

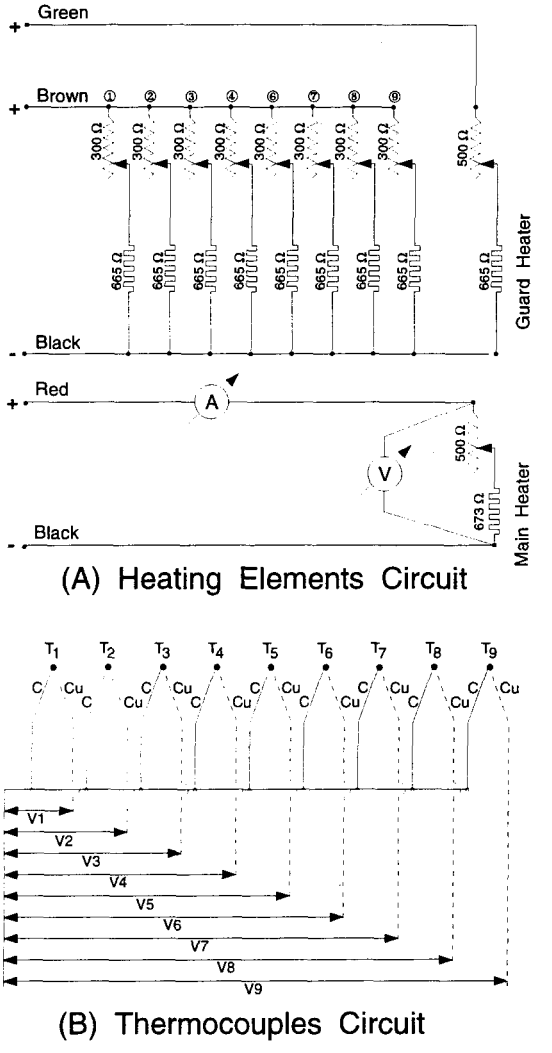

Figure 4.3 Circuitry of the HFS calibration device

4.2 INFRARED THERMOGRAPHIC MEASUREMENTS

To have an overall thermal view of heated skin surface for various experimental conditions, measurements were taken using an infrared Thermo-Tracer (6T62, manufactured by MIKRON Instruments Co., Inc.).

The amount of infrared energy radiated from the surface of any object can be described by a relationship between the surface temperature and the emissivity of the object. The Thermo-Tracer collects this infrared energy as a non contact measurement system and converts it into an electrical signal by a high sensitivity infrared detector (HgCdTe, liquid nitrogen cooled type). By optically scanning the infrared energy emitted from objects both horizontally and vertically, the system displays the temperatures of the surface of the object as two-dimensional color or monochrome temperature images [35].

The block diagram of 6T62 Thermo-Tracer can be seen in Figure 4.4.

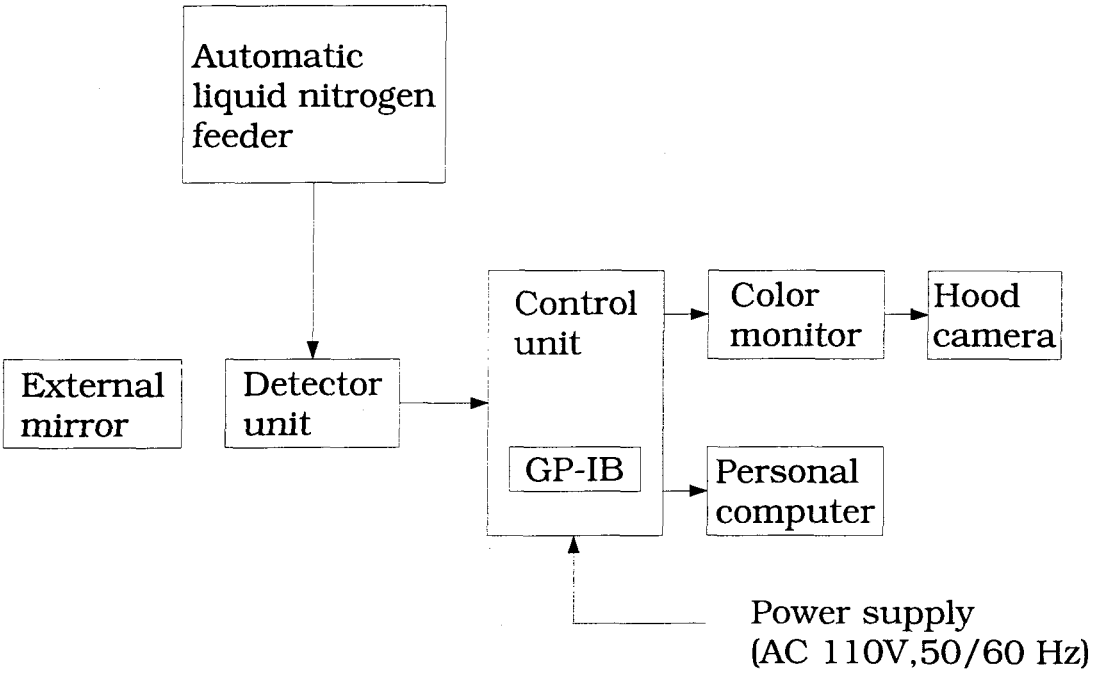

Figure 4.4 Block diagram of the Thermo-Tracer

4.2.1 Operating Principle

Infrared rays are electromagnetic waves of about 0.76 μm to 1000 μm in wavelength and are a generic name for a spectrum of waves from the short wavelength end of visible rays to long wavelength end of microwave. Infrared rays are closely related to the temperature of physical bodies. All objects above the absolute zero (-273°C) continuously radiate infrared energy. According to Planck's law, the radiation power (monochrome radiant emissive power) of a black body is given by the following formula and can be represented in a graph as shown in Figure 4.5.

$$E_{b\lambda} = \frac{C_1}{\lambda^5}\left(e^{\frac{C_2}{\lambda T}} - 1\right)^{-1} [W/cm^2.\mu m] \tag{25}$$

where

λ: wavelength, μm

T: absolute temperature of blackbody, K

C_1: first radiation constant, 3.7402×10^{-12} W.cm^2

C_2: second radiation constant, 1.4388 cm.K

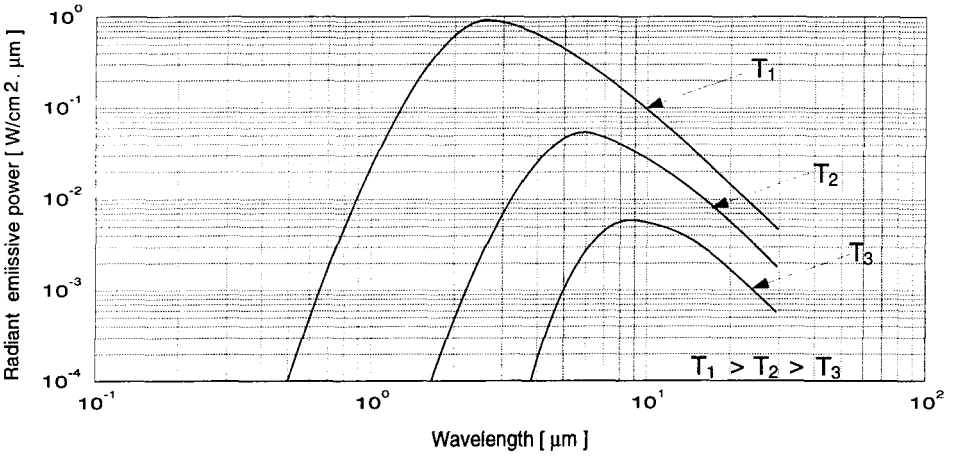

Figure 4.5 Monochrome radiant emissive power versus wavelength of a blackbody

The blackbody refers to a body that will completely absorb incident infrared rays. In other words, it means an object that will radiate more energy than any other object at a certain temperature.

Emissivity is defined as the efficiency of radiation compared with the blackbody. Thus emissivity of the blackbody is 1 and the emissivity of grey bodies is smaller than 1. Consequently, emissivities of these grey bodies must be compensated for, depending on objects to be measured. Compensation for emissive power by emissivity refers to this function.

When monochrome radiant emissive power formula is integrated over all wavelengths, total radiant emissive power can be obtained and this value is found to be proportional to the fourth power of absolute temperature as shown in the following formula. This is called Stefan-Boltzmann law.

$$E_b = \int_{\lambda=0}^{\lambda=\infty} E_{b\lambda} d\lambda \quad = \quad \sigma T^4 \quad [W/cm^2] \tag{26}$$

where σ: Stefan-Boltzmann constant (5.673×10^{-12} W/cm^2.K^4)

If a detector that can detect all wavelengths is available, an output proportional to the fourth power of absolute temperature can be obtained. However, it is impossible to detect all wavelengths with actual measuring instruments, because both their optical system and detector have wavelength characteristics of their own. In actual practice, infrared radiation is used by limiting a certain wavelength region to a range of 8μ to 13μ by an optical filter. The detected output is generally not an output proportional to the temperature. Therefore, this output is converted to one proportional to the temperature through a linearizing circuit (linearizer). The detailed block diagram can be seen in Figure 4.6.

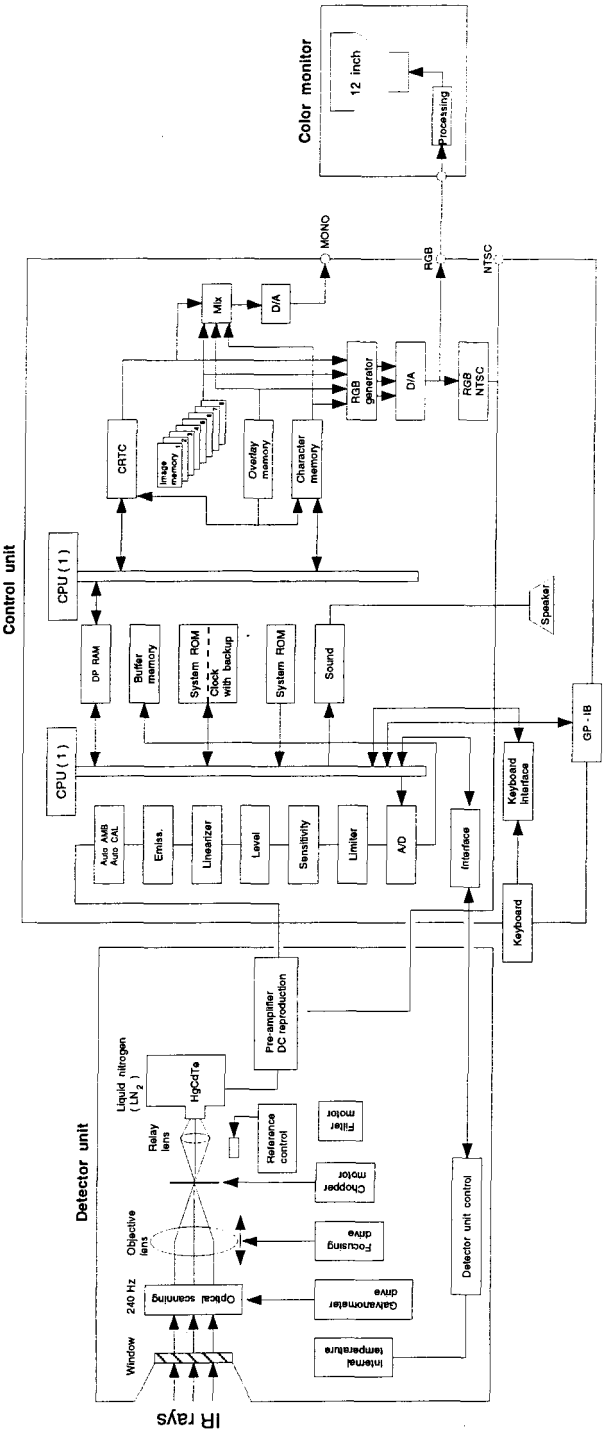

Figure 4.6 Detailed block diagram of 6T62 Thermo-Tracer

4.2.2 IR Window Material

The furnace model is made of plexiglass and this material is opaque to infrared rays, so it was decided to cut a window and replace it by a different material of high transmittance. Many different materials were found as possible candidates for making this IR window; they include organic and inorganic solids [47]. The most economical approach: a thin film of polyethylene, was selected for this purpose. The relationship between transmittance and wavelength for various materials including polyethylene can be seen in Figures 4.7 to 4.13.

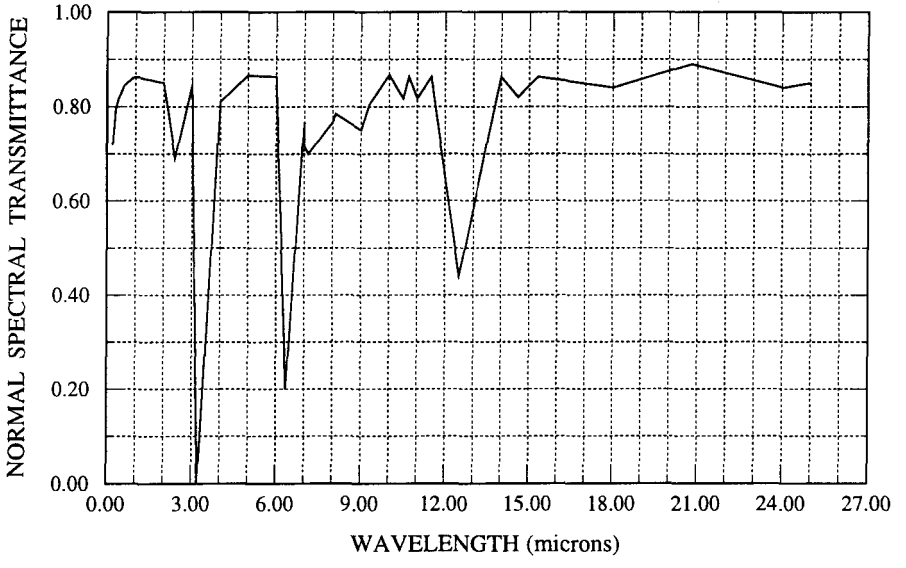

Figure 4.7 Transmittance of "Polyethylene", at 300 K, as a function of wavelength, 508 μm thick.

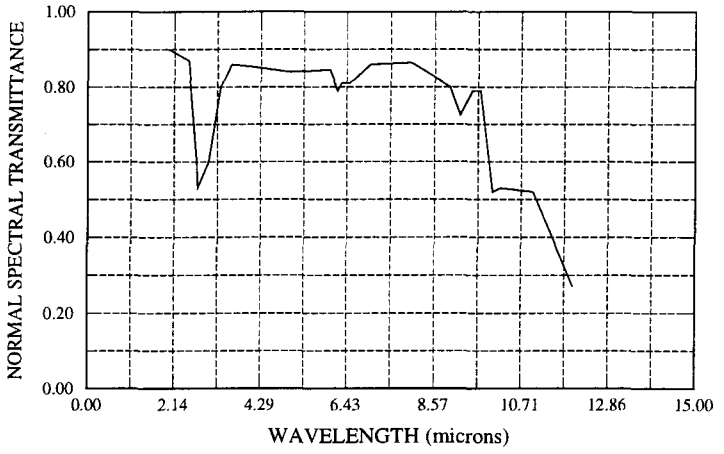

Figure 4.8 Transmittance of "Arsensulfide glass", at 300 K, as a function of wavelength, 3 mm thick.

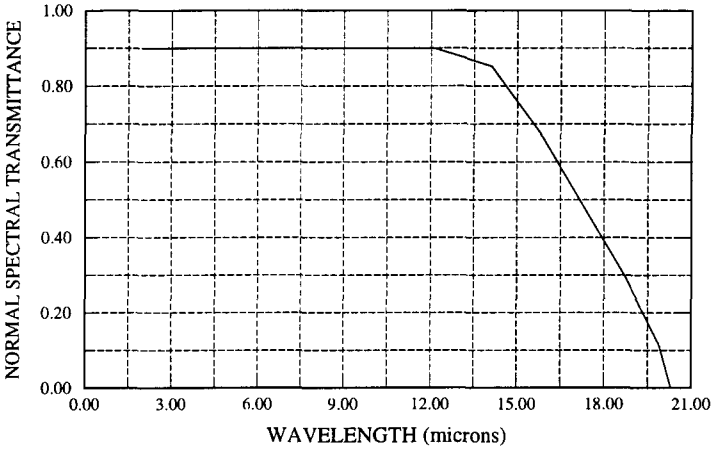

Figure 4.9 Transmittance of "Sodium Chloride (NaCl)", at 298 K, as a function of wavelength, 5 mm thick.

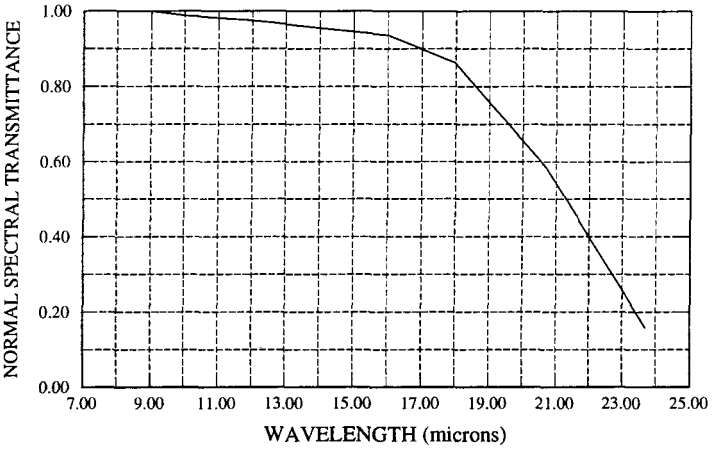

Figure 4.10 Transmittance of "Potassium Chloride (KCl)", at 300 K, as a function of wavelength, 10 mm thick.

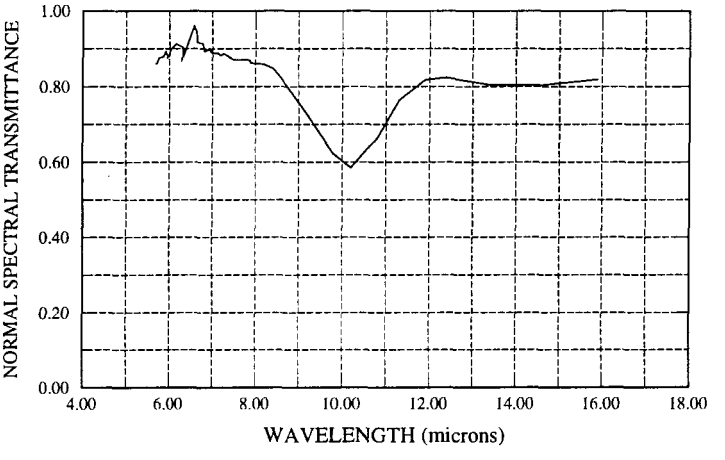

Figure 4.11 Transmittance of "Silicon monoxide (SiO)", at 298 K, as a function of wavelength, 137 mm thick.

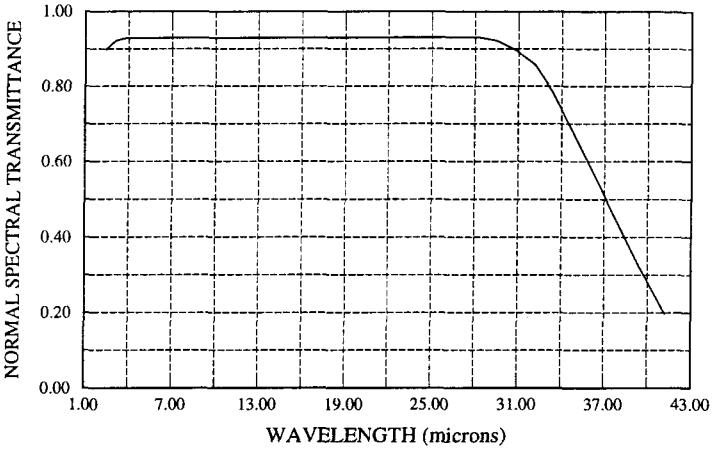

Figure 4.12 Transmittance of "Rubidium Bromide (RbBr)", at 313 K, as function of wavelength, 5.3 mm thick.

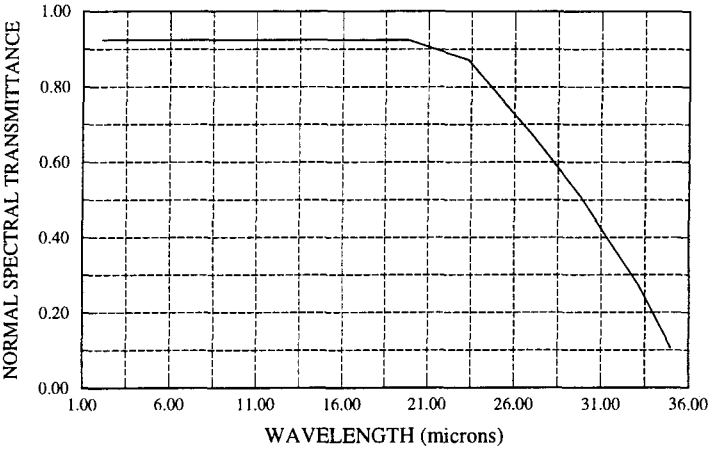

Figure 4.13 Transmittance of "Potassium Bromide (KBr)", at 298 K, as a function of wavelength, 5 mm thick.

4.3 EFFECT OF ADDITIONAL THERMAL RESISTANCE

Infrared thermographic measurements were performed to determine the temperature distribution over the molten metal flat bath in the circular furnace. In order to detect infrared rays, the emissivity of the surface should be at least in the order of 10%. To meet this requirement, a part of the heated skin was painted black as shown in Figures 3.1 and 5.12. This black paint coating permitted us to visualize the distribution of temperature, as well as the detection of hot spot formation [31].

While performing the first series of tests, it was found that the heat flux sensors measured higher heat flux values than what was provided as an input to the heating elements, because the color of the HFS was darker (brown) than that of the test surface (shiny) and the HFS was extracting the heat from the test surface due to radiation. Aluminum foil was applied on top of the sensors of the key hole section to force the surface reflectivity to be identical to that of the heating element surface, thus eliminating radiation from the sensors themselves (see Figure 4.14).

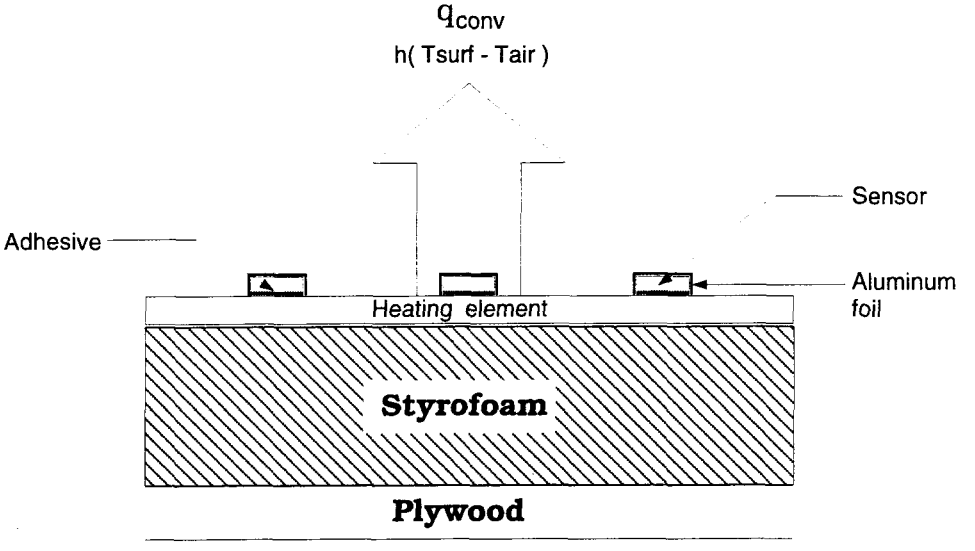

Figure 4.14 Effect of additional thermal resistance due to adhesive, sensor and aluminum foil

Applying the aluminum foil, sensor itself and the adhesive used to fix sensor on the heated skin cause thermal dissimilarity due to their additional thermal resistances. This thermal dissimilarity can be calculated in the following manner (see Figure 4.15).

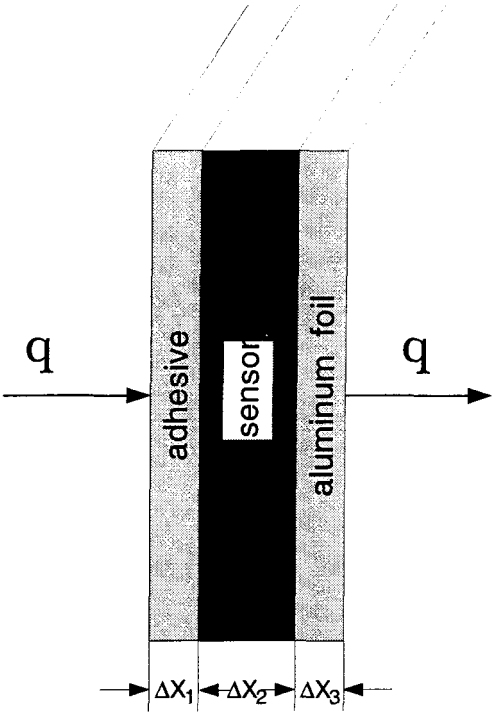

Figure 4.15 Heat transfer through additional resistances

An electrical analog can be seen in Figure 4.16

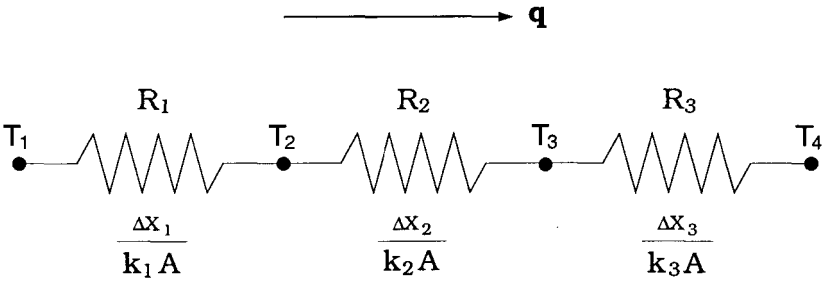

Figure 4.16 Electrical analog of heat transfer through additional resistances

where:

R_1 = Resistance due to the adhesive,

R_2 = Resistance due to the sensor, and

R_3 = Resistance due to the aluminum foil.

Now by Fourier's law

$$q = \frac{\Delta T_{overall}}{\sum R_{th}} = \frac{\Delta T_{overall}}{\sum \frac{\Delta X_i}{k_i A}} \tag{27}$$

$$\Delta T_{overall} = \dot{q} \left(\frac{\Delta X_1}{k_1} + \frac{\Delta X_2}{k_2} + \frac{\Delta X_3}{k_3} \right) \tag{28}$$

where:

k is the thermal conductivity of the material,

ΔX is the thickness of the material,

q is the heat flow rate, and

$\dot{q}$ is the heat flux density.

k_1 = 0.415 $\frac{W}{m.K}$

k_3 = 230.0 $\frac{W}{m.K}$

ΔX_1 = 0.02 mm

ΔX_3 = 0.12 mm

R_2 = 0.004 $\frac{K}{W/m^2}$

Note: The data for the thermal conductivity of the adhesive and aluminum were obtained from Ref. [32]. For the sensor material, the thermal resistance was provided by Rdf Corporation [41].

For $\dot{q}$ = 100 W/m^2

$$\Delta T_{overall} = 100\left(\frac{0.02\times10^{-3}}{0.415} + \frac{0.12\times10^{-3}}{230} + 0.004\right) = 0.4 \text{ K}$$

For $\dot{q}$ = 600 W/m^2

$$\Delta T_{overall} = 600\left(\frac{0.02\times10^{-3}}{0.415} + \frac{0.12\times10^{-3}}{230} + 0.004\right) = 2.4 \text{ K}$$

The above analysis shows that the temperature difference between the sensor surface and the heating element surface seen by infrared camera would vary from 0.4 K to 2.4 K depending upon the flux level.

Chapter 5

EXPERIMENTS, RESULTS AND DISCUSSION

5.1 PROBLEM STATEMENT

In this chapter, the steady state, forced convection heat transfer in a circular remelting furnace having complex mean flow, will be considered. This investigation examined the magnitude and uniformity of the convective heat transfer coefficients along the flat molten bath, which was simulated by heated skin, in a circular top-charged remelting furnace.

The main steps of this experiment were:

1. To use the heated skin technique to obtain local heat transfer data along the flat molten bath of a top-charged circular furnace.
2. To calculate the local convective heat transfer coefficients and arrange them in non-dimensional form.
3. To use the infrared Thermo-Tracer to obtain uniformity of the heat distribution along the flat molten bath, i.e. detection of hot spots.
4. Use of the hot-film anemometer to obtain the radial velocity distribution in the boundary layer near the flat circular bath as well as at the burner's level.
5. To analyze and compare the experimental heat transfer results with the velocity distribution results and those provided by the flow visualization experiments.

5.2 EXPERIMENTAL MEASUREMENTS

This section is divided into three main sub-sections, (i) Measurement of the heat transfer coefficient, (ii) Measurement of velocity, and (iii) Detection of hot spots using IR camera.

5.2.1 Measurement of Heat Transfer Coefficients

5.2.1.1 Heated skin module

As described earlier in section 3.1, a flat circular disk of 1.12 m in diameter and 13 mm thick, was fabricated from styrofoam. The back of this styrofoam disk was supported by a 13 mm thick plywood sheet. Nine holes of approximately 2 mm diameter were drilled in the styrofoam-plywood disk for the insertion of the wires from the heating elements, thermocouples, and heat flux sensors. The micro-foil heaters in seventeen pieces were glued to the styrofoam disk. Then, foil thermocouples and heat flux sensors were attached on the heated skin surface (see Figure C.2).

This flat instrumented disk was placed in the scaled physical model. The thermocouples and heat flux sensors were connected to the data acquisition system as shown in Figure 3.4 and the heaters were connected to the power supply through a control panel (see Figure 3.3).

5.2.1.2 Test procedure

Twenty five experimental runs were performed with combinations of five different Reynolds numbers and five different sets of burner orientations.

The *Re* number for all the five sets of different burner orientations were 5.9×10^3, 1.18×10^4, 1.67×10^4, 2.36×10^4 and 3.12×10^4. The five burner orientations consists one set given by the industrial partner (often mentioned as "original position", the burners angular position and their orientation can be seen clearly in Figure 3.7), and in the four

other burner orientations, the downward angle was fixed to 10° and the horizontal angle with reference to the radial direction in the horizontal plane was varied in the steps of five degrees beginning from 0° to 15°.

Repeatability runs were performed for the set in which all the burners are pointing axially towards the centre and making 10° downward in the vertical plane.

A data acquisition program was used to gather experimental data as described in the earlier chapter 3. For each run, the data acquisition program was left to monitor the heated skin temperatures for at least three hours after the power supply to the heaters had been turned on. This was done to ensure that steady state was achieved.

5.2.1.3 Heat transfer analysis and non-dimensionalization

Determination of the convective heat transfer at the interface between the test surface (circular molten metal flat bath, simulated by heated skin) and the fluid (air) requires the consideration of two other modes of heat transfer. They are, (i) heat conduction inside the test object that the heated skin is attached to, and (ii) radiation heat transfer from the surface of the heated skin to its surroundings.

As the temperature distribution along all boundaries of a closed region encompassing the test object and the thermal conductivities of all materials inside this region are known, the heat conduction inside the test object may be computed by using Fourier's law. Special attention was paid to minimize heat losses due to conduction while designing the test object, as discussed in section 3.1.

Radiation heat transfer calculations require the knowledge of the temperature and radiation properties of the heated skin surface and all other materials which the heater views. In order to simplify these radiation calculations and enhance the accuracy of the

results, shiny and black painted aluminium surfaces with emissivities below 1% and above 95% respectively were used.

In mathematical terms, an energy balance applied on the surface of the heated skin can be expressed as follows:

$$\dot{q}_{conv} = \dot{q}_{input} - \dot{q}_{rad} - \dot{q}_{cond} \tag{29}$$

where $\dot{q}_{conv}$ is the convection heat flux leaving the surface of the test object (heated skin surface), $\dot{q}_{input}$ is the heat flux generated inside the electrical resistances due to power supplied to the heaters, $\dot{q}_{cond}$ is the heat flux leaving the heater by conduction inside the test object, and $\dot{q}_{rad}$ is the heat flux leaving the heated skin surface due to radiation.

If the conduction heat loss through the test object is considered to be negligible, then the local convection heat flux may be given by:

$$\dot{q}_{conv} = \dot{q}_{input} - \sigma\epsilon\left(T_{surf}^4 - T_{air}^4\right) \tag{30}$$

In order to quantify the convection heat transfer process, a convection heat transfer coefficient is defined which relates the surface heat flux to a temperature potential difference. The local convective heat transfer coefficient becomes:

$$h_{conv}^{local} = \frac{\dot{q}_{conv}}{T_{surf} - T_{air}} \tag{31}$$

and the average convective heat transfer coefficient can be defined as:

$$h_{avg} = \frac{1}{A}\int_0^A h_{local}.dA \tag{32}$$

where $\dot{q}_{conv}$ is the heat flux leaving the test surface due to convection, A is the total test surface area, T_{surf} is the test surface temperature and T_{air} is the air temperature at the inlet.

A significant thermal boundary layer exists by virtue of the temperature gradient between the test surface temperature and the fluid (air) temperature. Here the analysis used to determine convective heat transfer coefficient is performed at the steady state condition,i.e. when the applied heat flux is balanced by the downward heat conduction transfer through the styrofoam-plywood plate (test object) and upward convection and radiation transfer from the test surface to its surroundings.

The convective heat transfer coefficient is usually presented in non-dimensional form as a Nusselt number, which involves fluid conductivity and a characteristic dimension. The use of the Nusselt number as a mean of expressing the convective heat transfer coefficient non-dimensionally seems to have been adopted quite early. In their 1932 text, Fishenden and Saunders [13] as cited in Ref. [9], discuss non-dimensional groupings in connection with convective exchange.

The Nusselt number is then defined as:

$$Nu = \frac{h_{conv}.L}{k_{air}} \tag{33}$$

The Nusselt number provides a very simple way of non-dimensionalizing the convective heat transfer coefficient. However, it includes a characteristic length which may not be physically relevant to the convection process, and it omits factors which are relevant. We may note the effect of the various parameters on the behavior of the convective heat transfer coefficient:

1. **Conductivity :** A finite value of k is necessary, so that there can be transfer of heat from the surface to the fluid.
2. **Density :** A finite value of ρ is necessary so that heat can be absorbed by the fluid.

3. **Specific Heat :** A finite value of C is also necessary so that heat can be absorbed by the fluid.
4. **Velocity :** A finite value of V is necessary to establish a steady state heat transfer.
5. **Characteristic Length :** The role of length L is less clear-cut. It is physically important, for example, in discussing natural convection heat transfer under laminar flow conditions, but not for turbulent flow conditions.
6. **Viscosity :** The viscosity of a fluid in no way assists convective heat transfer. Its only action is to tend to restrain the flow of the fluid.

Another important dimensionless group in the forced convection flow is the Reynolds number, which relates the intensity of the momentum transfer by convection to that by molecular mechanism (viscosity). This is defined as follows:

$$Re = \frac{V.\rho.L}{\mu} \tag{34}$$

The value of the Reynolds number strongly depends on how one selects the value of the characteristic velocity V and the characteristic length L. In case of the circular remelting furnace, the peak or average velocity at the mouth of the burner, the average velocity in the stack, or many other values can be equally recommended. Unfortunately, the complex and qualitatively different flow patterns in the axially and tangentially fired furnaces together with the highly undefined cross-sections of the main streams do not offer a plausible definition for the characteristic velocity. Therefore, there is no straightforward definition of the Reynolds number that would allow a comparison between furnace with axially symmetric firing pattern and another with rotating flow.

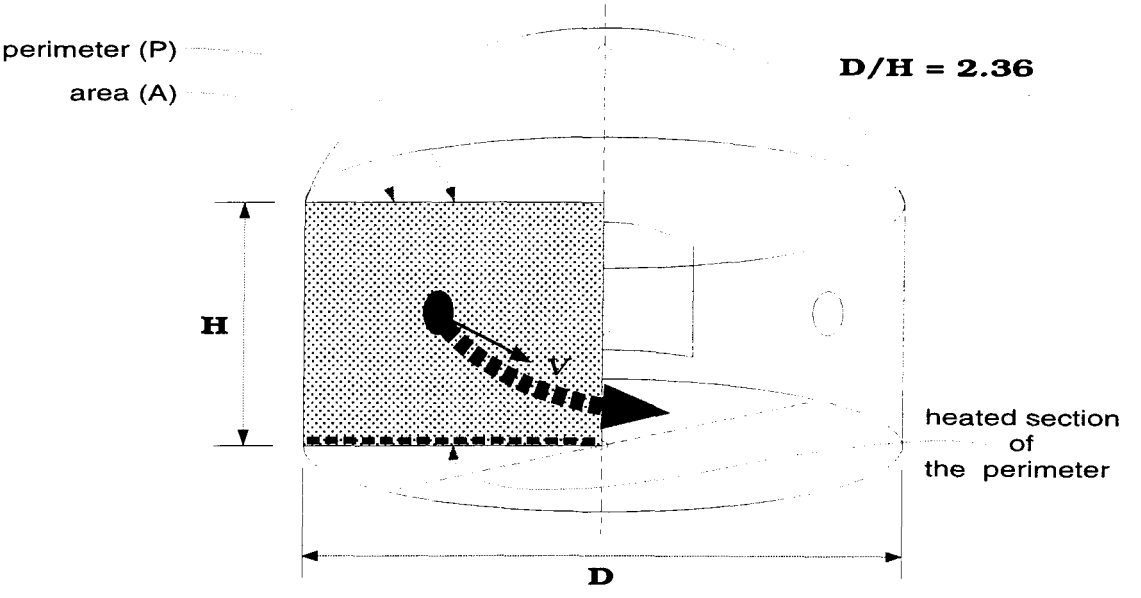

Figure 5.1 Definition of characteristic length and characteristic velocity

In our analysis, the following definition of the characteristic velocity was selected: the total volumetric flow rate from all the burners is divided by half the area of an internal vertical section of the circular furnace (see shaded area in Figure 5.1). This definition results in a hypothetical velocity, which can be interpreted as an average horizontal velocity value in the vertical central cross-section of both types of furnaces (rotational and axial flow pattern).

$$V = \frac{n.m}{\rho.A} = 2.\frac{n.m}{\rho.D.H} \tag{35}$$

where n is the number of burners, m is the mass flow rate of the gas from one burner and ρ is the average density of the gas in the furnace chamber.

As the characteristic length, several quantities like the internal diameter, the hydraulic and thermal equivalent diameters were taken into account. The thermal equivalent diameter can be expressed in terms of the diameter D or height H for a fixed aspect ratio (in the

present study D/H = 2.36) :

$$D_{thermal} = \frac{4.A}{P_{heated}} = \frac{4.H.\frac{D}{2}}{\frac{D}{2}} = 4H = 1.7D \tag{36}$$

and the hydraulic diameter is:

$$D_{hydraulic} = \frac{4.A}{P_{total}} = \frac{4.H.\frac{D}{2}}{H + 2.\frac{D}{2}} = 1.4H = 0.6D \tag{37}$$

In order to simplify the calculations, we have chosen, the following expression for calculating the Reynolds number:

$$Re = \frac{\dot{m}.L}{A.\mu} = \frac{\dot{V}.\rho.L}{A.\mu} = 1.2\frac{\dot{V}.\rho}{H.\mu} \tag{38}$$

where $\dot{V}$ is the air flow rate (m^3/s), μ is the dynamic viscosity of the air (kg/m.s), and $\dot{m}$ is the mass flow rate of the air (kg/s). The definition of the above Reynolds number corresponds to the use of the 0.6D as the characteristic length, while the characteristic velocity is obtained via equation (35).

However, it must be remembered that in the case of the rotational flow pattern, the horizontal velocity in the toroidal part of the flow, as described in chapter 2, can be significantly higher than the average value as calculated above on the basis of the continuity principle. The fast spinning doughnut is not leaving the furnace, its high velocity stream forms a closed loop inside the furnace. This vortex plays an important role in the intensification of the convective heat transfer along the surface. It is reasonable to assume that the characteristic velocity in the Reynolds number should depend on this rotational component also, not only on the average velocity of the path of the gas through the chamber. This can be done either by using an appropriate proportionality factor instead of 2 in equation (35) or splitting the Reynolds number into two components, one describing the effect of the overall flow rate through the furnace, the other characterizing the rotational velocity of flow.

5.2.2 Measurement of Velocity

The turbulent flow resulting from the six jets exhausting into the furnace chamber was investigated. The overall flow rate of the gas (air) was measured by an orifice meter before entering the distributor drum for the individual nozzles representing the burners. The radial velocity distribution (horizontal as well as vertical components) at the burners level and in the flow boundary layer near the test surface was measured by using hot-film anemometry, for each and every burner settings in combination with various overall Reynolds numbers as defined in section 5.2.1.2.

5.2.3 Detection of Hot Spots using IR Camera

The distribution of the surface temperature and the formation of hot spots were monitored by infrared thermograph for all the twenty five experimental runs.

Infrared is a mean of visualization currently used by the heat transfer researchers. Progress achieved in the technology of infrared scanners permit now the determination of wall temperature distribution with a good precision [3,14].

As explained earlier, the infrared scanning radiometer detects the electromagnetic energy radiated in the IR spectral band from an object whose temperature has to be measured and converts it into an electronic video signal. In particular, starting from the object, IR energy is first radiated through a medium (typically the atmosphere). It then enters the sensing system, passing through a lens, a scanning mechanism, an aperture (or a filter), and finally impinges on an IR detector, which transduces the radiation into an electrical signal [50].

As defined in section 4.2.2, the plexiglas walls of the furnace model are transparent to visible light, but they do not transmit the long wave (typically 8-13 μm) infrared radiation

from the heated skin. After a literature survey as well as a series of practical tests, an infrared window was made using thin, stretchable polyethylene foil. The requirements of the IR studies and those for the quantitative evaluation of the convective heat transfer coefficients are contradictory. To isolate the convective transfer from radiation, shiny metallic surfaces with negligible emissivity are required. A thin aluminium foil laminate on the heated skin meets this condition well by having an emissivity below 1%. On the other hand, IR thermography needs high emissivities, at least above 10%. In order to increase the emissivity, thus creating appropriate conditions for the thermography studies, a part of the heated skin was painted black [27].

5.3 PRESENTATION AND DISCUSSION OF RESULTS

5.3.1 Local Nusselt Number

A brief discussion of the expected character of dependence of the local Nusselt number curve, over the circular flat bath, along the radius and periphery, will be given before average values and final results are presented.

The radial distribution of the local Nusselt number, when all burners are set in the original position, is given in Figure 5.2, where [a] and [b] represent the two different ways of determining the heat flux values: by direct measurement of the heat fluxes using heat flux sensors or by measuring the surface temperatures. As the heat flux sensors were applied only on the measuring "key hole" section, further in our analysis, calculations based on the measurement of the surface temperatures will be used. The heat transfer is most intense under the inner annular zone (inner strip), where the cross-mixing in the stream is strong and is decreasing both towards the periphery and the centre of the furnace. The heat transfer coefficients are lower in the centre than over the periphery by 25-

40%. The ratio of the maximum to minimum values is between 1.8-2.5, depending on the Reynolds number. Higher velocities increase the heat transfer coefficient values everywhere and slightly reduce their variation along the radius, which can be explained by the more intensive mixing. The radial variation of the local velocity (horizontal component) near the test surface is given in Figure 5.3. It is following the tendency of the local heat transfer coefficient distribution and also confirms the qualitative tendencies determined in the cold flow studies. It does not follow exactly the shape of the local Nusselt number distribution curve, because not only the horizontal velocity component, but the vertical component is also participating in the heat transfer exchange. The three other graphs showing the radial distribution of the horizontal and vertical velocity components at different heights are shown in Figure D.1, Appendix D.

Figure 5.4 shows the variation of the local Nusselt number along the radius, when all burners are set uniformly at 15° counterclockwise from the radial direction in the horizontal plane and 10° downward from the horizontal in the vertical plane (H15V10). The heat transfer is most intense over the outer annular zone (outer strip) and decreases towards the centre of the furnace. The ratio of the local Nusselt number close to the walls and at the centre is varying between 1.5-2.1, depending on the Reynolds number. The radial variation of the local velocity (horizontal component) near the test surface is given in Figure 5.5. More graphs, showing the distribution of the horizontal and vertical velocity components at the burners level and close to the test surface, can be seen in Figure D.2, Appendix D.

The distribution of the local Nusselt number along the radius, when all burners are set uniformly at 10° counterclockwise from the radial direction in the horizontal plane and 10° downward from the horizontal in the vertical plane (H10V10), is shown in Figure

5.6. The variation of the local Nusselt number is more or less similar to that of the local Nusselt distribution curve when burners are set in the original position, except that in this case the heat transfer coefficient values are almost identical in the centre and at the walls, while they are higher near the walls than in the centre in the case of the original position. The ratio between the maximum and minimum values varies from 1.5-1.8, depending on the Reynolds number. The radial variation of the local velocity (horizontal component) near the test surface is given in Figure 5.7 and additional graphs are shown in Figure D.3, Appendix D.

The local Nusselt number variation along the radius, when all burners are set uniformly at 5° anti clockwise from the radial direction in the horizontal plane and 10° downward from the horizontal in the vertical plane (H5V10), is given in Figure 5.8. The heat transfer is still intense under the inner annular zone, as it was the case with the original burner setting, except that this time the intensity of heat transfer has shifted more towards the centre. The heat transfer coefficients are higher in the centre than near the walls by 25-30%, while the ratio of the maximum and minimum values is between 1.6-1.9, depending on the Reynolds number. The local velocity distribution (horizontal component) near the test surface, as a function of the relative radial position is given in Figure 5.9 and the graphs showing the horizontal and vertical velocity distributions along the radius at different heights are given in Figure D.4, Appendix D.

The last graph in this series of investigations showing the radial distribution of the local Nusselt number, when all burners are pointing towards the centre and making 10° downward from the horizontal in the vertical plane (H0V10), can be seen in Figure 5.10. The heat transfer is most intense in the centre and is decreasing towards the walls. The

slope of the local Nusselt number distribution curve is reverse compared to that for the case when burners are set in the H15V10 position. In this case the centre is more dominant than the inner annular zone and the overall value of the local Nusselt number is higher than in any other burner settings. The ratio between the Nusselt number in the centre and near the walls is varying from 1.9 to 2.0, depending on the Reynolds number. The variation band of this ratio is the lowest among all the burner orientations studied. It may be due to the higher turbulence and better mixing of the gases inside the furnace chamber. The radial variation of the local velocity (horizontal component) in the boundary layer near the test surface, can be seen in Figure 5.11. The other graphs, showing the horizontal and vertical velocity distribution along the radius, at different heights, are given in Figure D.5, Appendix D.

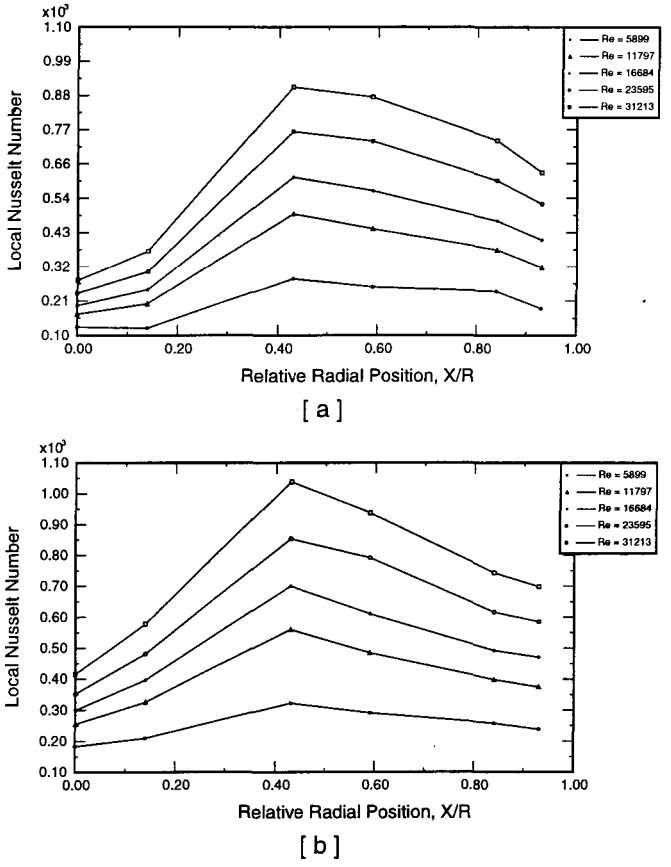

Figure 5.2 Local Nu number over the "key hole" section, along the radius, when burners are in original position, and fluxes were determined by (a) HFS-s, and (b) surface temperature measurement

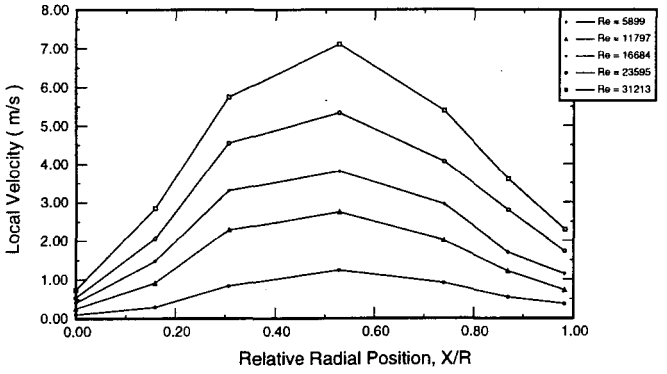

Figure 5.3 Variation of the velocity (horizontal component), near the test surface, along the radius, when burners are in original position

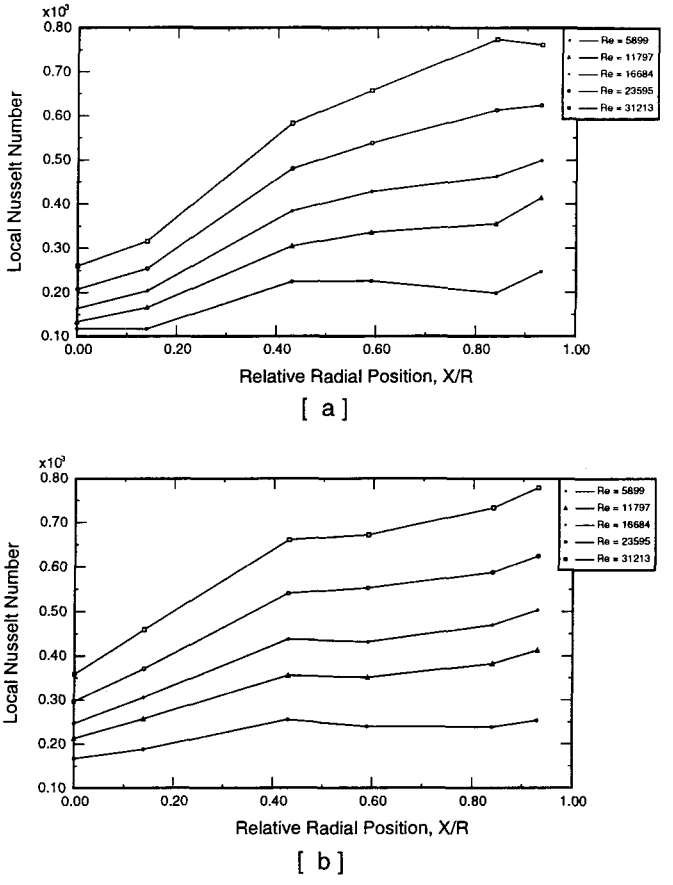

Figure 5.4 Local Nu number over the "key hole" section, along the radius, when burners are in H15V10, and fluxes are determined by (a) HFS-s, and (b) surface temperature measurement

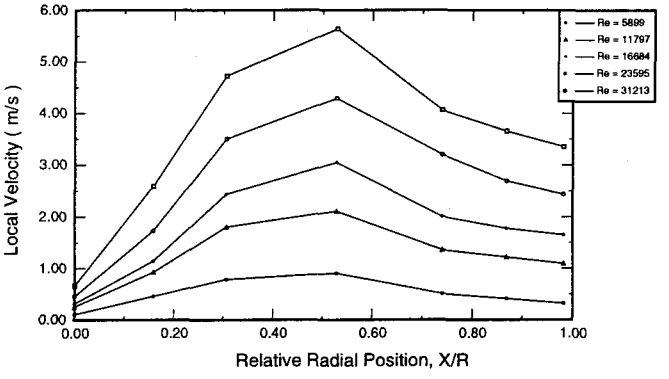

Figure 5.5 Local velocity (horizontal component), near the test surface, as a function of the radius, when burners are in H15V10

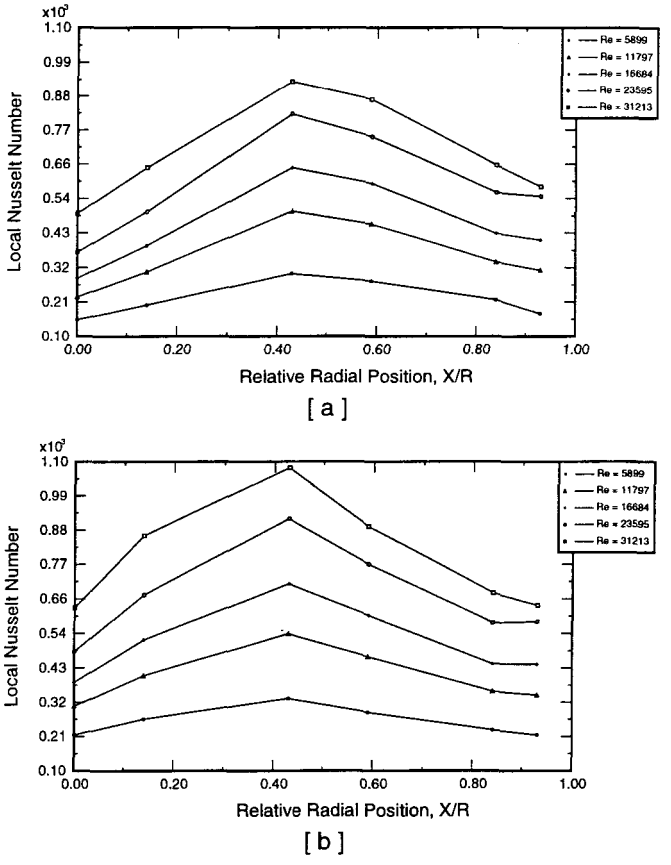

Figure 5.6 Local Nu number over the "key hole" section, along the radius, when burners are in H10V10, and fluxes are determined by (a) HFS-s, and (b) surface temperature measurement

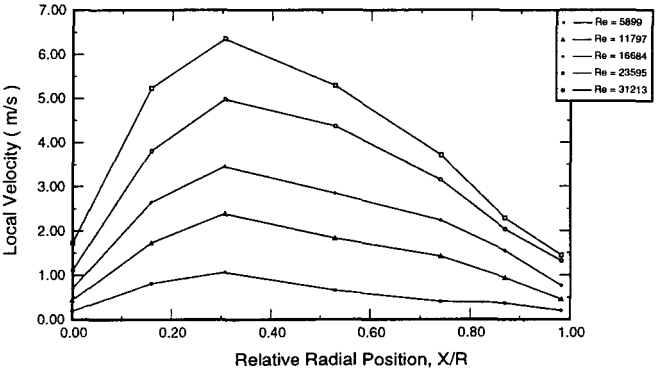

Figure 5.7 Local velocity (horizontal component), near the test surface, along the radius, when burners are in H10V10

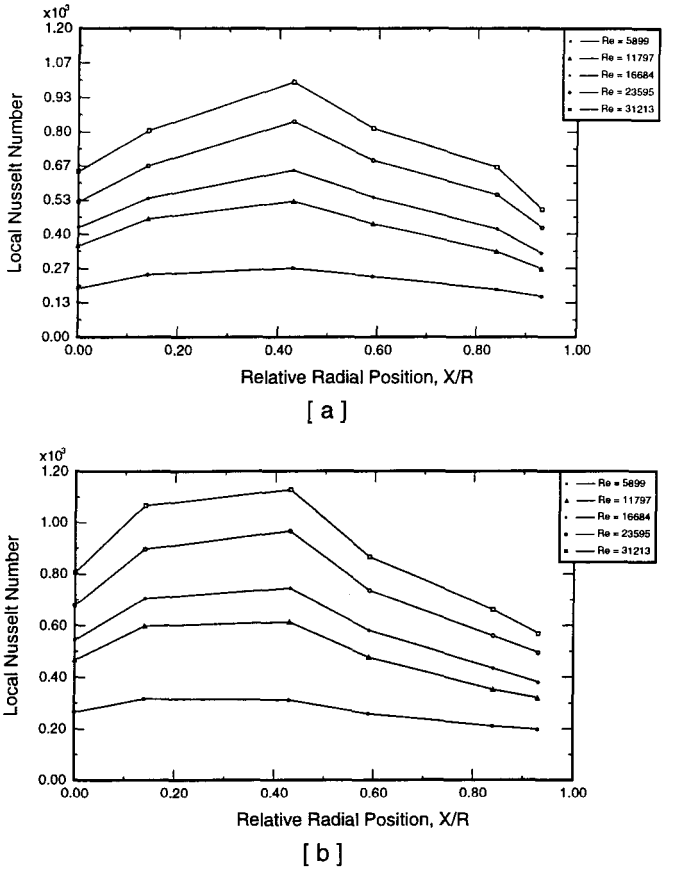

Figure 5.8 Local Nu number over the "key hole" section, along the radius, when burners are in H5V10, and fluxes are determined by (a) HFS-s, and (b) surface temperature measurement

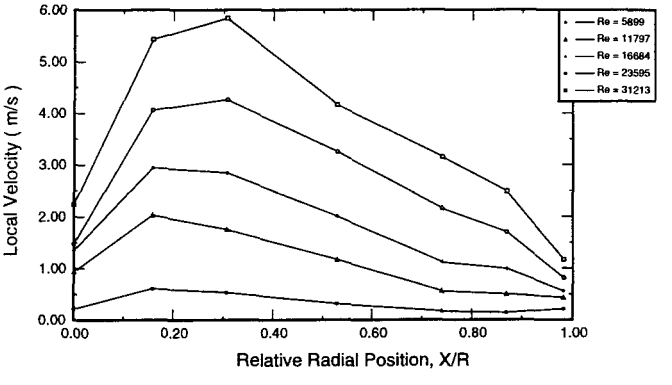

Figure 5.9 Local velocity (horizontal component), near the test surface, along the radius, when burners are in H5V10

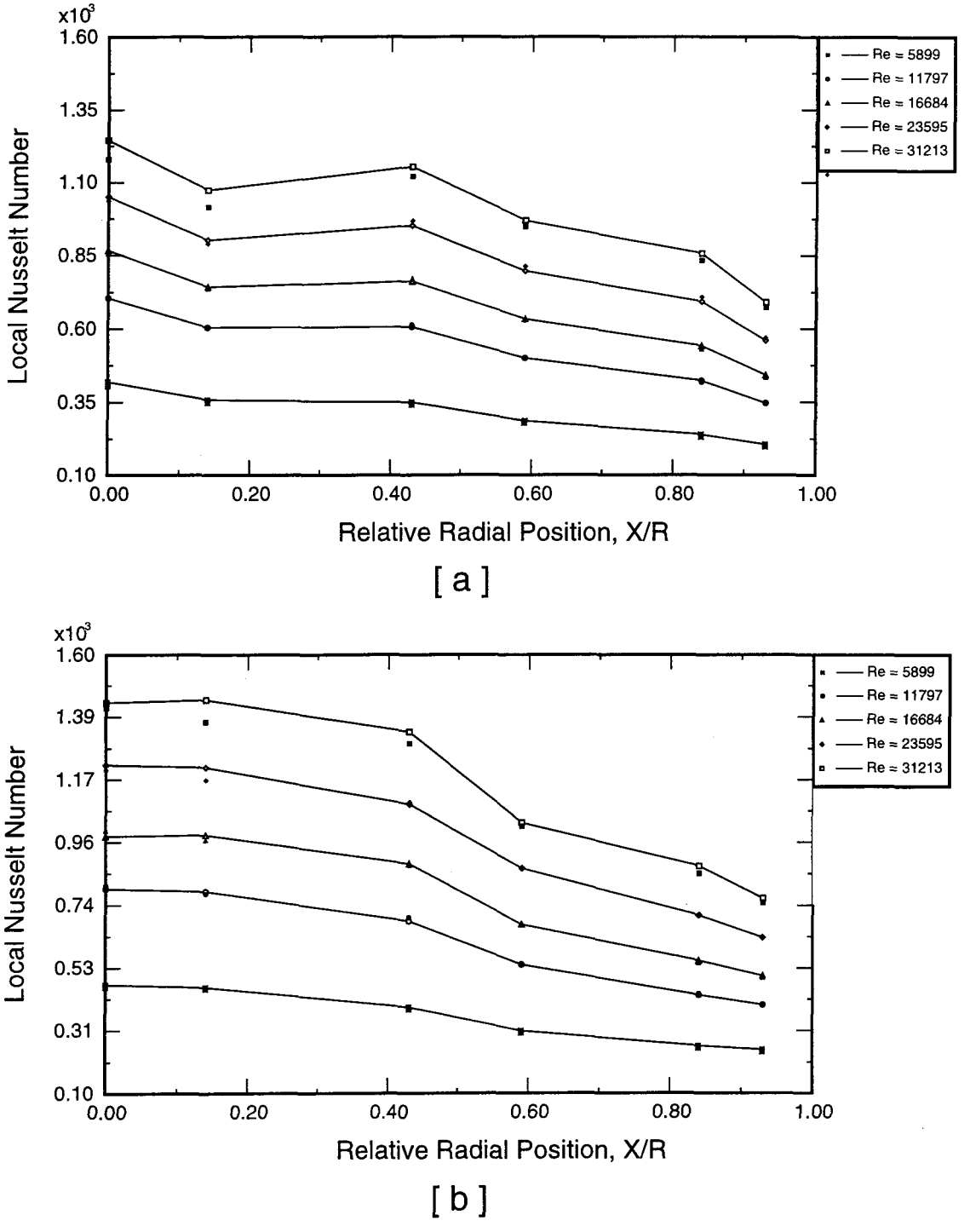

Figure 5.10 Local Nu number over the "key hole" section, along the radius (solid symbols are showing the repeated runs), when burners are in H0V10, and fluxes were determined by (a) HFS-s, and (b) surface temperature measurement

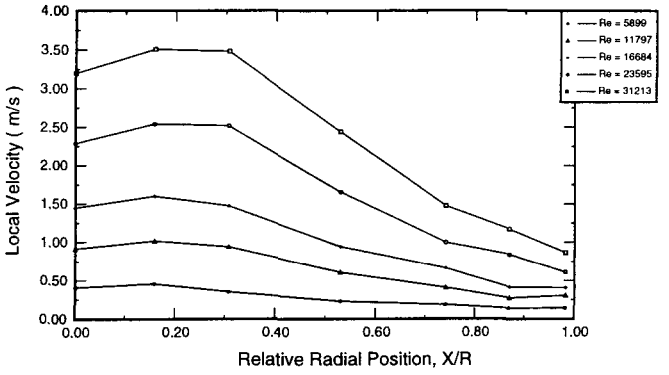

Figure 5.11 Local velocity (horizontal component) along the radius, near the test surface , when all burners are in H0V10

After analyzing the radial variation of the Nusselt number, in the second series of investigations, the angular variation of the local Nusselt number, will be considered in this section. Photographs taken by the infrared camera will be presented to support the results from the heated skin technique as well as to demonstrate the formation of hot spots due to oxidation of the metal. The relative position of the gate, chimney, burners, measuring "key hole" section and the blackened portion can be seen in Figure 5.12. This figure also displays the sections: centre, inner and outer annular zones (strips). The values shown in the parentheses are the respective angular positions in degrees.

The angular distribution of the local Nusselt number over the inner and outer strips, when the burners are in original position, is presented in Figure 5.13. The variation of the local Nusselt Number over the centre, as a function of the Reynolds number, for the same burner setting, is given in Figure 5.14. The heat transfer coefficients are increasing from 30° to 165° over the inner annular zone, while it decreases from 30° to 75° and then increases up to 165° over the outer strip. The increase in the local Nusselt number from 75° to 165° over both the inner and outer rings can also be seen in the IR photos shown in

Figure 5.15. In these photos, the temperature over the inner and outer rings is continuously decreasing from 75° to 165° ,i.e. the local heat transfer coefficient is increasing. Some low temperature zones (i.e. hot spots) are also clearly visible, wherever the burners are directly hitting the surface. For example, two hot spots can be seen very clearly around the angles 120° and 165°, because the jets from burner number five and four respectively are hitting the surface directly and intensifying the heat transfer rate locally. The ratio of the maximum to minimum local *Nu* values is between 1.5-1.7 over the inner annular zone and between 1.3-1.6 over the outer annular zone, depending on the Reynolds number. Another point to be mentioned is at 300°, where a peak is observed. This may be due to the fact that burner #2 impinging directly at this point. The slight decrease over the outer annular zone is likely to be due to less turbulence under this burner (dead zone).

Figure 5.16 shows the angular variation of the local Nusselt number over the inner and outer annular zones, when the burners are set in the H15V10 position. The distribution of the local Nusselt number versus the Reynolds number, over the centre, for the above described burner orientation, can be seen in Figure 5.17. The slope of the curve is less steep over the centre in comparison to the curve for the original burner setting, because in this case the heat transfer intensity has shifted more towards the wall and as a result of this shift the heat transfer rate has decreased over the centre and the inner ring. The ratio of the maximum to minimum local *Nu* values is between 1.5-1.8 over the inner annular zone and between 1.2-1.3 over the outer annular zone, depending on the Reynolds number. The tendency of increasing and decreasing of the heat transfer coefficient along the periphery is also present like in the case of the original burner orientation, because the local impingement of burners increases the heat transfer rate at/around the point of

impingement and at the same time this rate of heat exchange decreases under the burner locations due to weak turbulence (dead zones).

The local Nusselt number distribution along periphery, over the inner and outer rings, when the burners are set in the H10V10 position, is presented in Figure 5.18. The variation of the local Nusselt number as a function of the Reynolds number for the above mentioned burner orientation, is given in Figure 5.19. The variation of the heat transfer coefficient is very similar to that in the case of original burner setting, except that the intensity of the heat transfer is slightly higher in the centre. The ratio of the maximum to the minimum value of the heat transfer coefficient is between 1.3-1.4 over the inner ring and between 1.2-1.3 over the outer ring.

Figure 5.20 displays the angular variation of the local Nusselt number over the inner and outer rings, when the burners are set in the H5V10 position. The distribution of local Nusselt number over the centre as a function of the Reynolds number for the above mentioned burner setting is given in Figure 5.21. The rate of heat transfer in this case has shifted more towards the centre and the inner annular zone. As a result of this shift, the influence of these sections on the overall heat transfer coefficients has also slightly increased. It can also be supported qualitatively by the infrared photos shown in Figure 5.22. It is quite clear in the photos that the temperatures over the outer ring are higher than the temperatures over the inner ring. In this case, formation of the hot spots are also not very significantly visible over the sections shown in the photos. This may be due to the presence of more uniform fluid flow over the heated skin surface, than in any other burner setting. The ratio of the maximum and minimum Nusselt number is varying between 1.7-2.0 over the inner ring and 1.2-1.7 over the outer ring. The heat transfer

coefficient is higher than for any other previously described burner orientation.

The angular distribution of the local Nusselt number over the inner and outer annular zones, when all burners are set in the H0V10 position, is given in Figure 5.23. The variation of local Nusselt number as a function of the Reynolds number over the centre is shown in Figure 5.24. The intensity of heat transfer over the centre is the highest among all burner orientations studied in this thesis work and is very much responsible for the increment in the overall heat transfer coefficient. This increment in the heat transfer coefficient over the centre is almost 3-4 times higher in comparison to the value when burners are arranged in the original position. The intensity of the heat transfer is quite uniform over the outer annular zone and the overall heat transfer coefficient values are higher than the values obtained in any other burner orientation. This phenomena of uniformity over the outer annular zone can also be seen qualitatively in the IR photos shown in Figure 5.25. It should also be mentioned that the temperatures over the inner annular zone are lower than over the outer annular zone, which validates qualitatively the elevated values of the heat transfer coefficient over the inner annular zone. The ratio of the maximum and minimum values of the heat transfer coefficient is varying between 1.6-2.1 over the inner annular zone and between 1.3-1.7 over the outer annular zone.

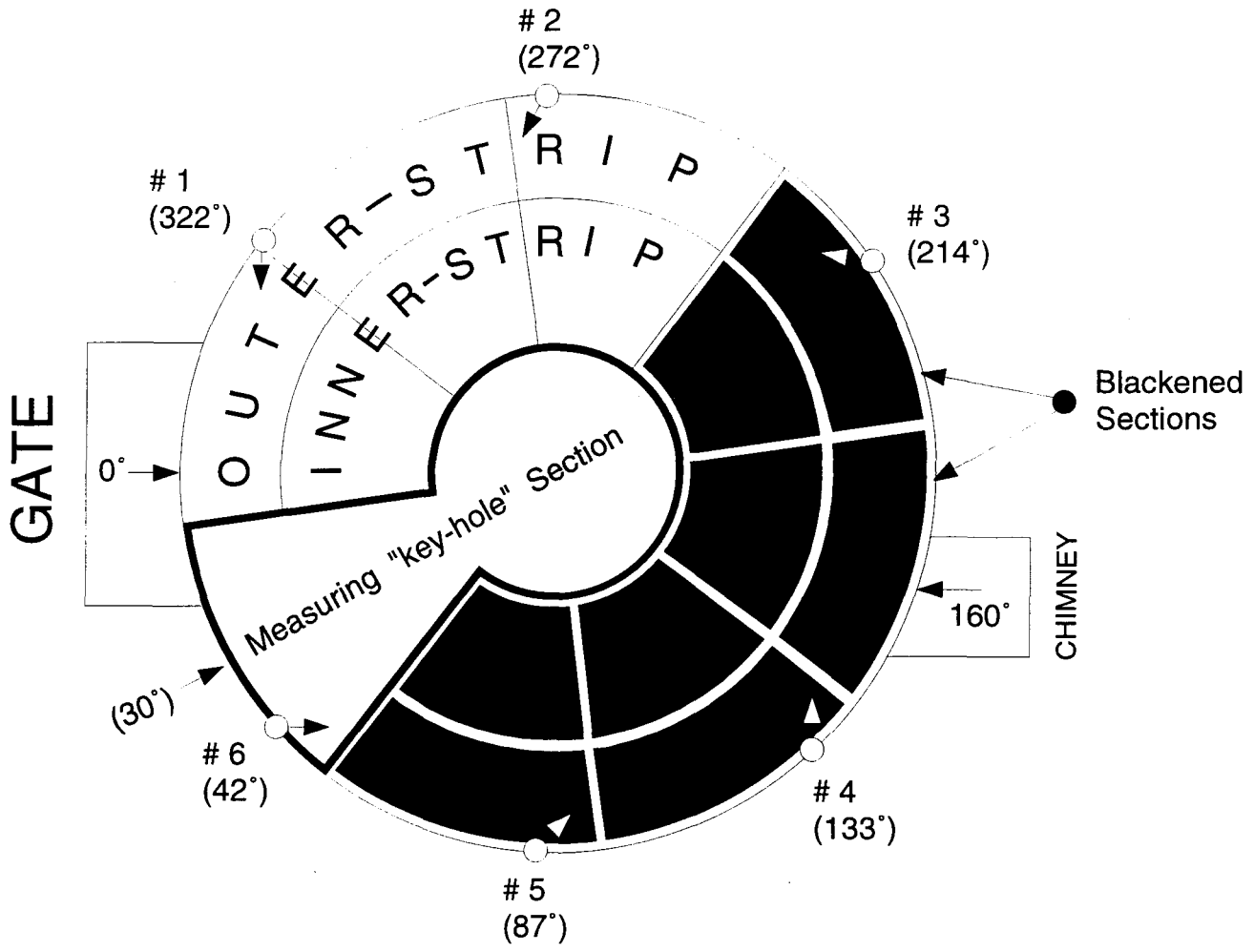

Figure 5.12 Schematic top view of the furnace/flat bath, showing the relative position of the gate, chimney, burners, measuring "key hole" section and the blackened portion

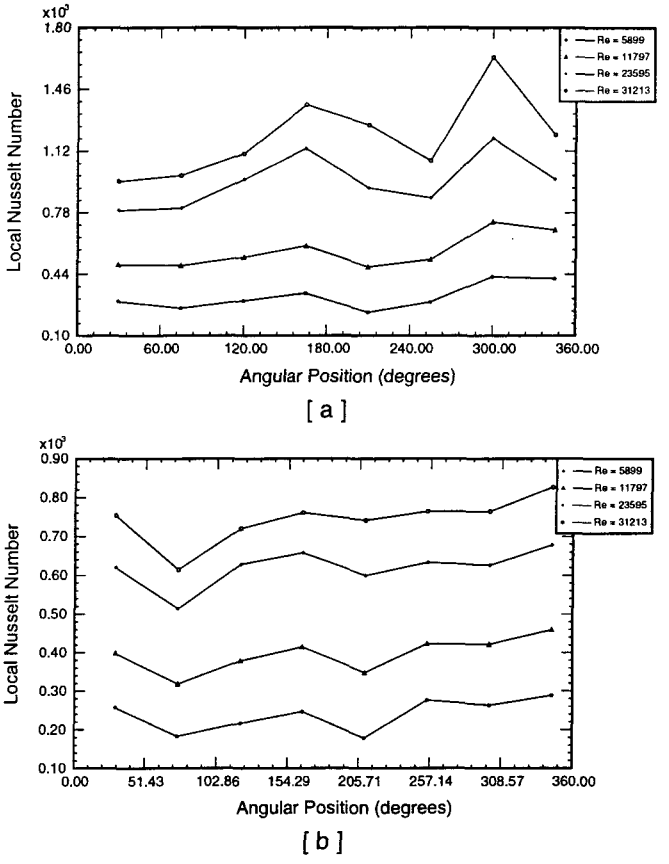

Figure 5.13 Local Nu number over the (a) inner strip, (b) outer strip, along the periphery, when burners are set in the original position

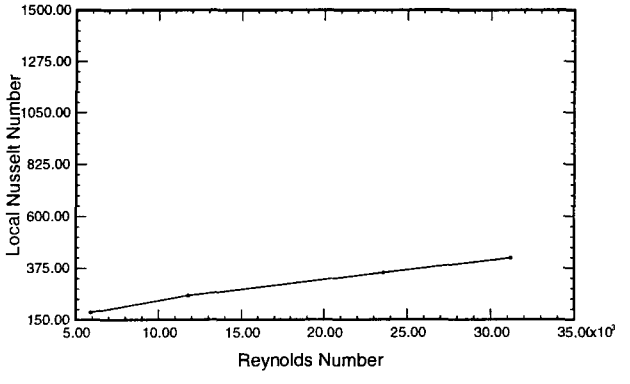

Figure 5.14 Local Nu number over the centre, as a function of the Re number, when burners are set in the original position

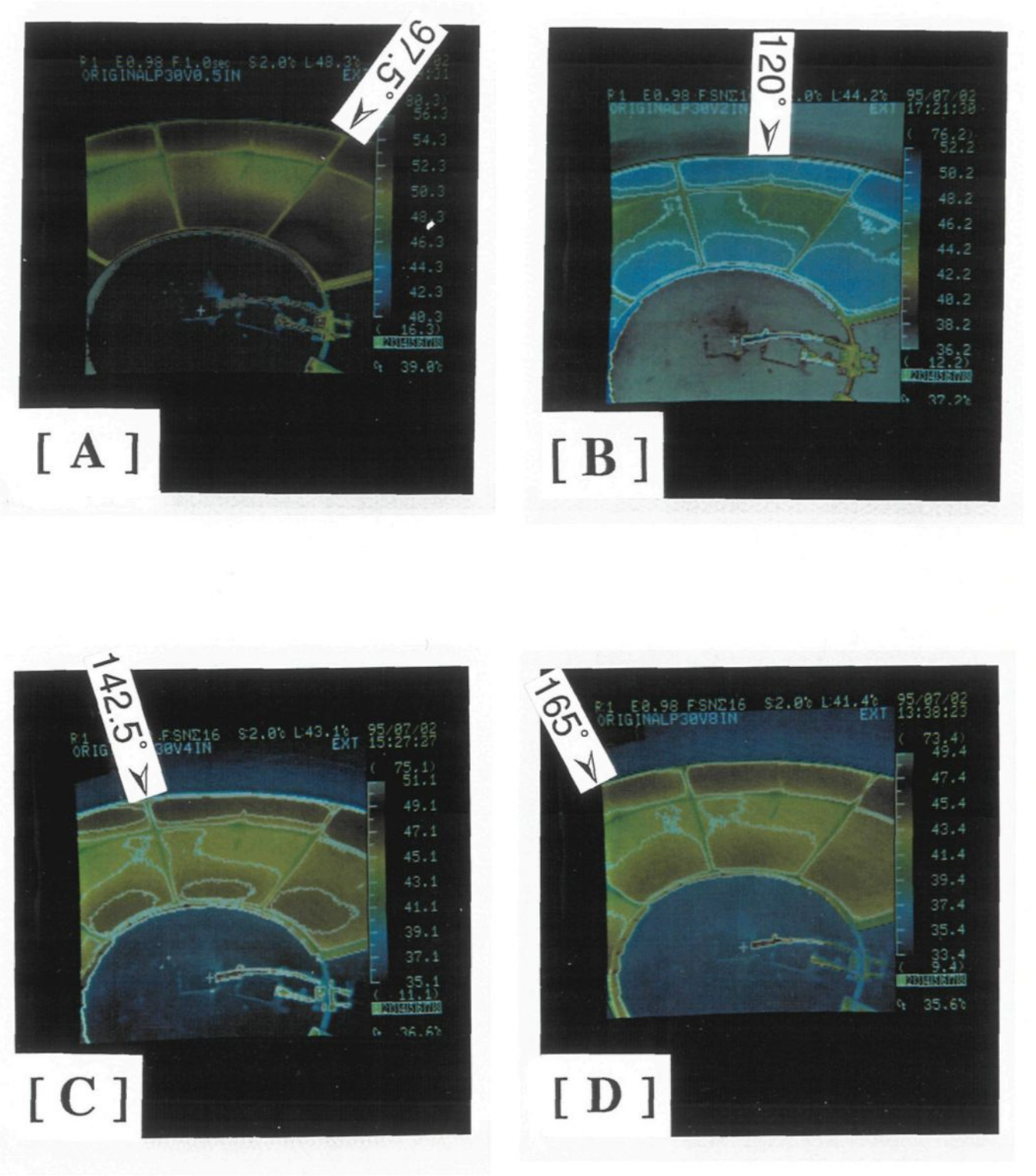

Figure 5.15 IR photos, when burners are in the original position and the Re number is (a) 5899, (b) 11797, (c) 16684, (d) 23595

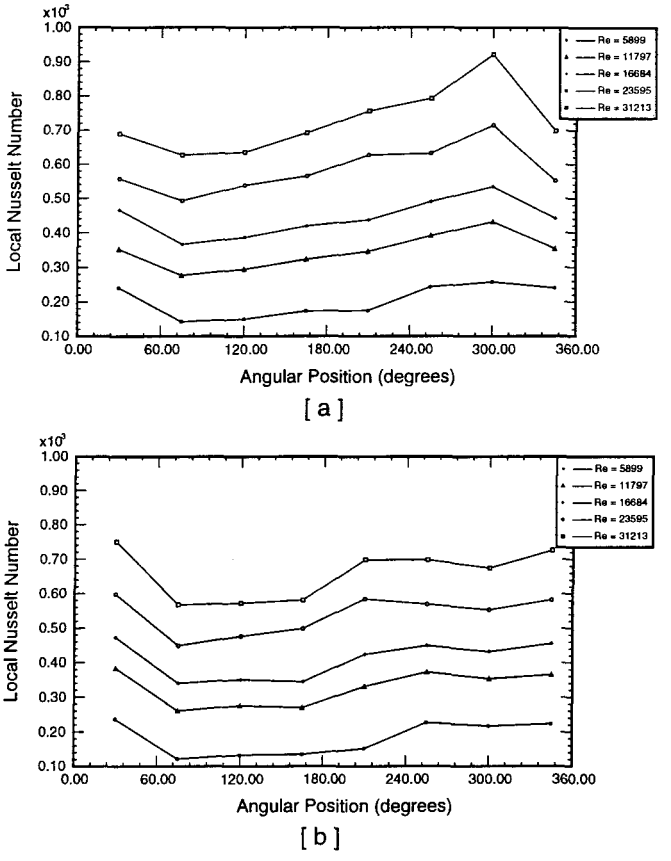

Figure 5.16 Local Nu number over the (a) inner strip, (b) outer strip, along the periphery, when burners are in H15V10

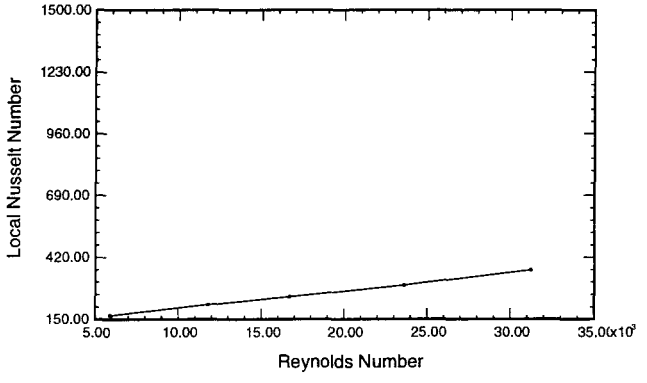

Figure 5.17 Local Nu number over the centre, as a function of the Re number, when burners are in H15V10

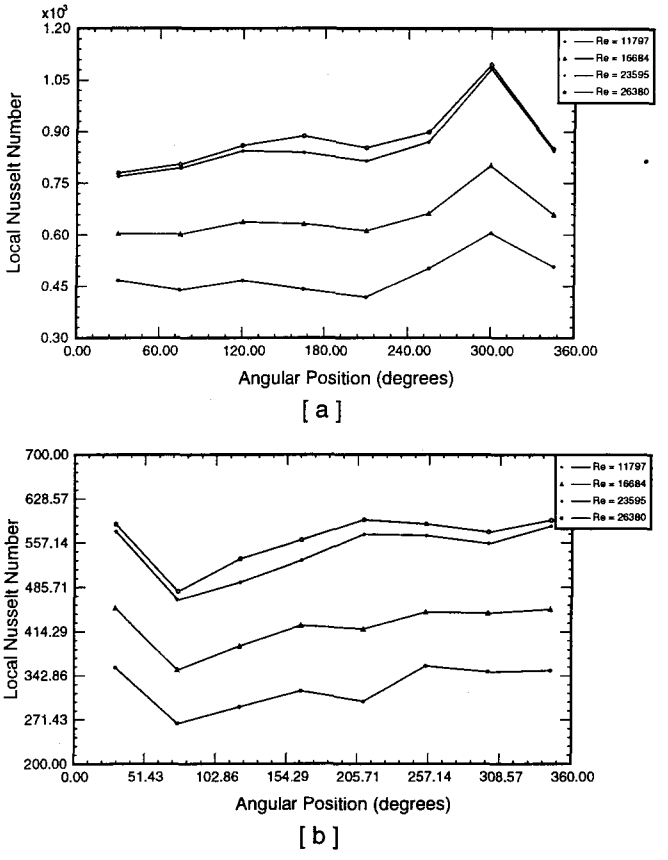

Figure 5.18 Local Nu number over the (a) inner strip, (b) outer strip, as a function of angular position, when burners are in H10V10

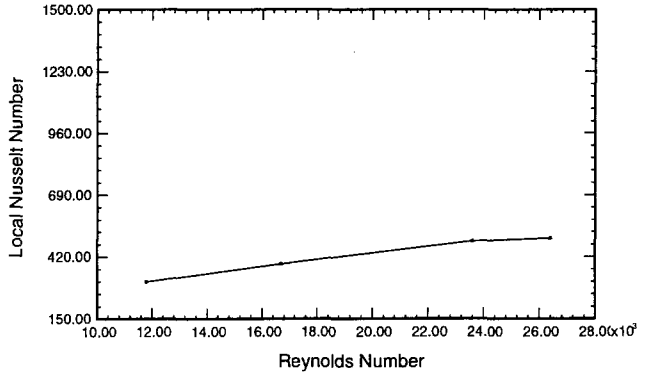

Figure 5.19 Local Nu number over the centre, as a function of the Re number, when burners are in H10V10

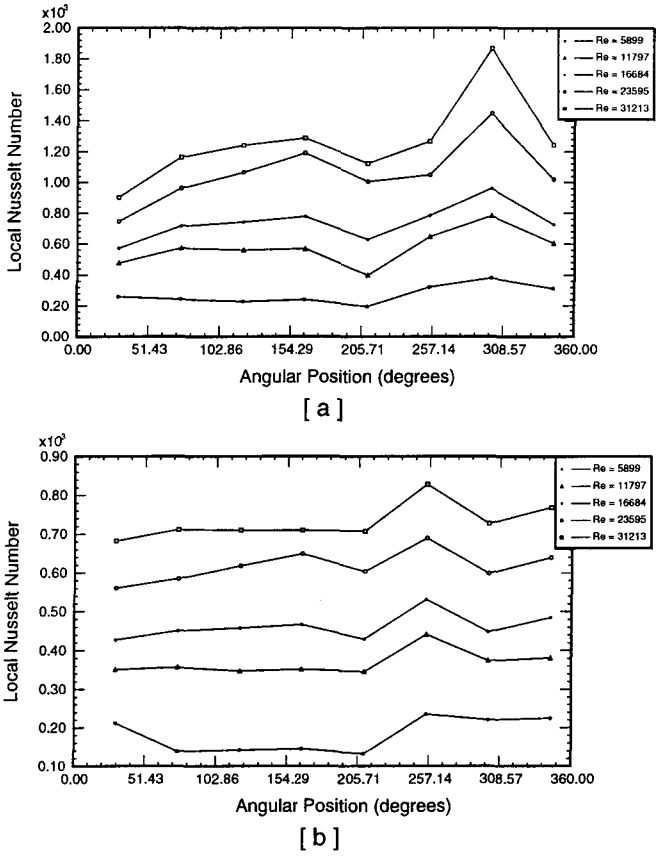

Figure 5.20 Local Nu number over the (a) inner strip, (b) outer strip, along the periphery when burners are in H5V10

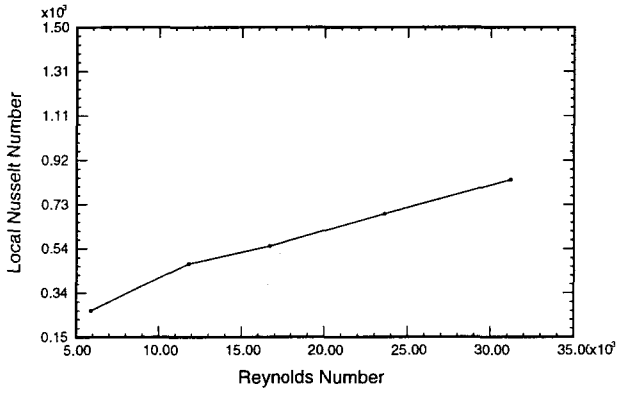

Figure 5.21 Local Nu number over the centre, as a function of the Re number, when burners are in H5V10

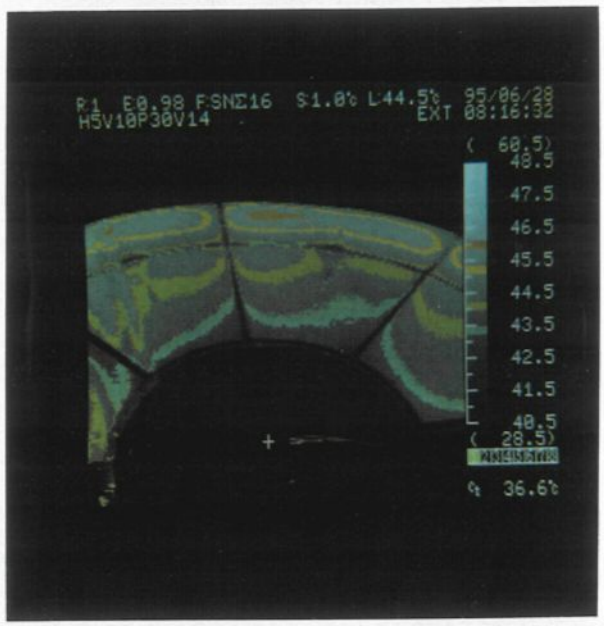

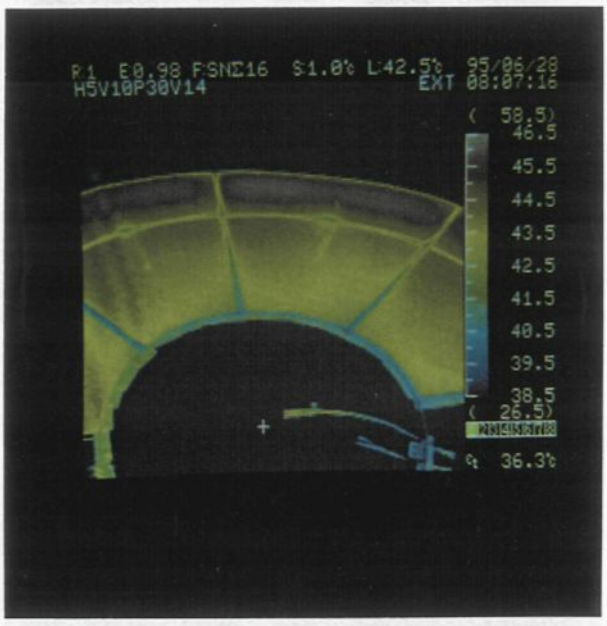

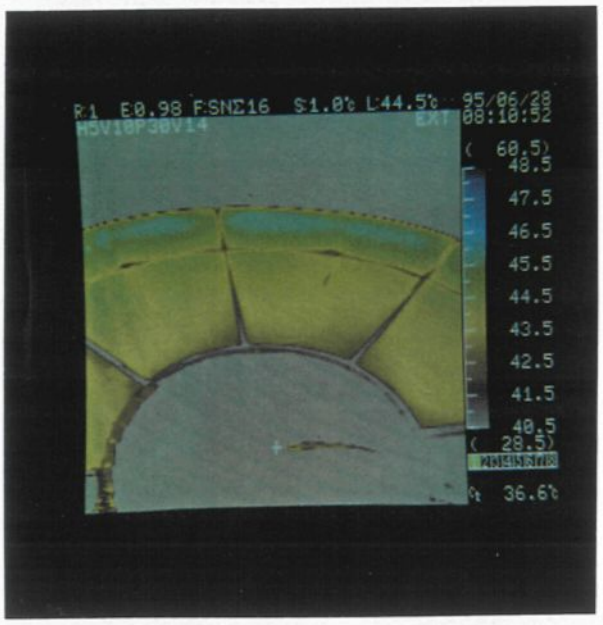

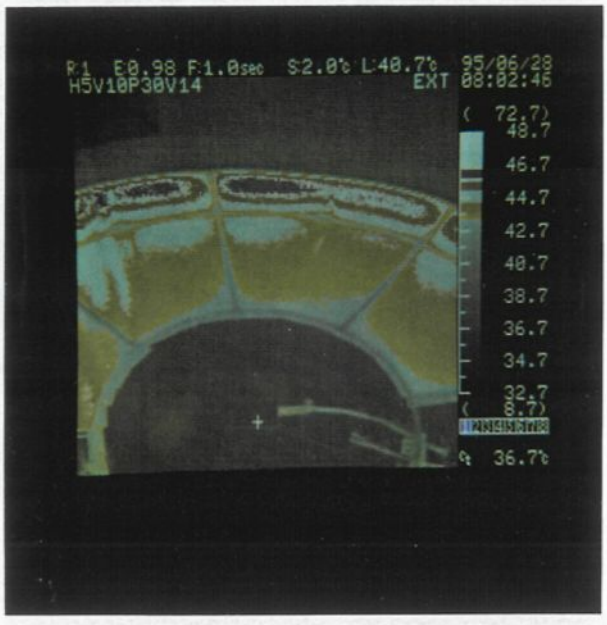

Figure 5.22 IR photos, when burners are in H5V10

and the Re number is 31213 for all the four photos

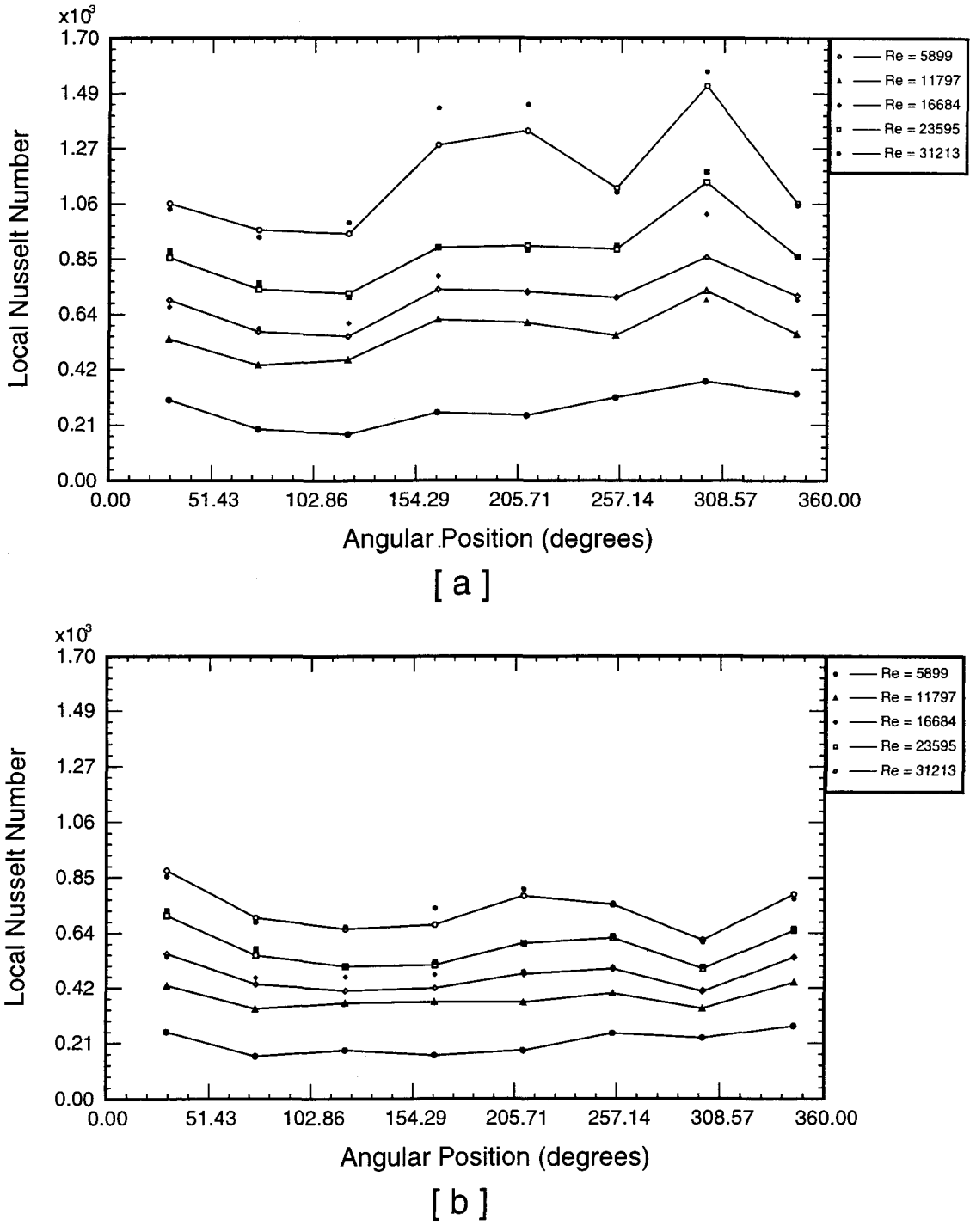

Figure 5.23 Local Nu number over the (a) inner strip, (b) outer strip, along the periphery, when burners are in H0V10 (solid symbols represent the repeated runs)

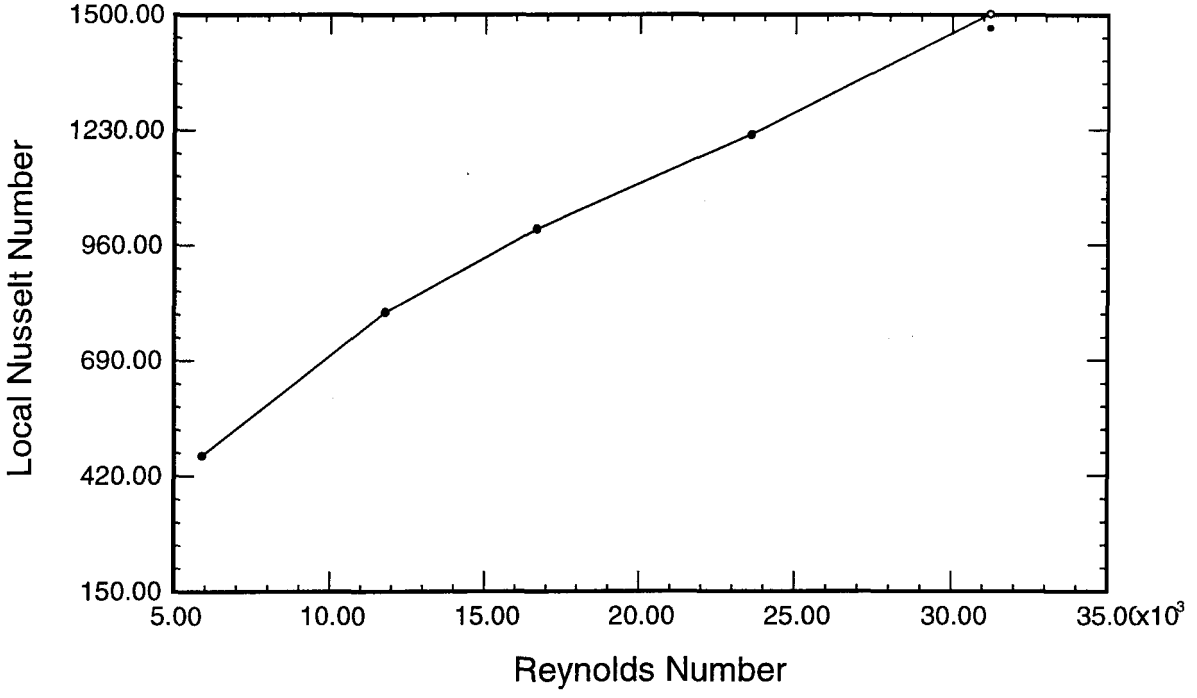

Figure 5.24 Local Nu number over the centre, as a function of the Re number, when all burners are in H0V10 (solid symbol represents the repeated runs)

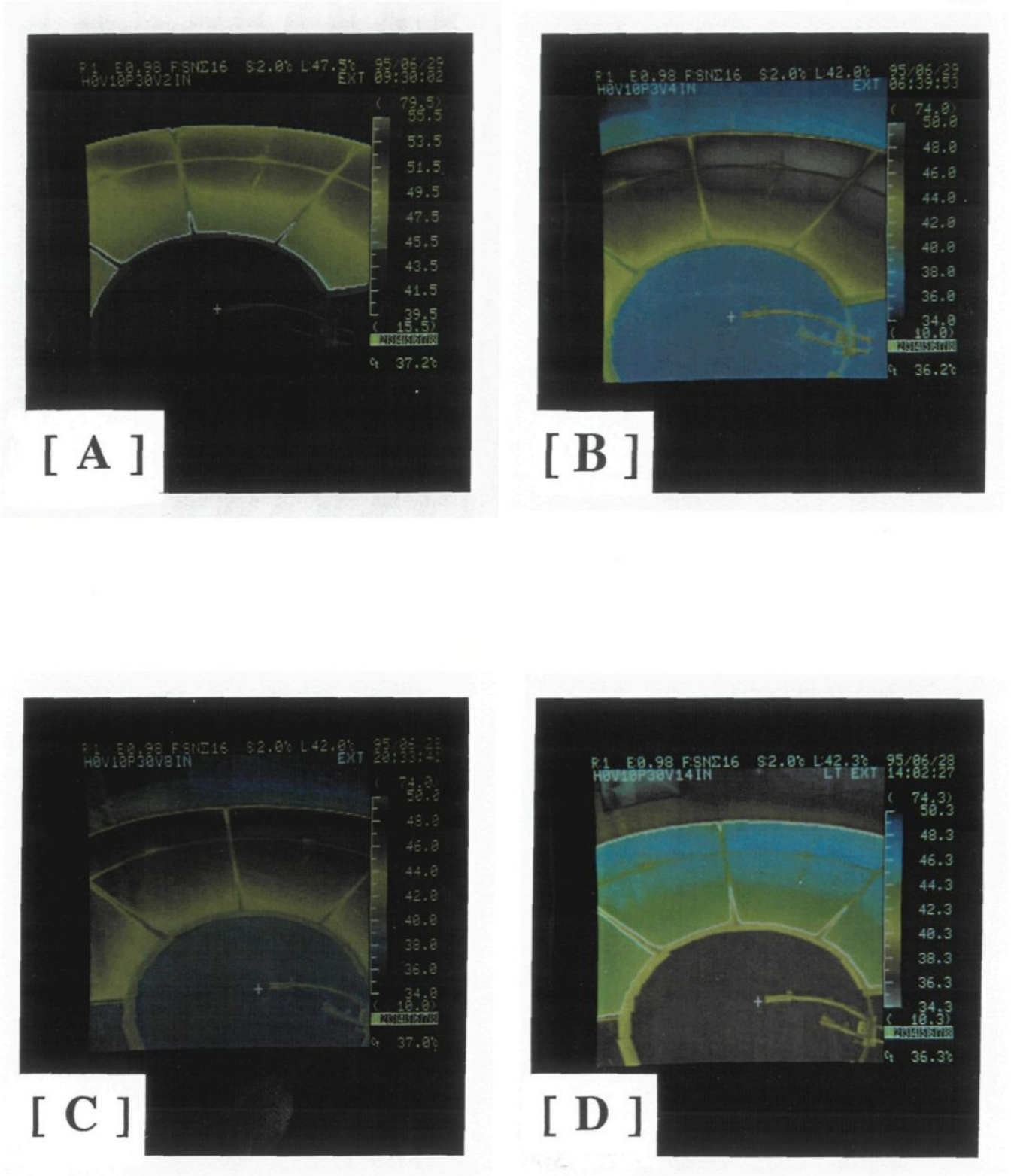

Figure 5.25 IR photos, when burners are in H0V10 and the Reynolds number is (a)11797, (b)16684, (c)23595, and (d)31213

5.3.2 Average Nusselt Number

The method of averaging the Nusselt number has already been explained in section 5.2.1.3. Various approaches for calculating the average Nusselt number as a function of the burner orientation are described. Results are presented in graphical and numerical form. The averaging was done over four different sections: centre, inner strip, outer strip and finally over the whole circular flat bath.

The variation of the average Nusselt number over the inner ring, as a function of the burner orientation in the horizontal plane, while the downward angle in the vertical plane was maintained at 10° for all burner settings, except for the original burner position, is shown in the graphical form in Figure 5.26 and in digital form in Table 5.3. The heat transfer is most intense for the burner orientation H5V10 and is slightly lower for the original and for H0V10 burner orientation. This tendency however does not seem to be valid in the case of low velocities (for Re = 5899), probably due to the presence of fluctuations in the gas stream.

The average Nusselt number distribution over the outer strip, as a function of the burner orientation in the horizontal plane, can be seen graphically in Figure 5.27 and numerically in Table 5.4. In the case of original burner orientation, the heat transfer coefficient over the outer annular zone is highest among all the burner orientations studied. While the heat transfer coefficient for the burner orientation H0V10 is very close to the original burner setting and the value for H5V10 is also comparable to the original set values.

The variation of the average Nusselt number over the centre, as a function of the burner orientation in the horizontal plane is presented graphically in Figure 5.28 and numerically in Table 5.5. It is quite clear from the graphs that the average Nusselt number value over

the centre is lowest for the original burner orientation, except for the H15V10 position. The heat transfer coefficient in the H0V10 setting is higher by approximately 3.5 times than that in the original burner orientation and this ratio is approximately 2 at H5V10.

The distribution of the average Nusselt number over the entire circular flat bath, as a function of the burner orientation in the horizontal plane is presented graphically in Figure 5.29 and numerically in Table 5.6. The average heat transfer coefficients in the cases of burner orientations H0V10 (highest) and H5V10 are higher than that in the case of the original burner orientation, except at lower velocities (Re = 5899) when the burners are in the H5V10 position. It is worthwhile to repeat that this is due to the presence of fluctuations in the gas stream as explained in the flow visualization experiments in Chapter 2, or a difficulty in adjusting the air flow rate. Based on data gathered, there is a strong evidence that the average heat transfer coefficient for the H5V10 orientation with Reynolds number of 23595 was overestimated probably due to a badly adjusted air flow rate. Therefore, this particular value was not considered in the analysis.

A comparative study was done to distinguish the average heat transfer coefficient values over circular and annular sections. In Figure 5.30, three light lines are representing the average Nusselt number distribution over the centre, inner strip and outer strip for the Reynolds numbers 11797 and 23595, while the dark line with triangular symbols in Figure 5.30(a) represents the average Nusselt number distribution over the entire flat bath for the Reynolds number 11797. As it is clear from the graph, the average Nusselt number over the centre follows the trend as below:

H0V10 > H5V10 > H10V10 > Original > H15V10

this sequence of the average Nusselt number over the inner strip is:

$$H5V10 > Original \geq H0V10 > H10V10 > H15V10$$

over the outer strip as follows:

$$Original \geq H0V10 \geq H5V10 > H10V10 > H15V10$$

and, over the entire circular flat bath as follows:

$$H0V10 > H5V10 > Original > H10V10 > H15V10$$

Figures 5.31 to 5.34 show the variation of average Nusselt number as a function of the Reynolds number over the whole flat bath, centre, inner annular zone and outer annular zone respectively. The intensity of the heat transfer over the center is higher for the orientations H0V10, H5V10 and H10V10 than in the original orientation (see Figure 5.32). Over the inner annular zone, the heat transfer coefficient is highest for the burner orientation H5V10 (see Figure 5.33). Over the outer annular zone, it is highest in the case of the original orientation (see Figure 5.34). Globally, the average heat transfer coefficient is higher for H0V10 (highest) and H5V10 than for original position (see Figure 5.31).

The dependence of the flow velocity on the heat transfer coefficient over the entire circular flat bath was also analyzed quantitatively in the Reynolds number range 6×10^3 - 3×10^4, for various rotational and axial burner orientations as shown in Table 5.2. The observations made earlier are cast in a correlation relating the Reynolds and Nusselt numbers. It is seen that the power n is higher for the burner orientations H0V10 and H5V10 than for the original position.

$$Nu_{avg} = C \cdot Re^{n}$$

Burner Orientation	C	n
H15V10	0.36	0.72
H10V10	0.41	0.73
Original	0.46	0.73
H5V10	0.33	0.77
H10V10	0.30	0.79

Table 5.2 Dependence of the average Nu number on the Re number over the circular flat bath

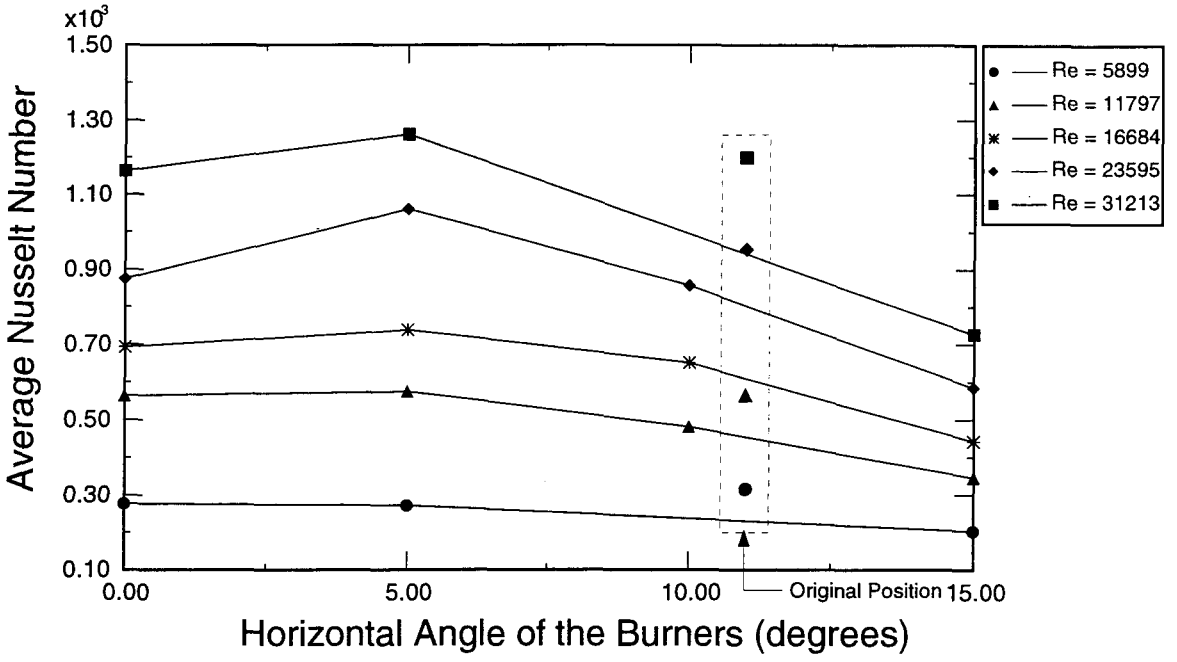

Figure 5.26 Average Nu number over inner strip, as a function of the burner orientation in the horizontal plane

Reynolds Number	**Average Nusselt number over inner strip for the burners orientation:**				
	H0V10	H5V10	H10V10	Original	H15V10
5899	276.992	272.288	—	315.584	202.626
11797	564.096	575.902	481.088	565.344	346.113
16684	692.448	738.304	651.040	—	442.626
23595	874.368	1061.344	856.896	953.344	584.8312
26380	—	—	878.112	—	—
31213	1163.550	1262.400	—	1198.98	726.432

Table 5.3 Average Nu number values over the inner strip of the flat circular bath for various Re numbers

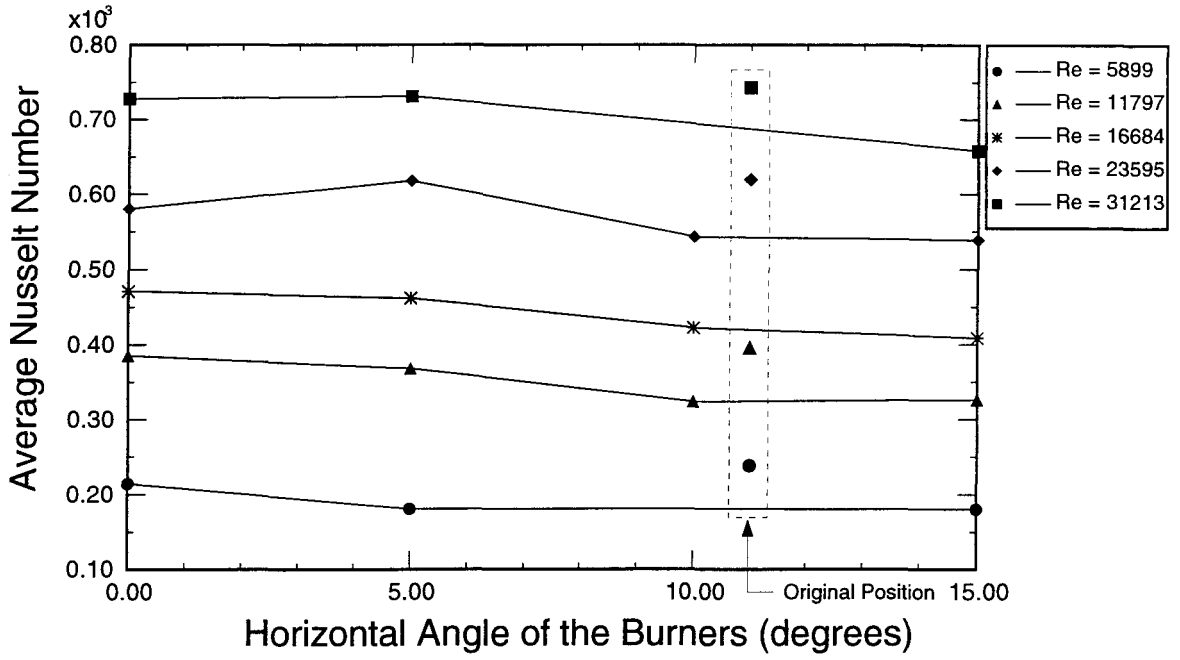

Figure 5.27 Average Nu number over the outer strip, as a function of the burner orientation in the horizontal plane

Reynolds Number	**Average Nusselt number over outer strip for the burners orientation:**				
	H0V10	H5V10	H10V10	Original	H15V10
5899	214.464	180.992	—	238.400	180.287
11797	385.344	368.416	323.744	395.296	326.270
16684	471.200	461.856	422.176	—	408.446
23595	580.416	618.176	542.688	619.488	538.657
26380	—	—	563.616	—	—
31213	727.296	730.976	—	742.912	658.304

Table 5.4 Average Nu number over the outer strip, for various Re numbers,

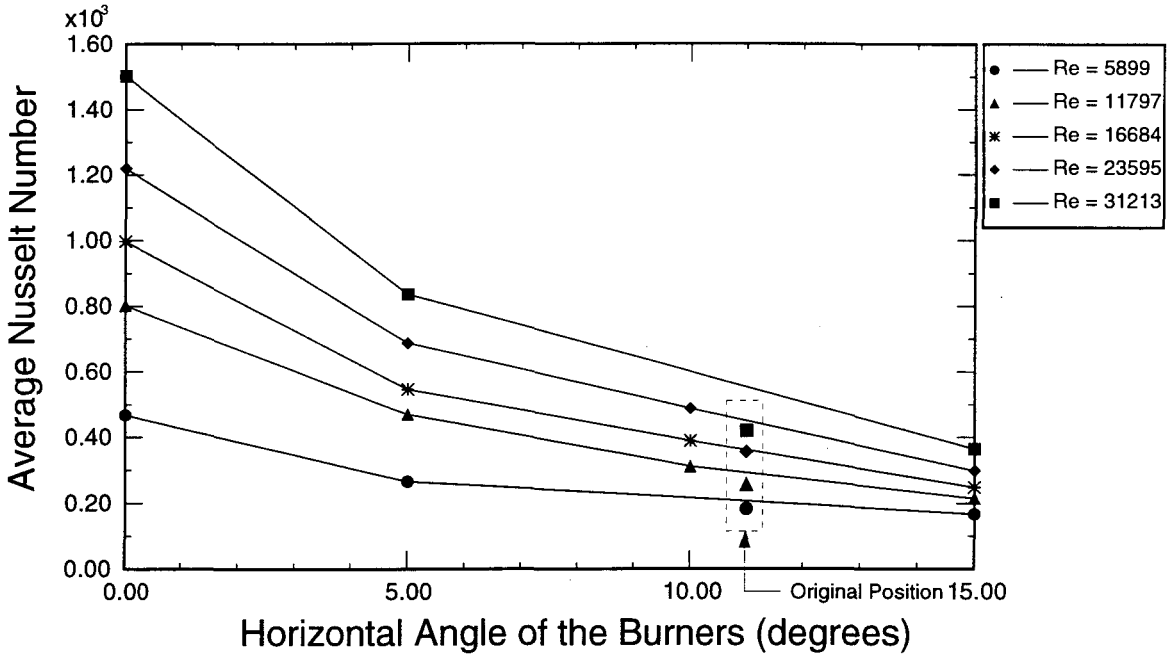

Figure 5.28 Average Nu number over the centre, as a function of the burner orientation in the horizontal plane

Reynolds Number	**Average Nusselt number over centre for the burners orientation:**				
	H0V10	H5V10	H10V10	Original	H15V10
5899	467.456	265.728	—	182.528	166.400
11797	802.304	469.504	311.296	255.488	214.020
16684	996.608	546.304	389.12	—	247.810
23595	1219.072	687.872	487.936	355.328	297.730
26380	—	—	500.736	—	—
31213	1501.696	837.376	—	419.328	364.290

Table 5.5 Average Nu number values over the centre for various Re numbers

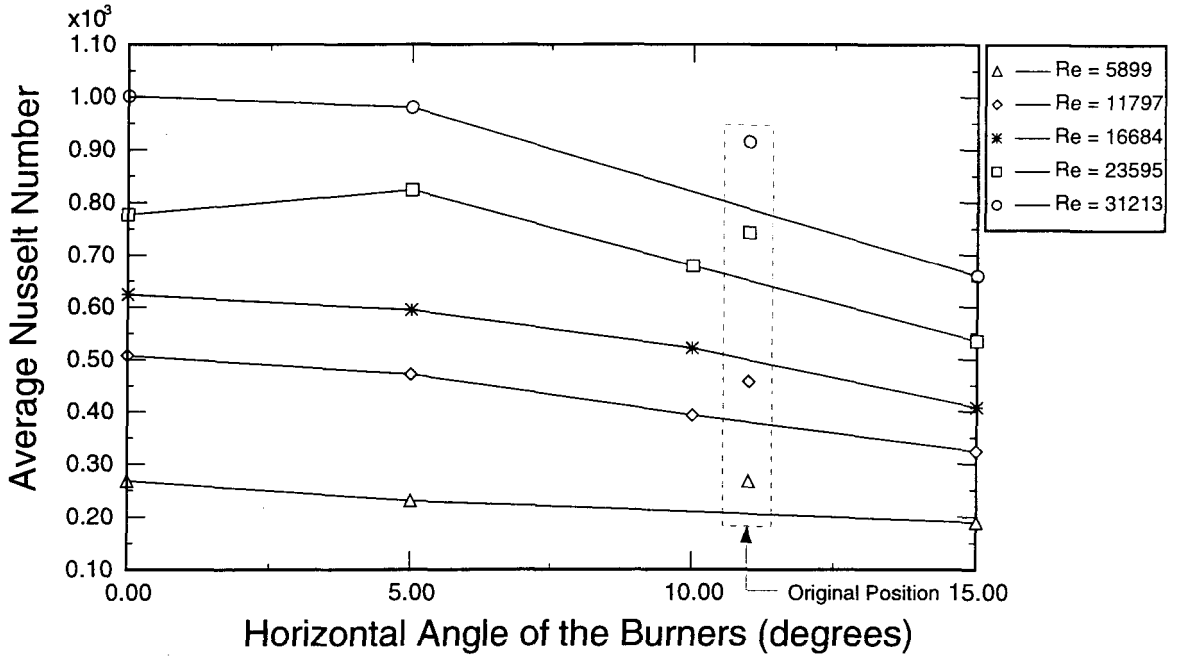

Figure 5.29 Average Nu number over the flat bath, as a function of the burner orientation in the horizontal plane for the Re numbers ranging from 5899 to 31213

Reynolds Number	**Average Nusselt Number for Burners Orientation:**					
	H15,V10	H10,V10	H5,V10	H0,V10	H0,V10 (repeated)	Original Position
5.899e3	188.920	—	230.597	268.176	267.290	267.428
1.1797e4	323.823	393.191	471.891	507.885	506.491	457.558
1.6684e4	407.543	521.676	594.636	623.817	645.805	—
2.3595e4	535.015	678.343	824.383	777.171	785.508	742.772
2.6380e4	—	698.5878	—	—	—	—
3.1213e4	659.153	—	980.559	1001.742	1015.69	915.097

Table 5.6 Average Nusselt number values over the flat bath for various Re numbers

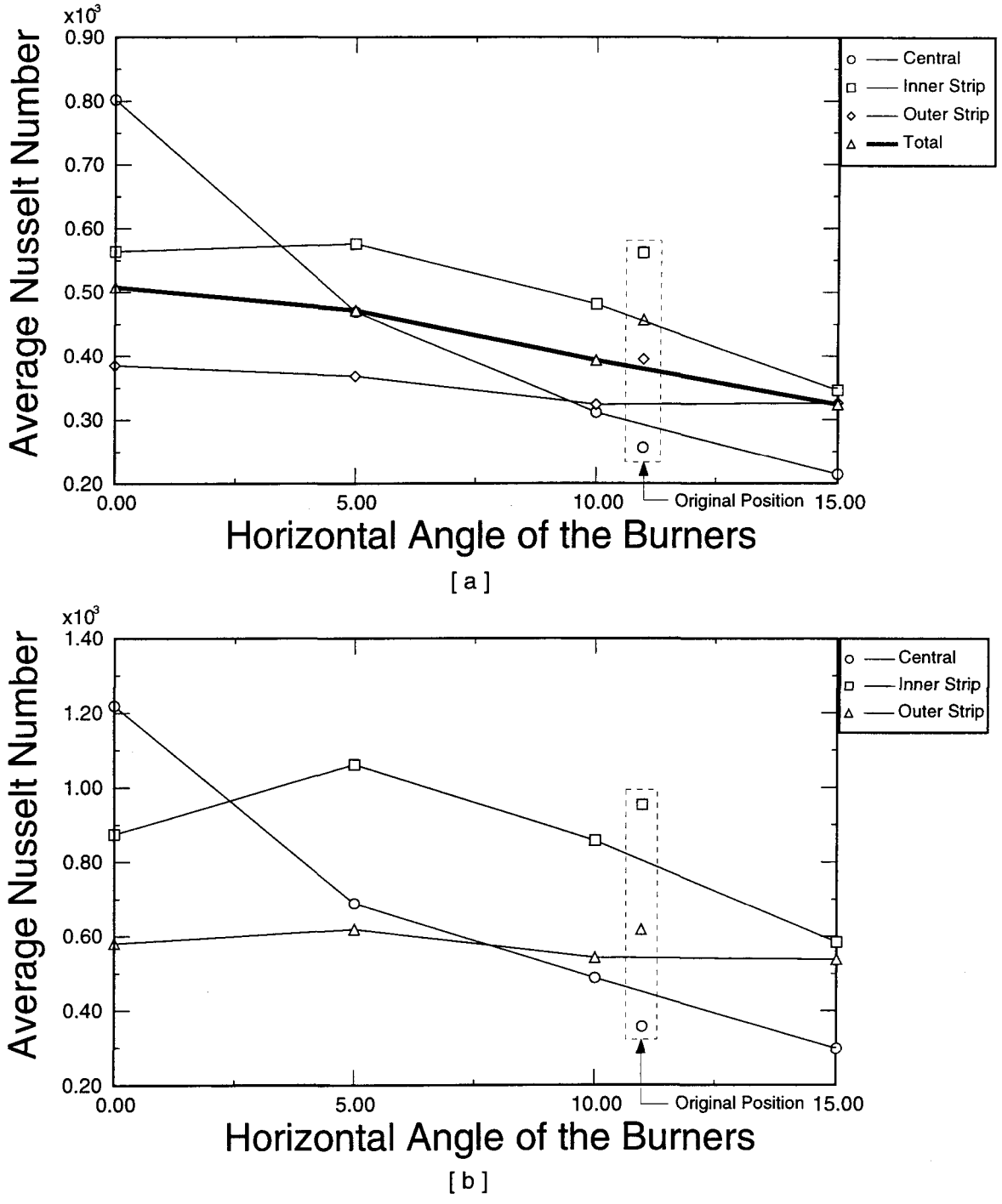

Figure 5.30 Average Nu number over centre, inner and outer strip, as a function of the burner orientation in the horizontal plane, for the Re number (a) 11797, (b) 23595

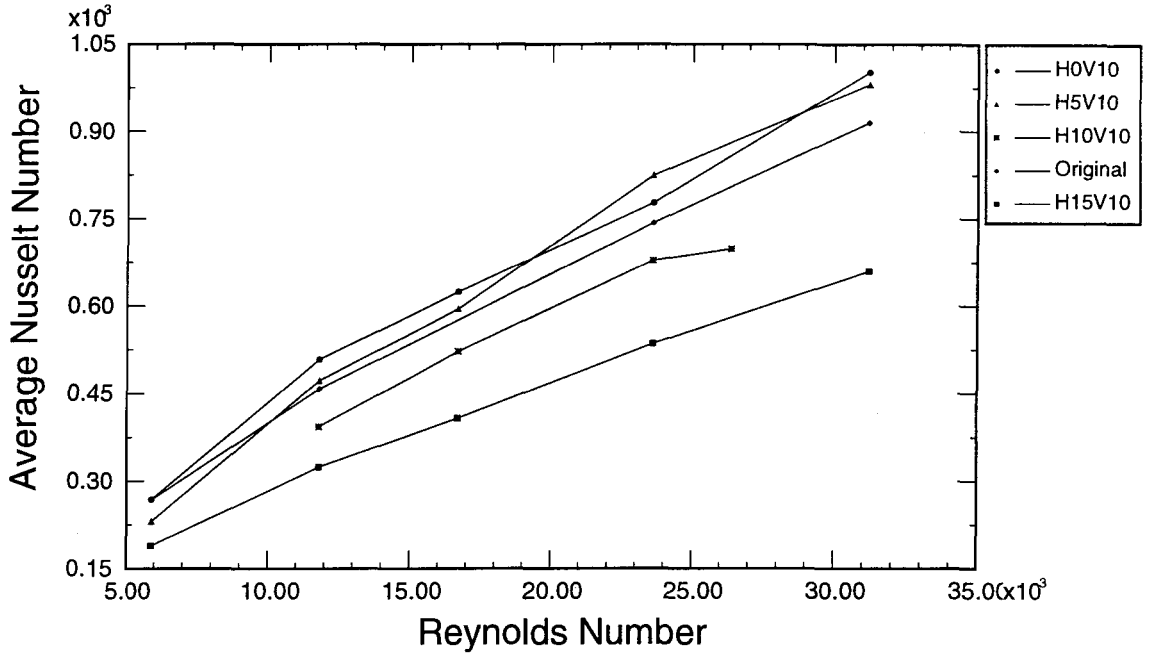

Figure 5.31 Average Nu number over the circular flat bath, as a function of the Re number for various burner orientations as mentioned in the legend

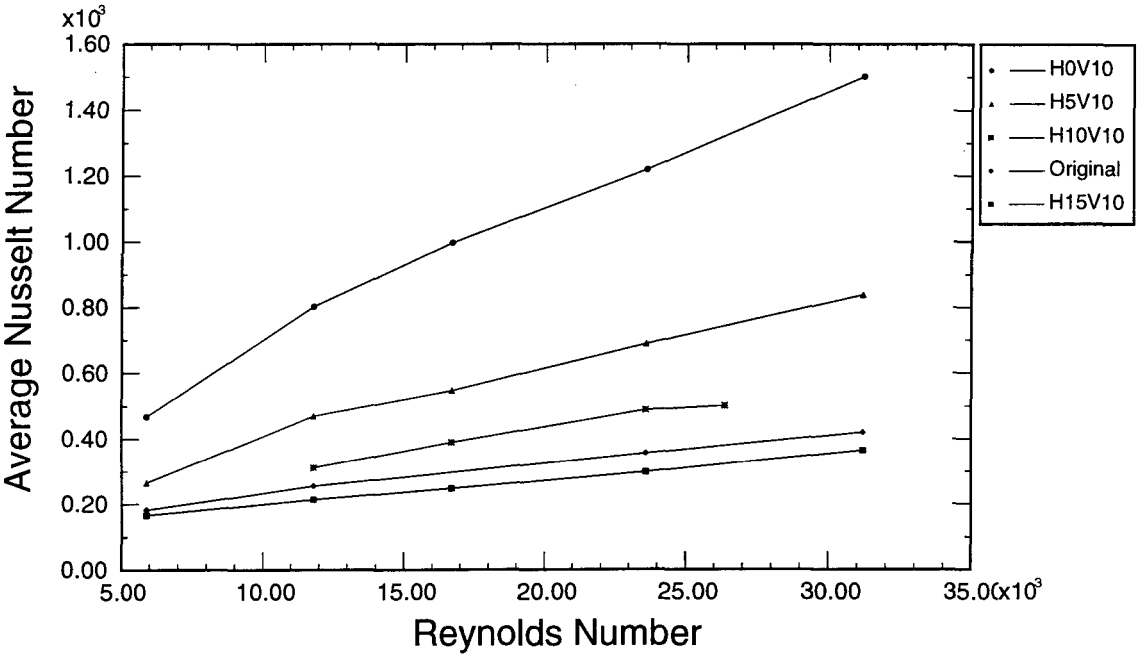

Figure 5.32 Average Nu number over the centre, as a function of the Re number for various burner orientations

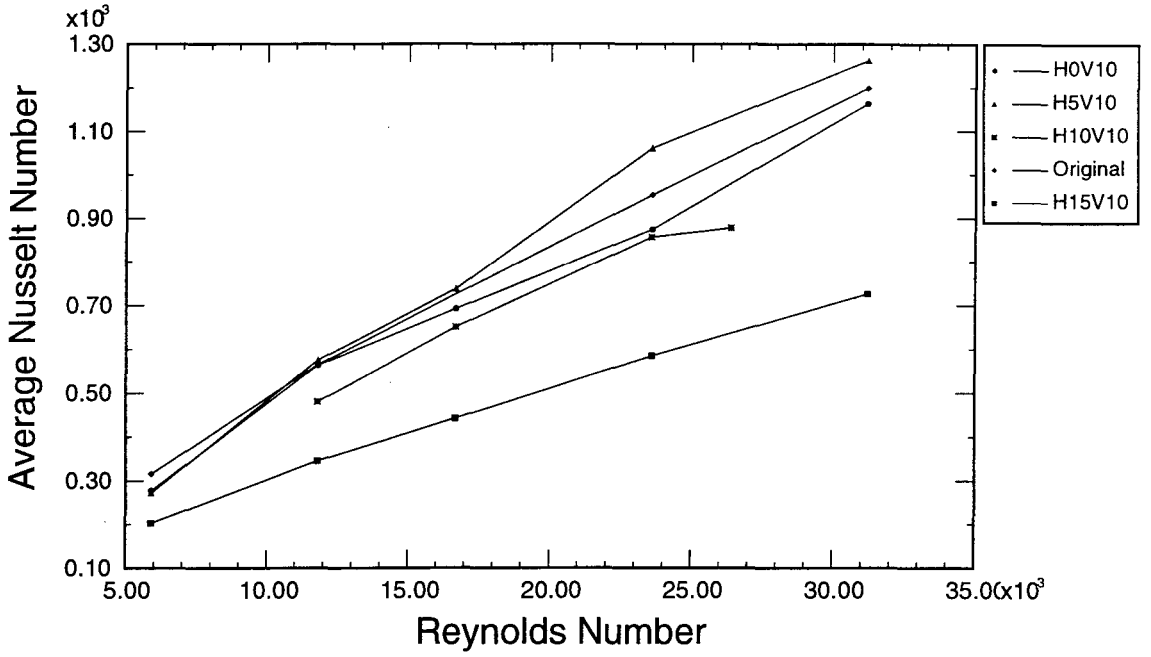

Figure 5.33 Average Nu number over the inner strip, as a function of the Re number for various burner orientations

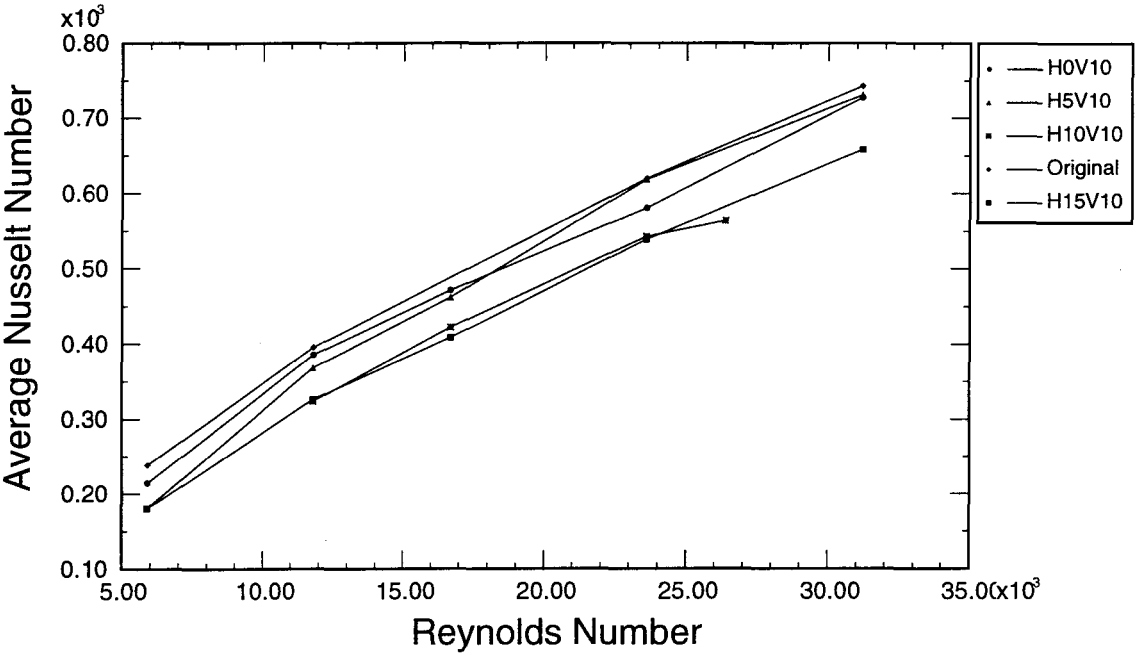

Figure 5.34 Average Nu number over the outer strip, as a function of the Re number for various burner orientations

5.3.3 Repeatability of Results

Repeatability tests were performed for the burner orientation where all burners are pointing toward the centre and making 10° downward in the vertical plane, for the Reynolds numbers: 5.9×10^3, 1.18×10^4, 1.67×10^4, 2.36×10^4, and 3.12×10^4. The results are shown graphically in Figures 5.23 and 5.24, where the local Nusselt number is plotted versus the angular position. Numerically, it is presented in Table 5.6 for the average Nusselt number. In these Figures, the original runs are marked by hollow symbols, while the repeated runs are marked by solid symbols. The experimental data points from the repeated runs fall within ± 3% of those from the original runs. This agreement between the original runs and the repeated runs is well within the experimental uncertainties.

Chapter 6

CONCLUSIONS AND RECOMMENDATIONS

6.1 REVIEW OF THE THESIS

The work presented in this thesis was undertaken to determine the values and distribution of the heat transfer coefficients along the circular molten metal flat bath in a circular remelting furnace. A method called the "heated skin technique" was developed to measure local heat transfer data. The development of this technique was one of the major goals of this work. The accuracy of the heated skin technique is comparable to many of the other available techniques for taking local heat transfer measurements, and the instrumentation and the equipment required to use the technique are commercially available and relatively inexpensive to purchase.

Five sets of experimental runs were performed with the Reynolds numbers ranging from 6×10^3 to 3×10^4. Five different axial and rotational burner orientations were studied. The experimental repeatability of the average Nusselt number was found to be within $\pm$ 3%, as observed for one setting of burner orientation.

The most important findings may be summarized as follows.

In the case of rotating flow patterns (H5V10, H10V10, Original, and H15V10), the intensity of the heat transfer is higher over the inner annular zone, while it is most intense

in the centre for burner orientation H0V10. The overall average heat transfer coefficient was found to be the highest for the orientation H0V10, while that for burner orientation H5V10 proved to be higher than in the case of the original setting.

The orientation H0V10 is the best burner arrangement from the point view of heat transfer, but there are chances of metal burning (oxidation of metal) due to direct intense impingement of flue gases into the metal pile. Therefore, the only burner orientation which can provide better heat transfer over the given orientation is the **H5V10**.

6.2 SUGGESTIONS FOR IMPROVEMENTS AND EXTENSIONS

The results obtained with the heated skin technique for taking local forced convection heat transfer data were quite encouraging. It is felt that it would be worthwhile to continue the development of the heated skin technique with a goal of reducing the experimental uncertainties. The two largest sources of uncertainties in the technique are due to: (i) fastening of the heat flux and temperature sensors, (ii) the uncertainties in determining conduction heat losses.

The fastening of the thermocouples and heat flux sensors is very important to avoid the creation of an additional thermal resistance between the test surface and the sensor. Secondly, the use of a guard heater below the heated skin may be used to compensate the downward conduction, thus eliminating the uncertainties in determining conduction heat losses. A diagram was prepared to give an idea about this "guard heater technique" as applied to a surface inside the physical model, see Figure E.1. The principle is also described in Figure 4.2.

It is recommended that the heated skin technique be evaluated as a potential technique for taking local forced convection heat transfer measurements. The successful completion

of this project would establish the heated skin technique as a convenient and effective way of measuring local heat transfer coefficients in natural, forced and mixed convection problems, with laminar and turbulent fluid flows.

BIBLIOGRAPHY

1. S. Ashforth, R.J. Edwards, D.P. Draham, B.J. Lowesmith, K. Jamunathan, and J.M. Rhine. Measurement of convective heat transfer coefficients, on the ligaments of a model shell boiler tube plate, using liquid crystal thermography. *3rd U.K. National Conference on Heat Transfer*, 1:351–359, 1992.

2. S. Bahl and J.A. Liburdy. Measurement of local convective heat transfer coefficients using three-dimensional interferometry. *International Journal of Heat and Mass Transfer*, 34(4/5):949–960, 1991.

3. D.L. Balageas, D.M. Boscher, and A.A. Déom. Measurement of convective heat transfer coefficients on a wind tunnel model by passive and simulated infrared thermography. In *Infrared Technology XVI*, volume 1341, pages 339–359. SPIE, 1990.

4. J.W. Baughn, P.T. Ireland, T.V. Jones, and N. Saniei. A comparison of the transient and heated-coating methods for the measurement of local heat transfer coefficients on a pin fin. *Journal of Heat Transfer*, 111:887–881, 1989.

5. J.W. Baughn, R.K. Takahashi, M.A. Hoffman, and A.A. Mckillop. Local heat transfer measurements using an electrically heated thin gold-coated plastic sheet. *Journal of Heat Transfer*, 107:953–959, 1985.

6. T.P. Bligh and D.M. Apthrop. Heat flux sensor calibration technique. In *Building Applications of Heat Flux Transducers*, pages 25–44. ASTM Special Technical

Publication 885, 1983.

7. T. Bourgeois, A. Chapdelaine, and A. Larouche. Optimal metal stirring with ajs in round, top charged melters. In *Recent Metallurgical Advances in Light Metals Industries, 34th CIM Conference*, pages 389–400, Vancouver, Canada, August 20-24, 1995.

8. C. Camci, K. Kim, S.A. Hippensteele, and P.E. Poinsatte. Convection heat transfer at the curved bottom surface of a square to rectangular transition duct using a new hue capturing based liquid crystal technique. *Fundamental Experimental Measurements in Heat Transfer, ASME*, 179:7–22, 1991.

9. M.G. Davies. Non-dimensionalizing the convective heat transfer coefficient. *International Journal of Mechanical Engineering Education*, 115(4):227–281, 1986.

10. G.M. Dvorina, A.A. Ruzmaikin, and D.D. Sokolov. Hot spots in a turbulent flow with heat liberation. *Plenum Publishing Corporation*, pages 610–615, 1990.

11. E.R.G. Eckert and R.J. Goldstein. *Measurement Techniques in Heat Transfer.* Technivision Services, 1970.

12. R.J. Emrich. *Methods of Experimental Physics*, volume 18 of *part B*. Academic Press, 1981.

13. M. Fishenden and O.A. Saunders. The calculation of heat transmission. *HMSO, London*, 15:91, 1932.

14. E. Gartenberg and R.E. Wright Jr. Problems and solutions for transition detection in cryogenic wind tunnels by infrared imaging. pages 156–168.

15. W.H. Giedt. Investigation of point unit heat transfer coefficient around a cylinder normal to an air stream. *Trans. ASME*, 71:375–381, 1949.

16. W. Hauf and U. Grigull. *Advances in Heat Transfer*, volume 6, pages 134–366. Academic Press, 1970.

17. S.A. Hippensteele, L.M. Russell, and F.S. Stepka. Evaluation of a method for heat transfer measurements and thermal visualization using a composite of a heater element and liquid crystals. *Journal of Heat Transfer*, 105:184–189, 1983.

18. J.P. Holman. *Experimental Methods for Engineers*. McGraw-Hill, Inc., sixth edition, 1994.

19. P. Jain, L.I. Kiss, A. Charette, and R.T. Bui. Développement de la technique de la peau chauffante pour la mesure du coéfficient de transfert de chaleur. In *ACFAS*, volume 63, page 179, Chicoutimi, Québec, Canada, May 22-26, 1995.

20. L.V. King. On the convection of heat from small cylinders in a stream of fluid, with application to hot-wire anemometry. *Phil. Trans. Roy. Soc. London*, 214(14):373, 1914.

21. L.I. Kiss, H. Boily, B. Fall, P. Jain, and P. Paquette. Flow structure in a six-burner round furnace (video recording, 17 min.). Technical report, UQAC/CHIP, 1993.

22. L.I. Kiss, A. Charette, and R.T. Bui. Experimental methods and facilities for the study of oswego type furnaces. Technical Report 26, GRIPS/UQAC, 1992.

23. L.I. Kiss, A. Charette, and R.T. Bui. Flow structure in circular remelting furnaces. Technical Report CHIP-11, Université du Québec à Chicoutimi, 1993.

24. L.I. Kiss, A. Charette, R.T. Bui, T. Bourgeois, and E. Rauch. Flow management in

circular furnaces. In *Developments in Light Metals, 33rd CIM Conference*, pages 443–454, Toronto, Canada, August 20-25, 1994.

25. L.I. Kiss, P. Jain, A. Charette, and R.T. Bui. The effect of modified burner orientation on the flow structure in a circular furnace. Technical Report CHIP-13, Université du Québec à Chicoutimi, 1994.

26. L.I. Kiss, P. Jain, A. Charette, and R.T. Bui. Experimental methods for the study of convective heat transfer in circular furnaces. In *Combustion and Fire Safety, 9th International THERMO Conference*, pages 331–335, Budapest, Hungary, June 14-16, 1995.

27. L.I. Kiss, P. Jain, A. Charette, R.T. Bui, and T. Bourgeois. Convective heat transfer along the surface of the molten metal in a round furnace. In *Recent Metallurgical Advances in the Light Metals Industries, 34th CIM Conference*, pages 401–412, Vancouver, Canada, August 20-24, 1995.

28. L.I. Kiss, P. Jain, B. Fall, and P. Paquette. Flow visualization in circular remelting furnaces (video recording, 12 min.). Technical report, UQAC/CHIP, 1992.

29. J.S. Kraabel and J.W. Baughn A.A. Mckillop. An instrument for the measurement of heat flux from a surface with uniform temperature. *Journal of Heat Transfer*, 102:576–578, 1980.

30. T. Kumada. Proposed method for measuring local heat transfer coefficients of isothermal surfaces. *Journal of Heat Transfer, Transactions of the ASME*, 111:858–863, 1989.

31. T. Kunitomo, M. Fujita, and H.M. Shafey. The effect of paint coating on heat transfer. *Scripta Technica*, 15(6):17–31, 1986.

32. D.R. Lide and H.P.R. Frederikse. *Handbook of Chemistry and Physics*. CRC Press, 75th edition, 1995.

33. K.D. Maglić, A. Cezairliyan, and V.E. Peletsky. *Compendium of Thermophysical Property Measurement Methods*, volume 1. Plenum Press, 1984.

34. MetraByte Corporation. *Data Acquisition and Control*, 1984.

35. Mikron Instruments Company, Inc. *Infrared Thermo Tracer*, 1990.

36. T. Mizushina. *The Electrochemical Method in Transport Phenomena, In Advances in Heat Transfer*, volume 7, pages 87–161. Academic Press, 1971.

37. W.S. Neill. Local natural convection heat transfer measurements using a thin gold-film technique. Master's thesis, Deparment of Mechanical Engineering, McGill University, 1989.

38. T. Ota and N. Kon. Heat transfer in the separated and reattached flow on a blunt flat plate. *Journal of Heat Transfer*, pages 459–462, 1974.

39. J.R. Philip. The theory of heat flux meters. *Journal of Geophysical Research*, 66:571–579, 1961.

40. A.R. Porro, Jr. T.G. Keith, and W.R. Hingst. A laser-induced heat flux technique for convective heat transfer measurements in high speed flows. *IEEE*, pages 146–155, 1991.

41. Rdf Corporation. *Temperature Measurements*, 1992.

42. R.G. Rimmer and D.M. Rowley. The measurement of temperature and convective heat transfer coefficient by a laser optical technique. *International Journal of Mechanical Engineering Education*, 15(1):31–39, 1986.

43. W.M. Roshenow and H. Choi. *Heat, Mass, and Momentum Transfer*. Prentice-Hall, Inc., 1961.

44. F.E.M. Saboya and E.M. Sparrow. Local and average transfer coefficients for one-row plate fin and tube heat exchanger configurations. *Journal of Heat Transfer*, 96:265–272, 1974.

45. S.S. Tewari and Y. Jaluria. Mixed convection heat transfer from thermal sources mounted on horizontal and vertical surfaces. *Journal of Heat Transfer*, 112:975–987, 1990.

46. L.C. Thomas. *Fundamentals of Heat Transfer*. Prentice-Hall, 1980.

47. Y.S. Touloukian and D.P. Dewitt. *Thermal Radiative Properties, Non Metallic Solids*, volume 8 of *The TPRC Data Series*. IFI/PLENUM, 1972.

48. VDI Wärmeatlas. *VDI Verlag Düsseldorf*, 1987.

49. Y. Wu and M. Lacroix. Numerical study of melting of scrap metal. *Numerical Heat Transfer*, 24:413–425, 1993.

50. W.J. Yang. *Handbook of Flow Visualization*. Hemisphere Publishing Co., 1989.

APPENDIX A CONTENTS OF THE VIDEO MOVIES

1. *FLOW VISUALIZATION IN CIRCULAR REMELTING FURNACES. UQAC/CHIP 1992.*

Introduction of the physical model

- Adjustment of burners (axi-symmetric, radial, rotating flow)
- Pile models (conical, cylindrical)

Introduction of the fluorescent mini-tuft technique

- Flat bath, axisymmetric flow
- Flat bath, radial flow
- Flat bath, rotating flow
- Conical pile, axisymmetric flow
- Conical pile, radial flow
- Conical pile, rotating flow
- Conical pile modified, rotating flow

Introduction of the popcorn technique

- Axisymmetric flow

Introduction of the smoke & laser sheet technique

- Production of laser sheet

- Generation of smoke

Visualization of flow structure by horizontal laser sheets

- Cylindrical pile, rotating flow
- Cylindrical pile, radial flow
- Cylindrical pile, axisymmetric flow
- Flat bath, rotating flow
- Flat bath, radial flow
- Flat bath, axisymmetric flow

Visualization of flow structure by vertical laser sheet

- Section through stack
- Section through burner

2. *FLOW STRUCTURE IN A SIX BURNER ROUND FURNACE UQAC/CHIP 1993*

Introduction of the physical model

Method of smoke injection

Production of light sheets

Burner arrangement

Structure of the flow, introduction of the main regions

- Toroidal region
- Core
- Merging region

Smoke injection in bursts, horizontal laser sheet

High-speed video recording technique

- Merging of individual jets

Jet behavior in 3D, diffuse illumination

Residence time

- Direct escape
- Toroidal region, spiralling-in
- Core

Behavior of the individual burners

- Burner #1, horizontal laser sheet
- Burner #6, horizontal laser sheet
- Burner #6, ordinary illumination, high-speed video
- Burner #5, horizontal laser sheet
- Burner #5, ordinary illumination, high-speed video
- Burner #4, horizontal laser sheet
- Burner #4, ordinary illumination, high-speed video

The structure of the core

- Visualization by horizontal laser sheet

Mass exchange between the core and toroidal region

Visualization of the flow structure by vertical laser sheet

- Structure of the core

Analysis of the flow at the exit

- Burner #5, horizontal laser sheet
- Burner #4, horizontal laser sheet
- Burner #6, vertical laser sheet
- Burner #5, vertical laser sheet
- Burner #4, vertical laser sheet

APPENDIX B FLOW VISUALIZATION PHOTOGRAPHS

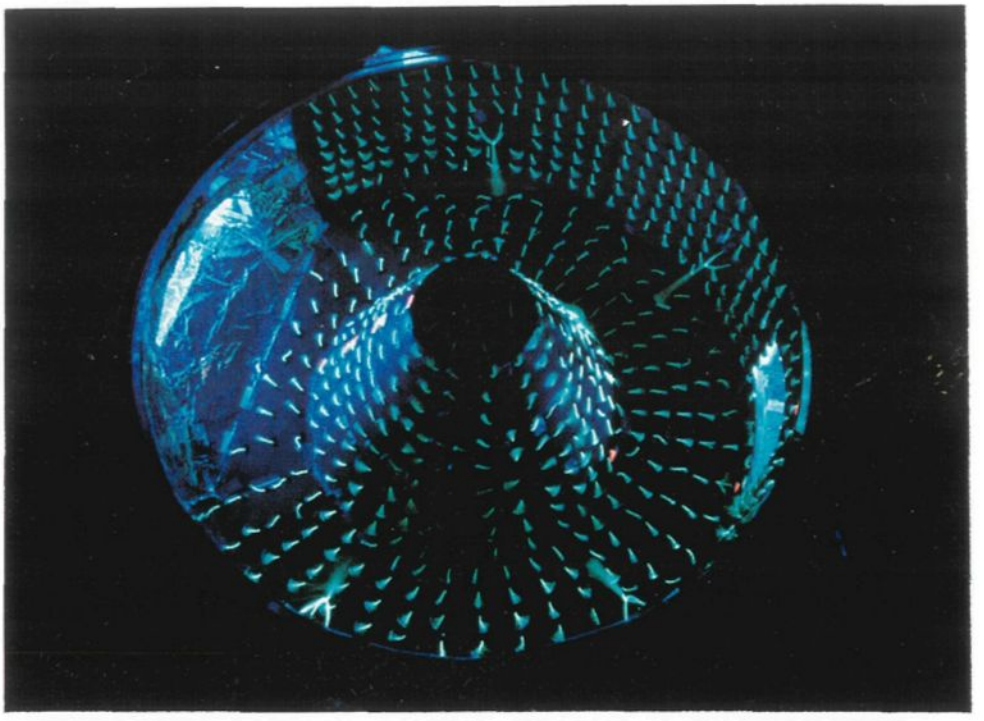

Figure B.1 Mini-tuft technique of flow visualization

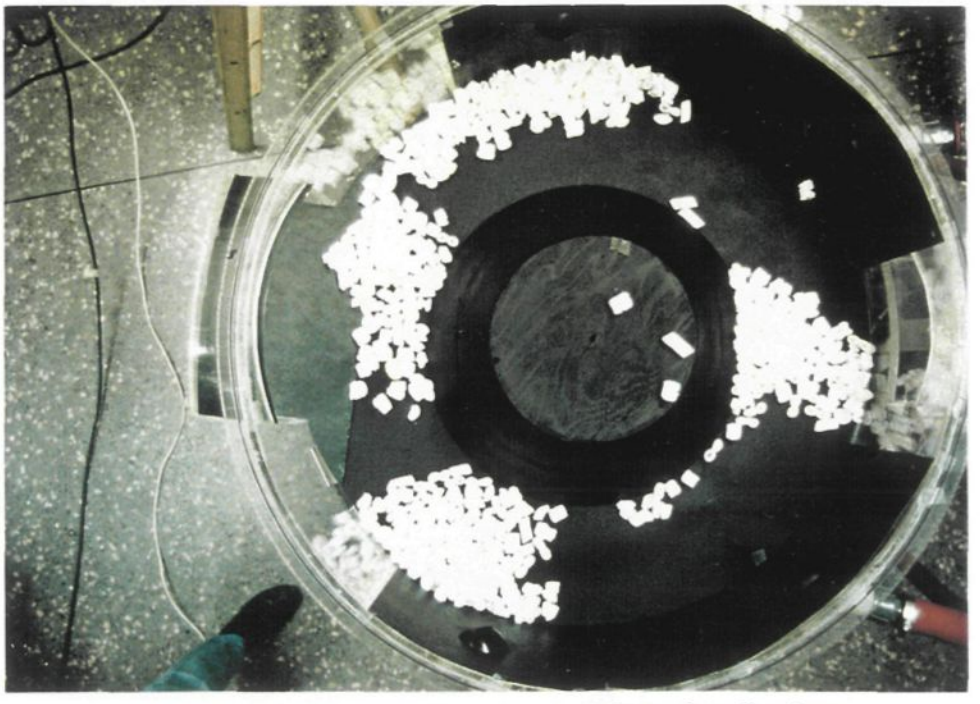

Figure B.2 "Pop corn" method of flow visualization

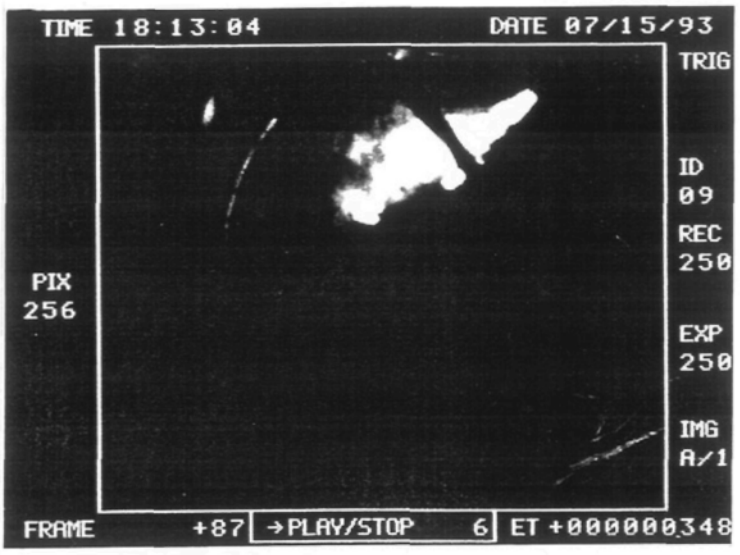

Figure B.3

Start of merging of the individual jets

Figure B.4

Merging of jets after few ms

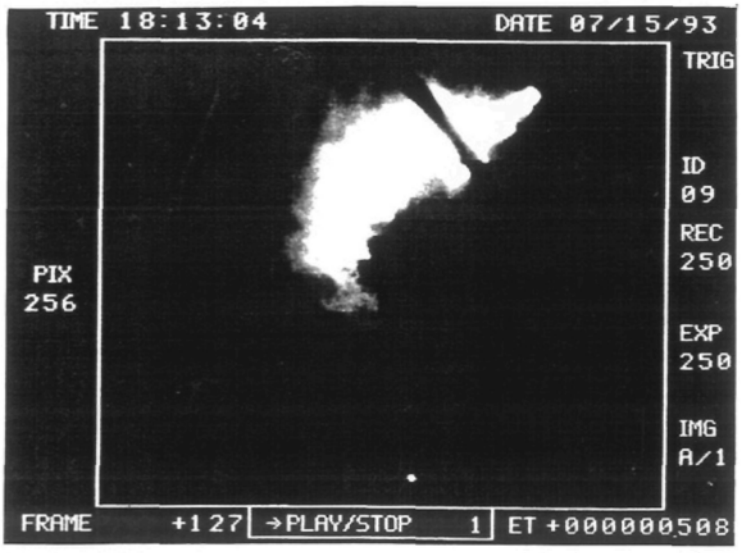

Figure B.5

At the end of merging

Figure B.6

Rotational flow formation

Figure B.7

Formation of rotational flow continuation

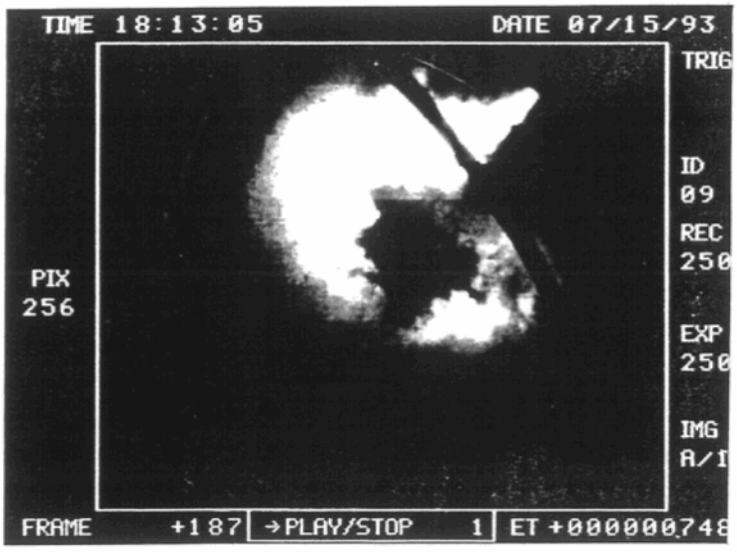

Figure B.8

Clear rotational flow

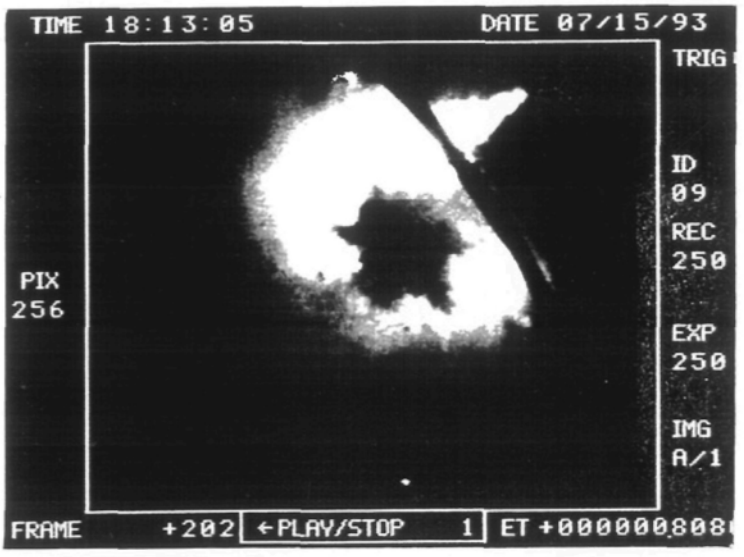

Figure B.9

Starting of the doughnut formation

Figure B.10

The "doughnut" shaped toroid-like flow

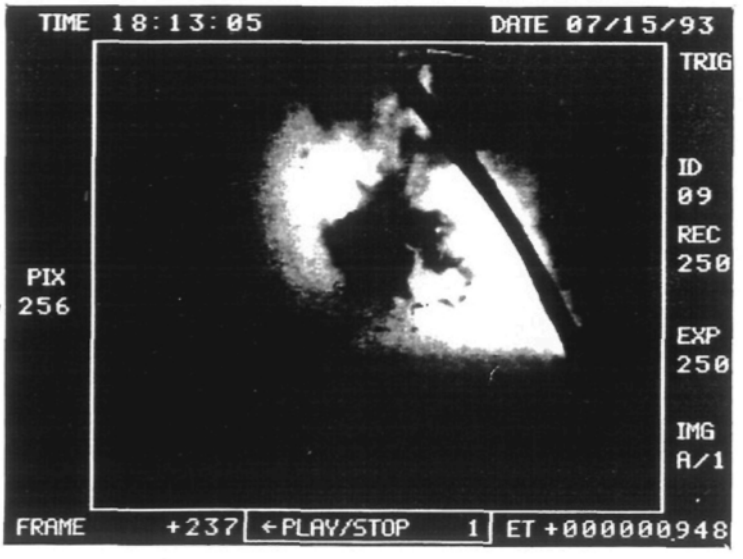

Figure B.11

Dispersion of the rotational "doughnut"

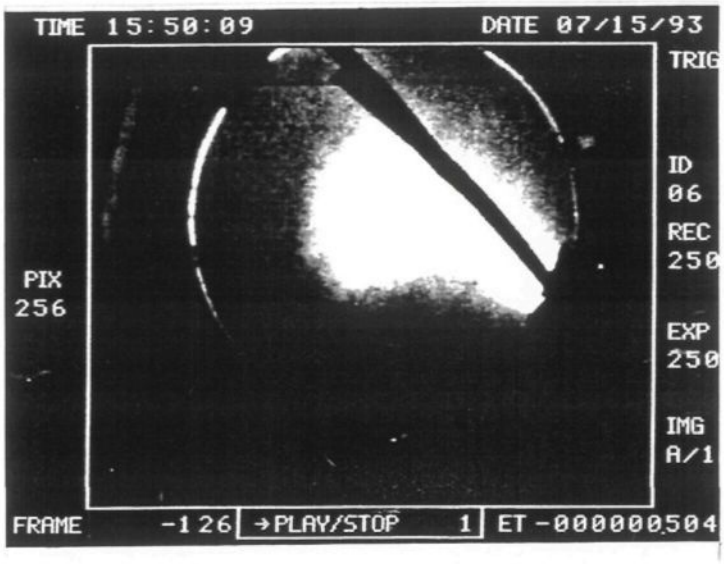

Figure B.12

Formation of the core

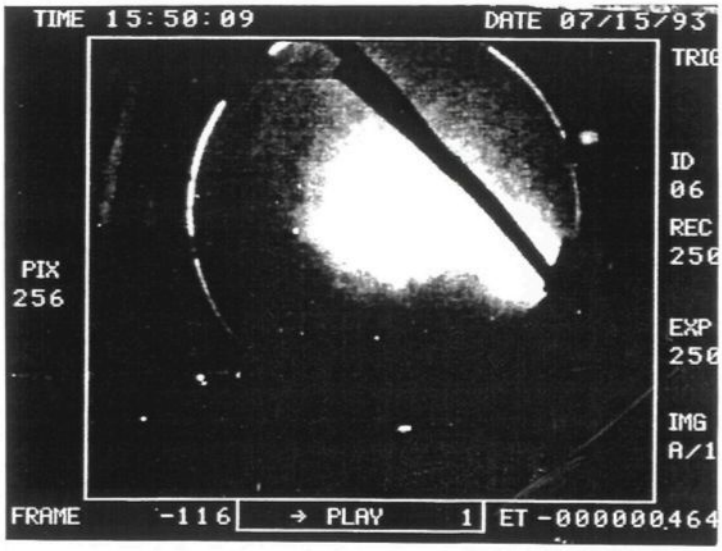

Figure B.13

Core after few ms

Figure B.14

Star shaped coherent structure

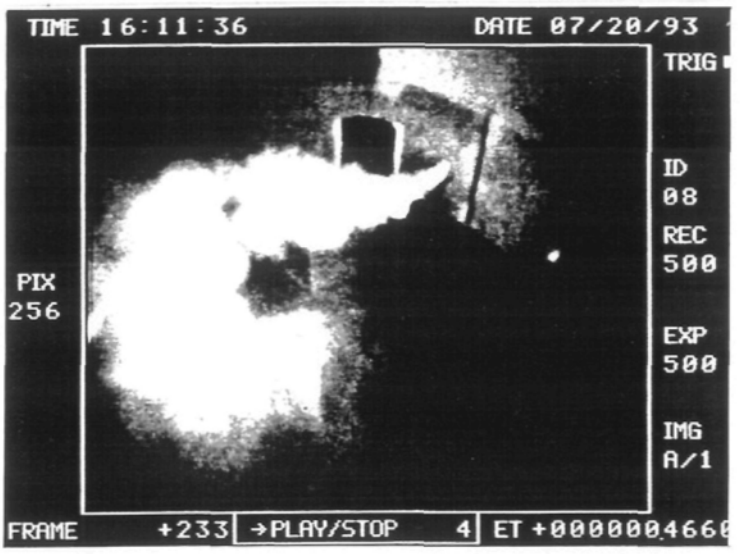

Figure B.15

Merging of jets in question mark "?"

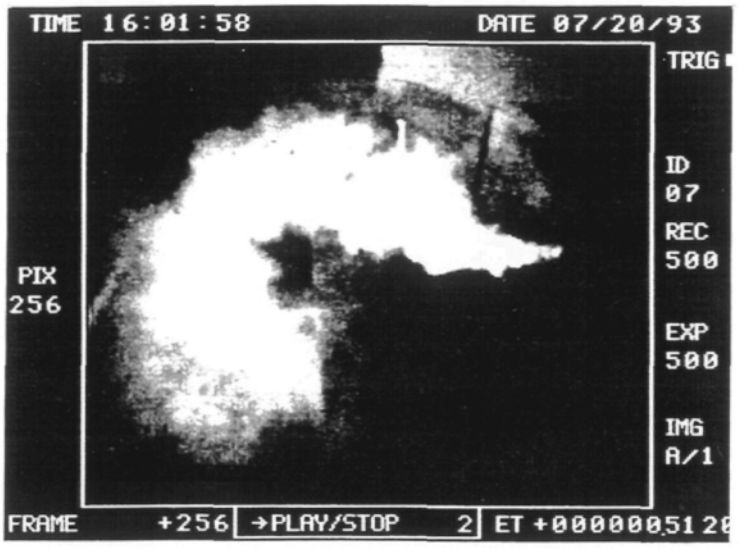

Figure B.16

Formation of "?" continuation

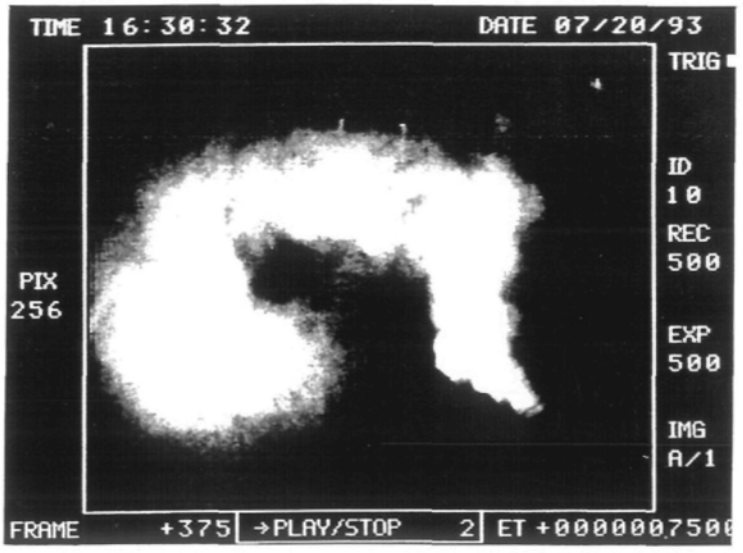

Figure B.17

End of the question mark formation

APPENDIX C MODEL AND THE HEATED SKIN TECHNIQUE

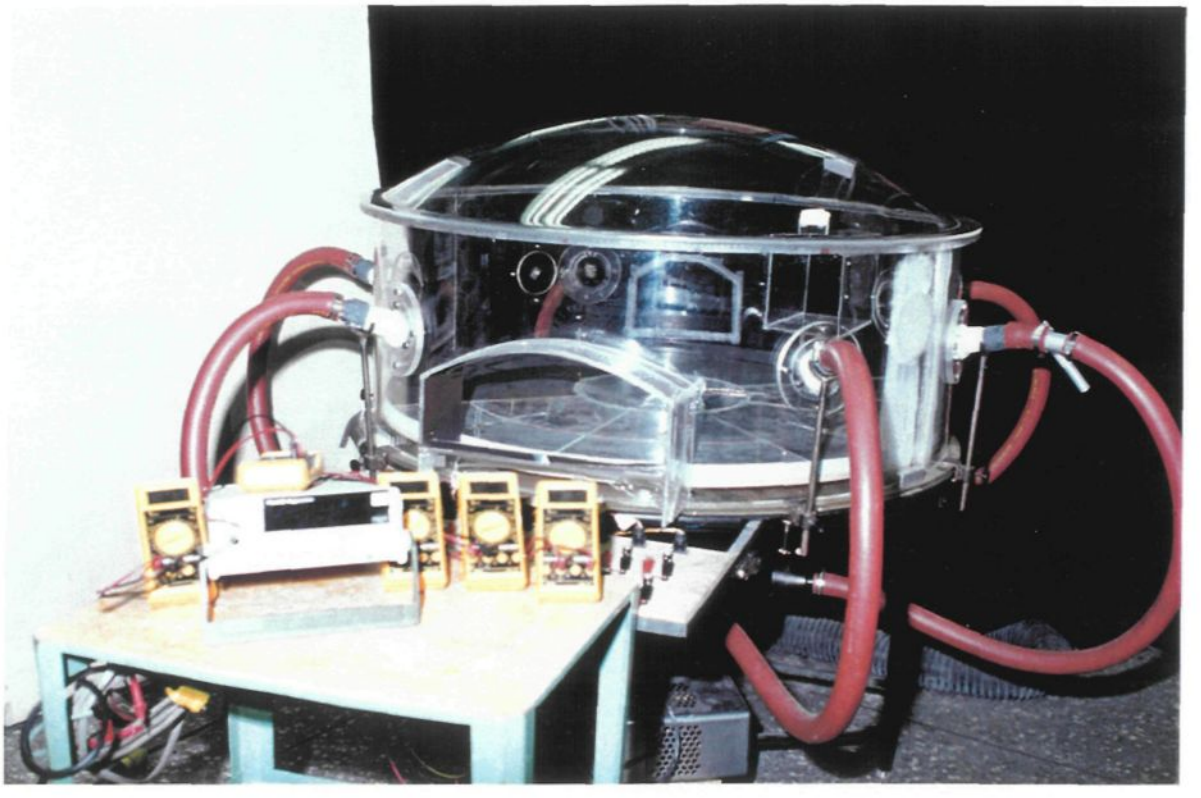

Figure C.1 Photo of the reduced scale physical model

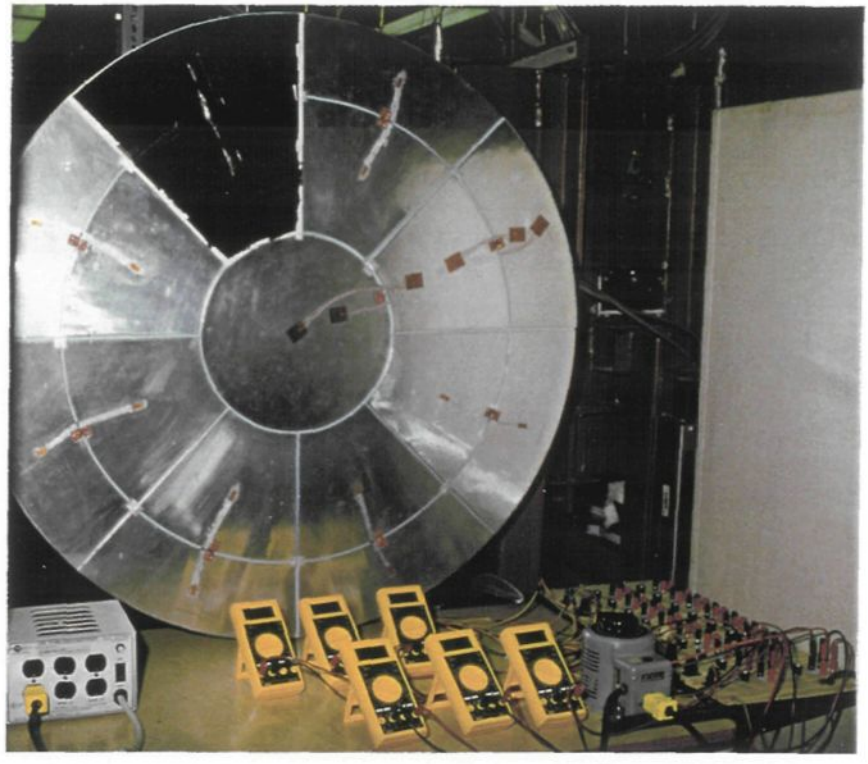

Figure C.2 The heated skin module with power regulator, multimeters, variac and control panel at the bottom

Figure C.3 The furnace model with the heated skin module

APPENDIX D DISTRIBUTION OF VELOCITY

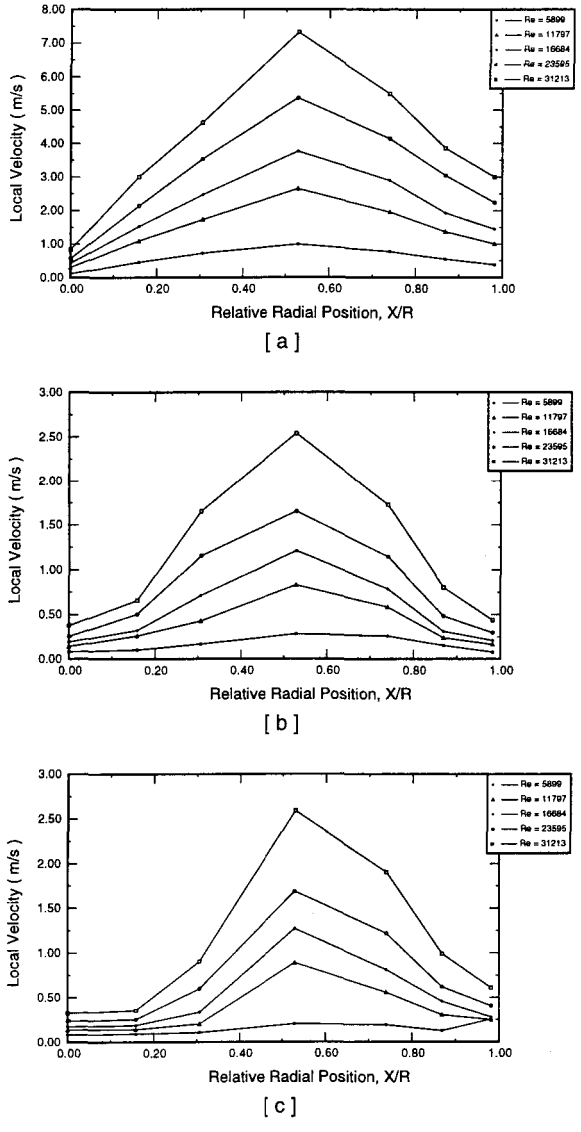

Figure D.1 Local velocity, (a) horizontal component at burner's level, (b) vertical component near the test surface, (c) vertical component at burner's level, when burners are in the original position

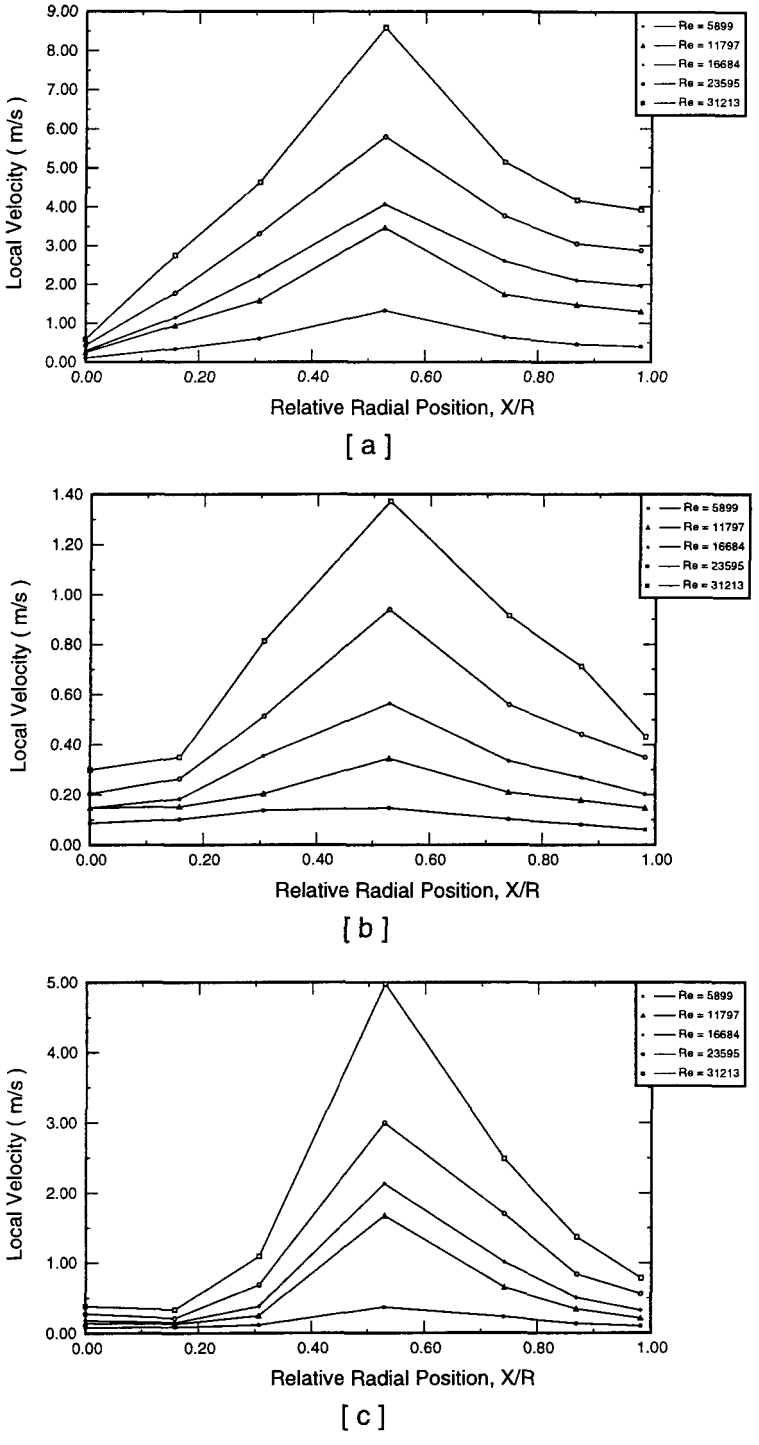

Figure D.2 Local velocity, (a) horizontal component at burner's level, (b) vertical component near the test surface, (c) vertical component at burner's level, when burners are in H15V10

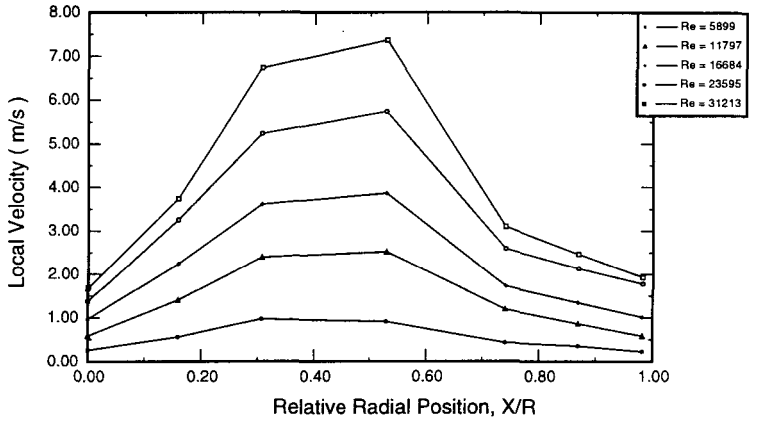

[a]

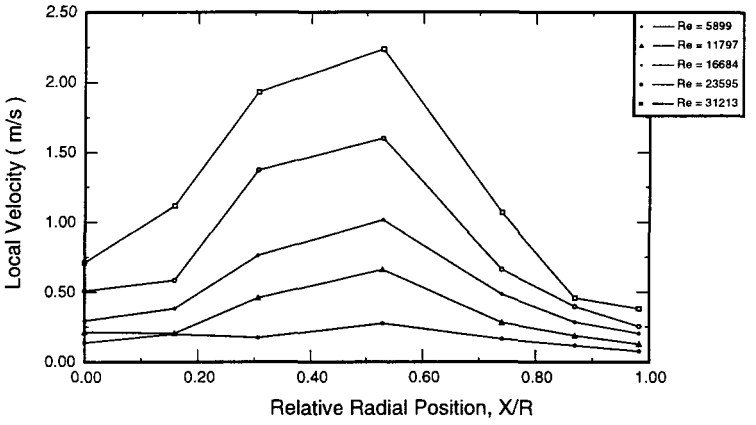

[b]

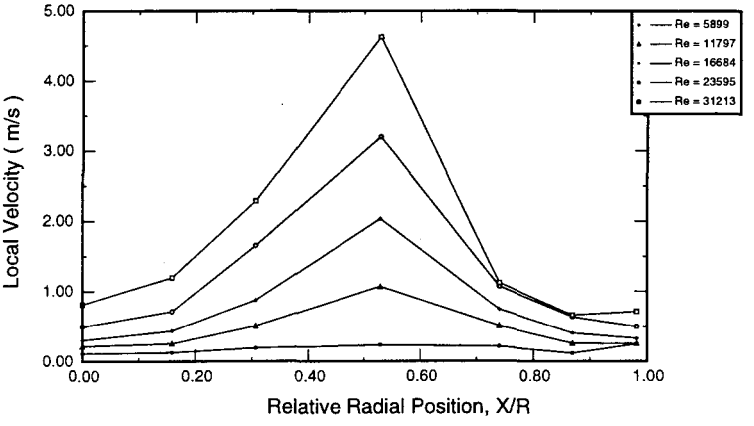

[c]

Figure D.3 Local velocity, (a) horizontal component at burner's level, (b) vertical component near the test surface, (c) vertical component at burner's level, when all burners are in H10V10

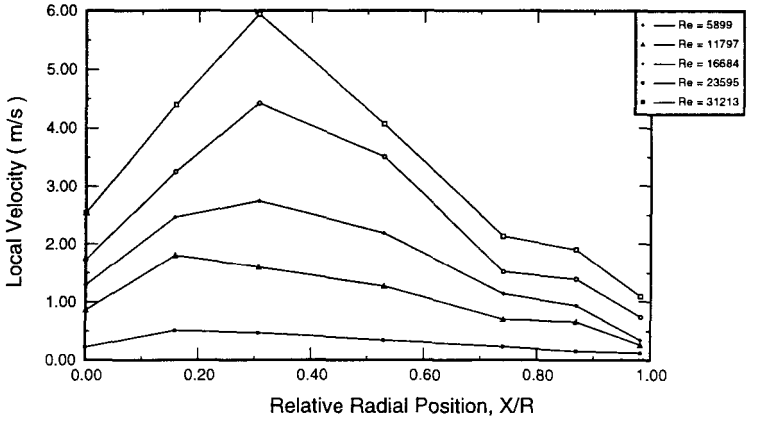

[a]

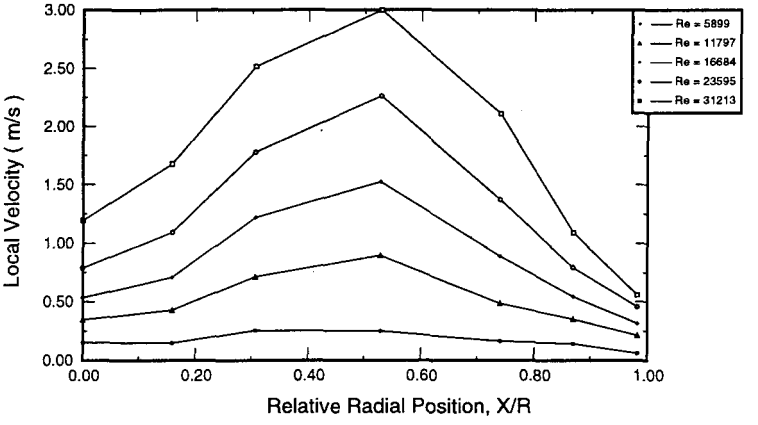

[b]

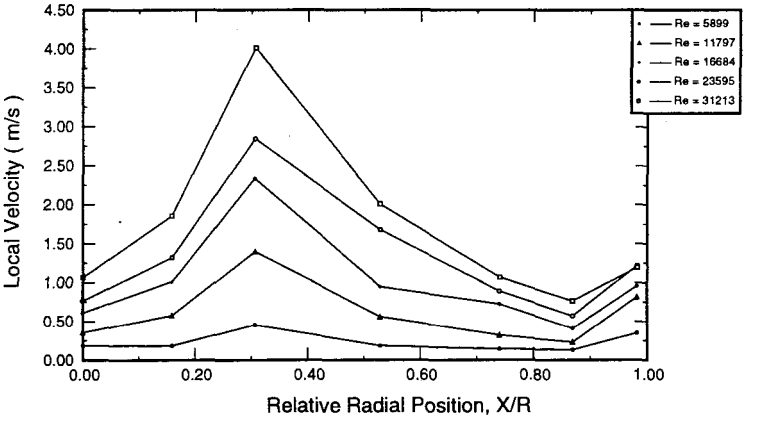

[c]

Figure D.4 Local velocity, (a) horizontal component at burner's level, (b) vertical component near the test surface, (c) vertical component at burner's level, when all burners are in H5V10

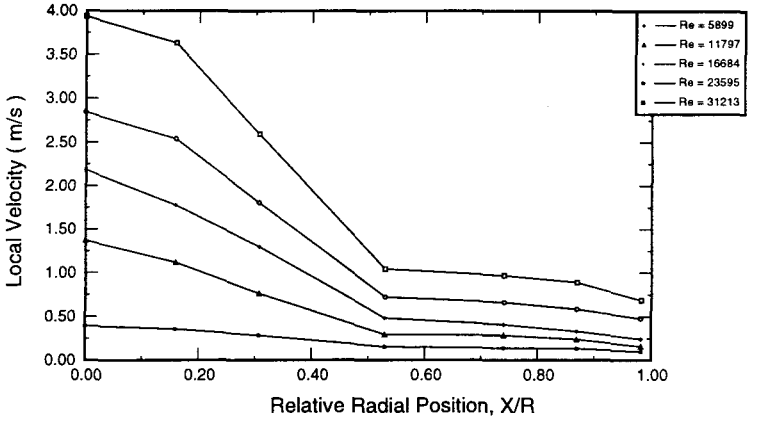

[a]

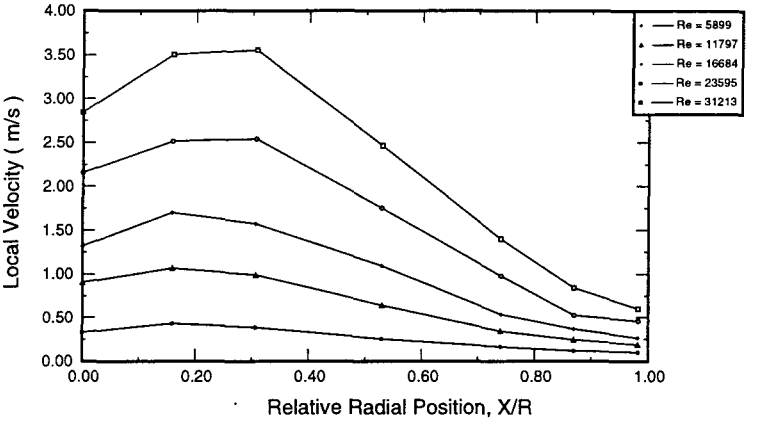

[b]

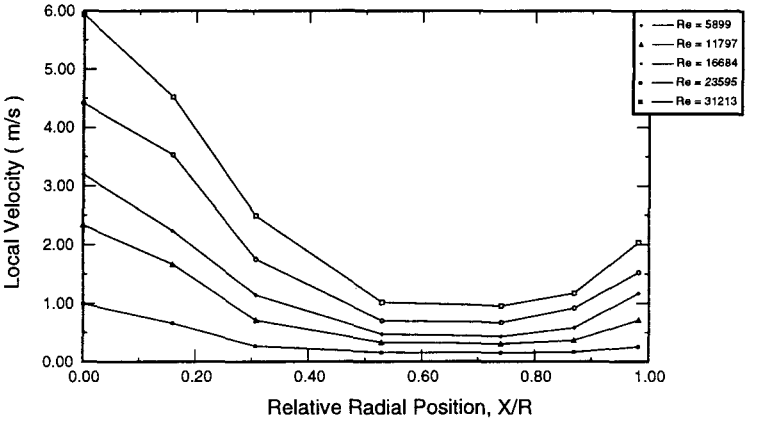

[c]

Figure D.5 Local velocity, (a) horizontal component at burner's level, (b) vertical component near the test surface, (c) vertical component at burner's level, when all burners are in H0V10

APPENDIX E GUARD HEATER TECHNIQUE

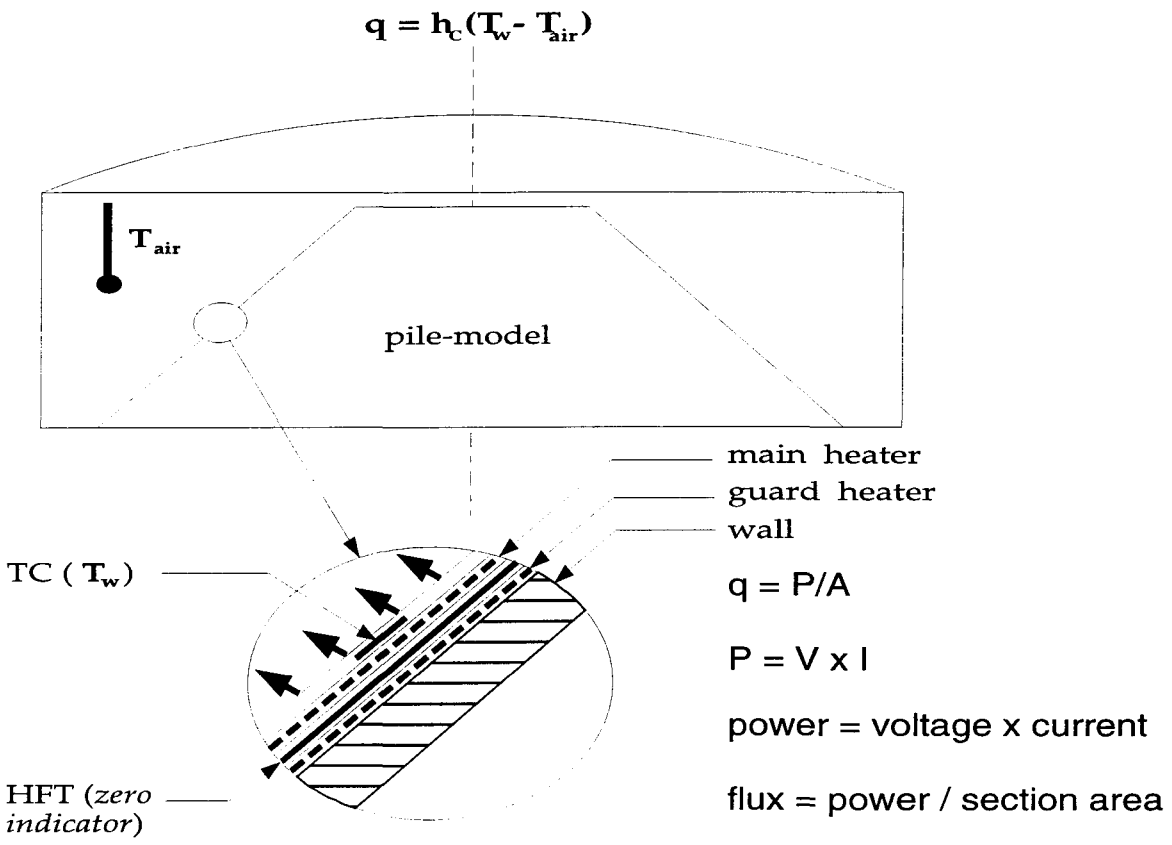

Figure E.1 Guard heater technique